# The Physics of Tropical Convection

**Ulrike Wißmeier**

München 2009

# The Physics of Tropical Convection

**Ulrike Wißmeier**

Dissertation
at the Faculty of Physics
Ludwig–Maximilians–University
Munich by

Ulrike Wißmeier
from Erlangen

Munich, July 2009

# Zusammenfassung

Die Intensität eines Gewitters wir vor allem durch zwei Parameter - Windscherung und Instabilität der Atmosphäre (quantifiziert als „Convective Available Potential Energy", CAPE) – bestimmt. Sind diese beiden Paramter groß, so kommt es zu „schweren Gewittern", wie Böenfronten, Multi- oder Superzellen. Darwin im tropischen Nordaustralien wird während der Regenzeit im Durchschnitt von zwölf solch schweren Gewittern heimgesucht – darunter auch die sogenannten „Northeasters", die sich der Küstenstadt von Nord-Osten nähern. Die Vorhersage jener schweren Gewitter gestaltet sich jedoch mitunter als schwierig, da sich bisherige Studien darüber hauptsächlich auf die Mittleren Breiten konzentriert haben, und es nur wenige konzeptionelle Gewittermodelle für die Tropen gibt. Es ist nicht bekannt ob die Gewittermodelle und Vorhersageparamter, welche für die Mittleren Breiten entwickelt wurden und auch in den Tropen Anwendung finden, überhaupt zur Vorhersage und Klassifikation tropischer Gewitter geeignet sind.

Mit Hilfe zweier idealisierter numerischer Modelle wurde der Einfluss von vertikaler Windscherung (mit/ohne Richtungsänderung mit der Höhe) auf tropische Konvektion untersucht, und mit den Ergebnissen von Simulationen von Gewittern in den Mittleren Breiten verglichen. Das Hauptaugenmerk wurde dabei auf das „Aufspalten" der anfänglichen Gewitterzelle gelegt. Letzteres führt gemäß früherer Studien zur Entwicklung von rotierenden, langlebigen Zellen – den Superzellen. Ganz gleich mit welchem Modell, Mikrophysik-Schema, welcher horizontalen Auflösung, thermischen Blase, oder Scherungsdicke die Experimente initialisiert wurden, sie zeigen alle eindeutig, dass eine größere Windscherung notwendig ist um Gewitter in den Tropen zu spalten, als für jene in den Mittleren Breiten. Untersuchungen ergaben, dass die Neigung eines Gewitters sich zu Spalten von der Geschwindigkeit, mit der sich der Gewitter-Kaltluftausfluss ausbreitet, abhängt. Eine hohe Ausbreitungsgeschwindigkeit führt zum Abschneiden der Warmluftzufuhr zur anfänglichen Gewitterzelle, und jener verbleibt weniger Zeit sich zu entwickeln und zu spalten. Die hier modellierten tropischen Gewitter produzieren einen stärkeren, d.h. schnelleren, Kaltluftausfluss als die in den Mittleren Breiten. Es zeigte sich, dass die Geschwindigkeit des Kaltluftausflusses mit sinkendem Wasserdampfmischungsverhältnis in der mittleren Troposphäre und mit steigendem Gesamthydrometeorgehalt in der Zelle steigt. Aufgrund des höheren Boden-Wasserdampfmischungsverhältnisses in den Tropen kommt es zu mehr Kondensation und somit zu einem größeren Gesamthydrometeorgehalt in den tropischen Gewittern als in jenen der Mittleren Breiten. Eine hohe Windscherung bewirkt jedoch eine Reduktion des Gesamthydrometeorgehaltes, und somit der Geschwindigkeit des Kaltluftausflusses, was begründet, warum eine größere Windscherung notwendig ist um Gewitter in den Tropen, welche einen hohen Hydrometeorgehalt haben, zu spalten als für jene in den Mittleren Breiten.

Die Richardson-Zahl, welche das Verhältnis von CAPE zur Windscherung wieder-

spiegelt und oft zur Vorhersage des Gewitters oder Gewittertyps verwendet wird, wurde auf ihre Eignung hin überprüft. Es zeigte sich, dass die Richardson-Zahl weder für die Klassifizierung der hier modellierten tropischen Gewitter, noch für solche in den Mittleren Breiten gut geeignet ist. Mit Hilfe der gefundenen Zusammenhänge zwischen Windscherung, Feuchte in der mittleren Troposphäre und Bodenfeuchte wurde ein Punktesystem entwickelt, womit die Vorhersagbarkeit von Superzellen gegenüber jener die die Richardson-Zahl verwendet, deutlich verbessert werden kann. Die Ergebnisse dieser Studie sowie dieses Punktesystems können als Grundlage für die Entwicklung neuer diagnostischer Variablen, welche für die Gewitterklassifikation in den Tropen und Mittleren Breiten geeignet sind, dienen.

Aus Beobachtungen ist bekannt, dass Seewinde eine entscheidende Rolle in der Entwicklung der Northeasters spielen. Um zwei solche Gewittersysteme, welche am 14. November 2005 bzw. am 7. Februar 2006 über Darwin wüteten, zu simulieren, wurde ein idealisiertes Modell mit dem Windprofil des jeweiligen Tages, einer thermischen Blase, welche die Konvektion auslöst, und zwei Bassins kalter Luft, welche Seewinde repräsentieren, initialisiert. Mit jener einfachen Konfiguration konnte die gesamte Entwicklung der Gewittersysteme gut simuliert werden – angefangen mit der Entstehung einer ersten Gewitterzelle über dem nördlichen Seewind, bis hin zu der Bildung von neuen Zellen an der Kaltluftausflusskante jener ersten Zelle. Die neuen Zellen formten einen Gewitterkomplex mit Eigenschaften wie sie von Böenfronten bekannt sind, wobei die Geschwindigkeit und Richtung, sowie die Orientierung und Länge der Gewitterlinie ähnlich derer der beobachteten Northeasters war. Änderungen an dem ursprünglichen Experiment offenbarten, dass zwar ein Seewind die erste Gewitterzelle – aufgrund der Zufuhr von warmer und feuchter Luft – intensivieren kann, jedoch die weitere Entwicklung, d.h. ob sich ein Gewitterkomplex bestehend aus mehreren Zellen bildet, nicht von der Intensität der ersten Zelle abhängt. Prinzipiell ist es die Stärke der horizontalen Bodenkonvergenz an der Kante des Kaltluftausflusses, welche bestimmt ob es zur Entstehung neuer Gewitterzellen kommt. Es stellte sich heraus, dass Letzteres nur der Fall ist wenn die Bodenkonvergenz über eine genügend große Zeitspanne vorhanden, und ausreichend stark ist. Große Konvergenz wurde dann erreicht, wenn sich die vertikale Windscherung der Umgebung mit der Scherung, welche von dem Kaltluftausfluss erzeugt wurde, die Waage hielt. Um diesen Zusammenhang zu beschreiben wurde eine etwas veränderte Form des Rotunno-Klemp-Weisman-Kriteriums vorgeschlagen. In weiteren Untersuchungen des Kaltluftausflusses wurde herausgefunden, dass jener stark ist, wenn die Gewitterzelle, von der er ausgeht, geneigt ist, sodass der Abwind nicht in den Aufwind fällt, sondern eine spezifische Region des Kaltluftbassins mit kalter und trockener Luft versorgt.

Wenngleich nicht alle in der Studie verwendeten Parameter aus Messungen bekannt sind, so kann jedoch die Bestimmung anderer Größen, gemeinsam mit den hier gefundenen Zusammenhängen helfen, jene Parameter abzuschätzen. Vorschläge wie die Ergebnisse dieser Arbeit zur Verbesserung der Vorhersage von Gewittern beitragen können wurden gemacht. Ferner sei erwähnt dass, obgleich die Studien speziell für das Gebiet um Darwin in Nordaustralien durchgeführt wurden, die Ergebnisse mitunter auch für andere Regionen in den Tropen oder Mittleren Breiten gelten können.

# Contents

# Chapter 1

# Introduction

## 1.1 Background and motivation

*,, ... Nun laßt auch niederwärts, durch Erdgewalt*

*Herabgezogen, was sich hoch geballt,*

*In Donnerwettern wütend sich ergehn,*

*Heerscharen gleich entrollen und verwehn! ..."*

*[Johann Wolfgang von Goethe, Howards Ehrengedächtnis[1]]*

Thunderstorms have always impressed humans and the cumulonimbus cloud that Goethe is referring to above is still one of the most visually striking and photogenic of all cloud phenomena. However, even though impressive, many hazardous weather events are associated with thunderstorms. Lightning causes many fires around the world each year and leads to severe injuries or to death when people are struck. Thunderstorms can produce intense rainfall, which can lead to flash flooding, and hail larger than tennis balls, which causes immense damage to property. Strong winds associated with thunderstorm downdraughts knock down trees and power lines, and tornadoes with winds up to about 140 m s$^{-1}$ devastate whatever lies in their path. A thunderstorm is classified as "severe" when one or more of the following accompany it: hail with a diameter of 2 cm or larger; strong winds with speeds of 90 km h$^{-1}$ or greater; tornados; flash flooding[2].

Figure 1.1 shows the global distribution of lightning as observed between April 1995 and February 2003, indicating that most of the flashes, and thus thunderstorms, are observed in the tropics. Even though thunderstorms are more frequent in the tropics than in the mid-latitudes, tropical thunderstorms are not generally considered to be severe.

Studies of thunderstorms from field campaigns in the United States (U.S.), along with numerical modelling experiments, *e.g.*, by Weisman and Klemp (1982, hereafter[3] WK82)

---

[1] "Now downwards by the world's attraction driven, / That tends to earth, which had upris'n to heaven; Threat'ning in the mad thunder-cloud, as when / Fierce legions clash, and vanish from the plain;"

[2] Only contained in the definition of severe thunderstorms of the Australian Bureau of Meteorology, and the German Weather service (DWD).

[3] A list of all acronyms used in the thesis is given in Appendix A
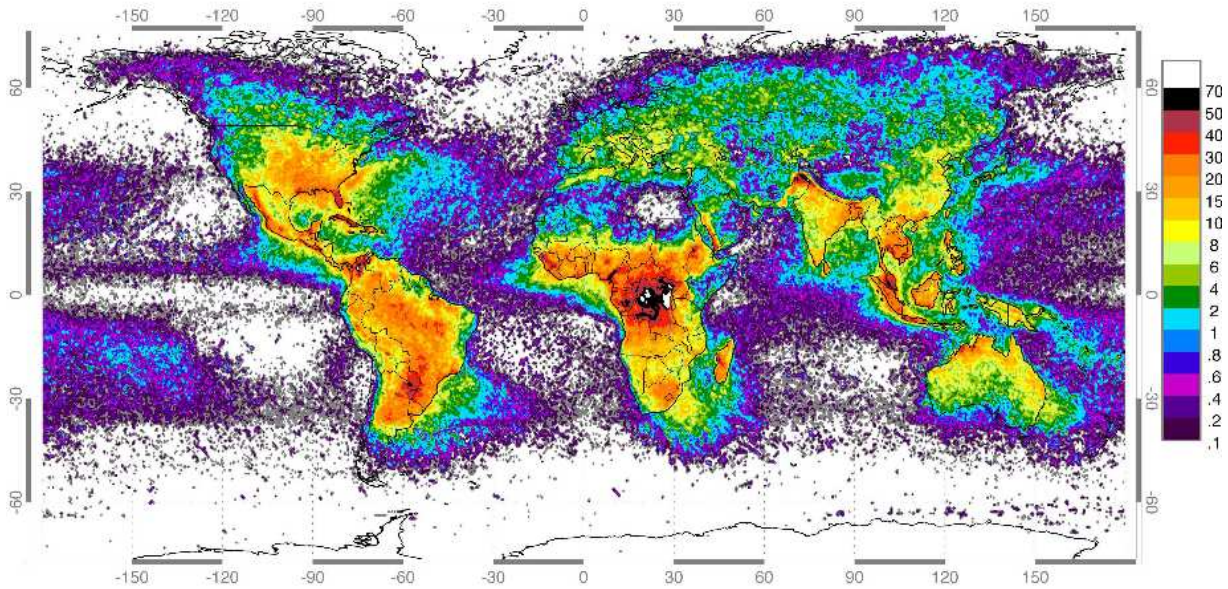
Figure 1.1: Global distribution of lightning between April 1995 and February 2003, from the combined observations of the NASA Optical Transient Detector (April 1995 – March 2000) and the Land Information System (January 1998 – February 2003) instruments. Shading represents the annual flash rate. Courtesy of NASA.

have shown that the severity of a thunderstorm depends on a small number of observable parameters defining the environment in which the thunderstorm grows. Two of these parameters are the atmospheric stability, also expressed through the Convective Available Potential Energy (CAPE), and the change in the horizontal wind speed and direction with height, referred to as vertical wind shear. WK82 showed that for a given amount of environmental CAPE, weak vertical wind shears produce short-lived single cells, low-to-moderate shears produce multicells, while moderate-to-high shears produce thunderstorms with a rotating updraught, also called supercells. The definition of "weak", "moderate", and "high" wind shears will be explained later on. A line of active thunderstorms including connected areas of precipitation associated with the storms is called a squall line. In general, severe weather is more frequently associated with squall lines and supercells (Houze 1993).

The mid-latitudes provide the most favourable environment for supercell formation. In this region, cold polar air meets warmer subtropical air, often generating convective precipitation along the collision boundary. Further, the vertical wind shear (vertical derivative of the horizontal wind) can be large due to the large horizontal temperature gradients which exist in the mid-latitudes. However, the vertical derivative of the horizontal wind is also inverse proportional the Coriolis parameter, which increases with latitude, thus counteracting the effect the temperature gradient has on the generation of vertical wind shear. In the U.S., about 100000 thunderstorms occur each year, and they are most common over the Florida Peninsula and the southeast plains of Colorado. The greatest severe weather threat in the U.S. extends from Texas to southern Minnesota and is called "tornado alley". This region experiences a high frequency of supercells which are capable of forming tornadoes. In terms of absolute tornado counts, the U.S. leads the list, with an average of over 1000

Figure 1.2: Photograph of a thunderstorm near the Ammersee in southern Germany, taken on 28 May 2005. Courtesy of Markus Garhammer.

tornadoes recorded each year. Severe thunderstorms present a violent threat to society also in Central Europe, even though their frequency is less than in the U.S. tornado alley. The damage from severe local thunderstorms in Europe is significant, sometimes exceeding one billion Euros per event (hail or tornado / downburst) (Dotzek 2002). Figure 1.2 shows a thunderstorm which occurred in southern Germany in the late afternoon on 28 May 2005.

Even though less frequent than in the mid-latitudes, severe thunderstorms occur also in the tropics. The city of Darwin (12°S, 131°E), which lies within the tropics of northern Australia, records 12 severe events during the "build-up" and wet season (October to May) during an average of 80 days of thunder each year. For many regions in the tropics, *e.g.*, around Darwin, sea breezes are considered to play an important role in the evolution of deep convection. The sea breeze occurs during the summer months in many coastal regions, and results from temperature differences between the land and ocean, leading to onshore flow during the day, if the broadscale flow does not have a strong offshore component. Studies of sea breezes in the tropics have shown that the convergence caused by sea breezes can trigger thunderstorms (*e.g.*, Keenan and Carbone 1992, Carbone *et al.* 2000).

Severe tropical thunderstorms are not only observed in the Darwin region. "Kalbaisakhi" are thunderstorms which occur over the Gangetic West Bengal, Bangladesh, and in North East India. These storms are the most severe to be recorded anywhere in the subcontinent. In India more than 70% of the tornadoes are associated with these "Kalbaisakhi" and 28 of such storms occur, on average, during the pre-monsoon months of April and May (S. M. Deshpande, personal communication).

One of the most important problems for weather forecasters in tropical regions is the prediction of severe weather resulting from thunderstorms. However, statistics show that forecasting severe thunderstorm events in the tropics is a challenge. For example, the probability of detection of severe thunderstorms in the Darwin area was lower than 50% during the five wet seasons 2002/03 – 2006/07, and the false alarm ratio, indicating overprediction of severe thunderstorms, was over 50% in the seasons 2002/03 – 2005/06 (see Table 1.1). One reason for these poor forecasts is that forecasters in Darwin, as well as elsewhere in the

| Season | Warned events | Successful warnings | Missed events | False alarms | POD | FAR |
|--------|---------------|---------------------|---------------|--------------|-----|-----|
| 2002/03 | 12 | 2 | 11 | 10 | 15% | 83% |
| 2003/04 | 3 | 0 | 12 | 3 | 0% | 100% |
| 2004/05 | 10 | 3 | 10 | 7 | 23% | 70% |
| 2005/06 | 11 | 5 | 7 | 6 | 42% | 55% |
| 2006/07 | – | 9 | 11 | – | 45% | – |

Table 1.1: Severe Thunderstorm Warning Statistics for the seasons 2002/03 – 2006/07, where the number of warned events issued by the Bureau of Meteorology in Darwin, successful warnings, missed events, and false alarms are given. Also shown, the Probability of Detection (POD) calculated as the ratio of successful warnings to all events, and the False Alarm Ratio (FAR) calculated as the ratio of false alarms to the sum of successful warnings and false alarms. The symbol "–" represents unknown quantities.

tropics, have few conceptual tropical thunderstorm models at their disposal and there is a notable lack of useful theory about severe tropical thunderstorms that they can call upon. While many studies on mid-latitude thunderstorms have been conducted during the past decades, helping to improve the forecasts, weather prediction in the tropics is sometimes of limited accuracy when it comes to the forecast of weather involving deep convection, due to the lack of studies of tropical thunderstorms.

For the foregoing reasons, the U.S. National Academy of Science (1998) emphasised that understanding how tropical convection is organised and the prediction of tropical convection are among the most important problems in atmospheric science today. An International Workshop on the Dynamics and Forecasting of Tropical Weather Systems held in Darwin in 2001, highlighted the great difficulty in forecasting weather systems in the tropics, especially thunderstorms (Smith *et al.* 2001).

One of the major goals of this work is to use two numerical models to investigate how thunderstorms in a tropical environment are influenced by vertical wind shear. Different temperature and moisture profiles, as well as different wind profiles are used in the models, and the results are compared to those of mid-latitude simulations. Further, I investigate the extend to which the indices developed for the prediction of mid-latitude thunderstorm types are applicable also to the tropics. Moreover, I examine the influence of a sea breeze on deep convection and the role of the sea breeze in producing vertical wind shear leading to the development of a severe multicell complex. In the forthcoming sections, preliminary knowledge and terminology are provided to help the reader to understand the results of this study.

## 1.2   Two basic concepts

A thunderstorm is a deep convective cloud accompanied by lightning and thunder, which is driven by buoyancy. The buoyancy force is an upward force exerted upon a parcel of fluid in a gravitational field due to the density difference between the parcel and that of
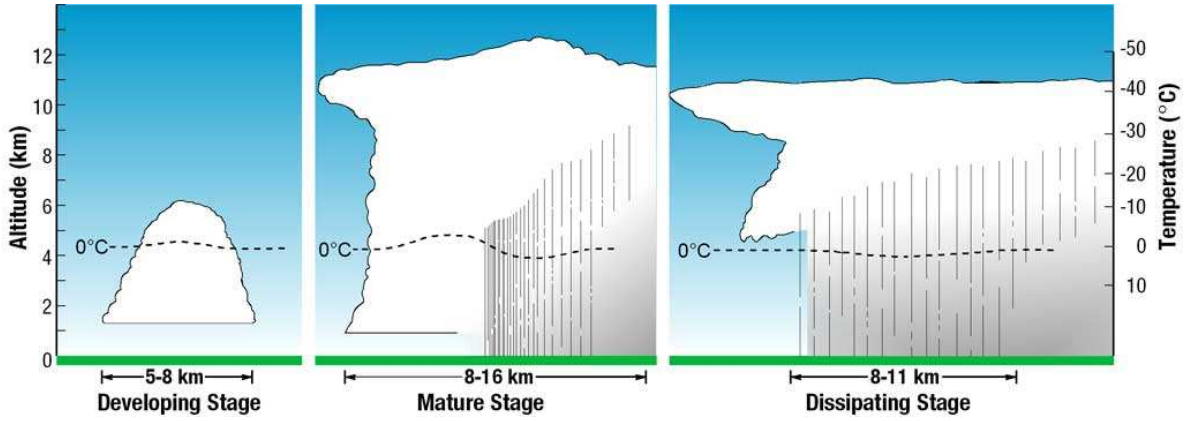
Figure 1.3: Schematic, showing the three stages of a single cell: developing stage, mature stage, and dissipating stage. Courtesy of National Oceanic and Atmospheric Administration (NOAA), National Severe Storms Laboratory (NSSL).

the surrounding fluid. The buoyancy is given by

$$B = g \, \frac{T_{vp} - T_{ve}}{T_{ve}}, \tag{1.1}$$

where $g$ is the acceleration due to gravity, $T_{vp}$ is the virtual temperature of the parcel, and $T_{ve}$ is the virtual temperature of the environment. An energetic measure of the viability of convection is the Convective Available Potential Energy (CAPE):

$$CAPE = \int_{i}^{LNB} B \, dz, \tag{1.2}$$

where $B$ is the buoyancy for a parcel lifted through the troposphere, $i$ is the initial parcel level, and $LNB$ is the level of neutral buoyancy.

Besides CAPE, the vertical wind shear plays also an important role in determining the thunderstorm type. For an environmental wind profile defined by $\mathbf{v}_h(z) = [u(z), v(z)]$, where $(u, v)$ are the Cartesian velocity components in the $(x, y)$ directions, the environmental wind shear vector $\mathbf{S}$ is defined as

$$\mathbf{S} = \frac{d\mathbf{v}_h}{dz} = \left( \frac{du}{dz}, \frac{dv}{dz} \right). \tag{1.3}$$

If the wind speed is directed in the same direction at all height levels $z$, the vertical wind shear is called "uni-directional".

## 1.3   Thunderstorm types

Thunderstorms can occur in isolation as a single cell, multicell, or supercell, or be part of a group as in a squall line, a mesoscale convective complex, or a tropical cyclone.

### 1.3.1 Single cell storms

Single cell storms occur in environments without, or with only small vertical wind shear. Analysing aircraft penetration measurements taken during the "Thunderstorm Project", Byers and Braham (1949) identified three stages in the evolution of a single cell: the developing stage, the mature stage, and the dissipating stage (see Fig. 1.3). During the first stage, or cumulus stage, the updraught grows as buoyant air rises and condenses once it reaches the lifting condensation level. Growing further, single cells reach the freezing level, above which the formation of ice, hail, and graupel may start. Evaporation due to entrainment and precipitation result in a downdraught, which is a sign that the single cell has reached its mature phase. When the downdraught reaches the ground, a pool of cold air develops at the surface and spreads out uniformly in all directions, lifting warm and moist environmental air and supplying it into the updraught. However, once the cold pool – also called gust front – spreads out too far, the updraught is cut off from its source of energy, the warm moist air, and starts to dissipate; the single cell is now in the dissipating stage. Usually, the whole life cycle of the single cell occurs in less than an hour and thus, the threat of heavy rainfall leading to flash flooding is small due to the short lifetime.

### 1.3.2 Multicell storms

Multicell storms occur in environments with large environmental buoyancy and low-to-moderate wind shear (WK82). A multicell consists of a series of single cells, whereby each cell is in a different stage of its life cycle. New updraughts form along the upwind edge of the system due to the strong low-level convergence created as the gust front from the pre-existing cells is opposed by the low-level wind. Multicells tend to produce severe weather such as large hail, strong winds, and heavy rain. The latter can lead to flash flooding if the system is quasi-stationary.

### 1.3.3 Supercell storms

The most intense and most dangerous type of thunderstorm is the supercell, which forms in environments with moderate-to-strong wind shears and large environmental buoyancy (WK82). A supercell is a convective storm that consists of a single rotating updraught. While in weakly-sheared environments the rain falls into the updraught and eventually destroys it, the regions of ascending and descending air within the supercell are separated, leading to a persistent updraught. Figure 1.4 depicts a schematic of a supercell, indicating its cyclonically rotating vortex (mesocyclone). The dynamics of these thunderstorms have been studied extensively in the past decades (see, *e.g.*, Rotunno 1981, Klemp 1987), and a summary of this research will be given in section 1.4.

**Supercells in tropical cyclones**

Mini-supercells – so-called because they are shallower and smaller in diameter than the classic Great Plains supercells – have been observed in rainbands of tropical cyclones, *e.g.*, in the offshore outer rainbands of Hurricane Ivan in 2004. As Ivan crossed the southeast U.S., over 115 tornadoes were reported (Eastin and Link 2009). In general, the majority of landfalling tropical cyclones produce tornadoes and in the U.S. about 10% of all deaths associated with tropical cyclones are the result of tornadoes (Novlan and Gray 1974).
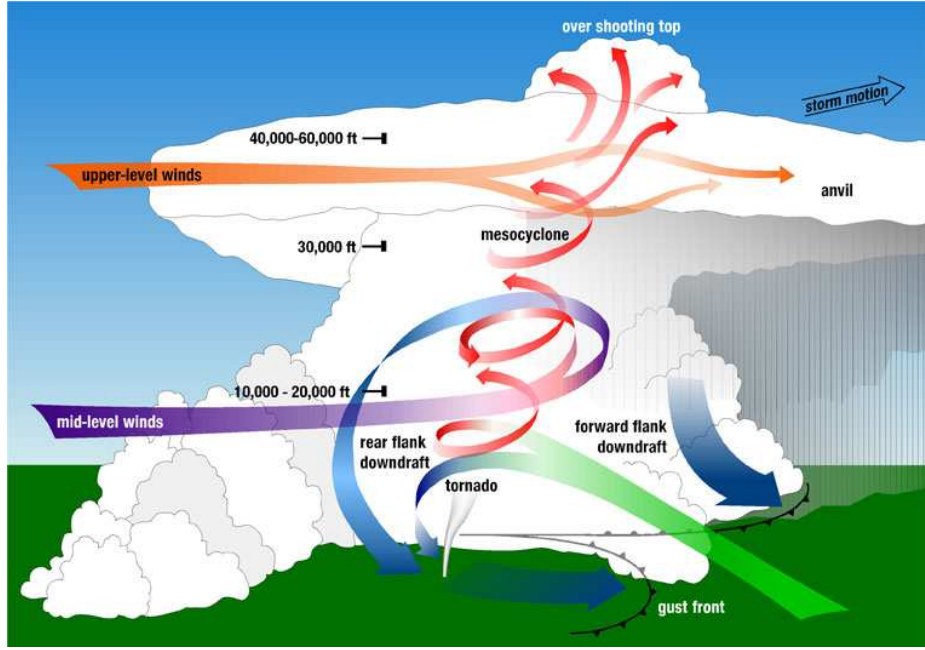
Figure 1.4: Schematic of a supercell. The red arrows represent the rotating updraught and the blue arrows the downdraught. Courtesy of NOAA, NSSL.

Thus, it is important to identify and monitor supercells within tropical cyclones as early as possible. However, the detection of rotating cells at large ranges from land-based radars can be limited due to the small diameter of the cells.

## 1.4 Thunderstorm dynamics

To examine how the vertical wind shear influences the storm dynamics and can lead to a rotating updraught, a measure of rotation, the vorticity, needs to be introduced. The vorticity $\boldsymbol{\omega}$ is given by

$$\boldsymbol{\omega} = (\xi, \eta, \zeta) = \nabla \times \mathbf{v} = \left( \frac{\partial w}{\partial y} - \frac{\partial v}{\partial z} \right) \mathbf{i} + \left( \frac{\partial u}{\partial z} - \frac{\partial w}{\partial x} \right) \mathbf{j} + \left( \frac{\partial v}{\partial x} - \frac{\partial u}{\partial y} \right) \mathbf{k}, \qquad (1.4)$$

where $(u, v, w)$ are the components of velocity $\mathbf{v}$, and $(\xi, \eta, \zeta)$ the components of vorticity in the $(x, y, z)$ directions, respectively. As the updraught of a supercell rotates around a vertical axis, it is of interest to examine the evolution of the vertical vorticity component $\zeta$, which satisfies the equation:

$$\frac{\partial \zeta}{\partial t} = -\mathbf{v}_h \cdot \nabla \zeta - w \frac{\partial \zeta}{\partial z} \underbrace{-\zeta \left( \frac{\partial u}{\partial x} + \frac{\partial v}{\partial y} \right)}_{\text{stretching}} + \underbrace{\left( \frac{\partial w}{\partial y} \frac{\partial u}{\partial z} - \frac{\partial w}{\partial x} \frac{\partial v}{\partial z} \right)}_{\text{tilting}} +$$

$$+ \underbrace{\frac{1}{\rho^2} \left( \frac{\partial \rho}{\partial x} \frac{\partial p}{\partial y} - \frac{\partial \rho}{\partial y} \frac{\partial p}{\partial x} \right)}_{\text{solenoidal}}, \qquad (1.5)$$

where the first two terms on the right hand side are advection terms, the third term is the stretching (divergence) term, the fourth term is the tilting term, and the last one is the solenoidal term. Note that the Coriolis force is assumed to be zero in Eq. (1.5), which is a valid approximation for mesoscale[4] phenomena. In a vertically-sheared environment, *e.g.*, where $u$ is a function of height $z$, and $\partial v/\partial z = 0$, horizontal vortex lines are embedded in the environmental shear (see Fig. 1.5a). Rising buoyant air within an updraught tilts these vortex lines into the vertical, creating vertical vorticity $\zeta$. Equation (1.5) shows that once vertical vorticity $\zeta$ is generated by the updraught through tilting ($\partial w/\partial y \, \partial u/\partial z \neq 0$), the vortex tubes can be stretched further. In an environment with uni-directional shear ($u = f(z), v = 0$), positive (cyclonic) vertical vorticity is then generated along the southern flank of the updraught, and negative (anticyclonic) vorticity is produced on the northern flank. This can be seen in Fig. 1.5a, where the sign of vorticity within the updraught is denoted by $+$ or $-$.

Once the downdraught develops, the vortex tubes get tilted downward, and a cold pool forms at the surface below the thunderstorm (see Fig. 1.5b). However, while in weakly sheared environments the gust front spreads out almost uniformly in all directions, the cold pool in strongly sheared environments is prevented from moving out ahead of the thunderstorm by the low-level relative environmental flow. Thus, the updraught is maintained with warm and moist environmental air which is lifted by the gust front, extending the longevity of the thunderstorm. The rotation in each updraught leads to a pressure deficit in the centre of each vortex and an upwards-directed pressure gradient force is produced in the north and south of the storm centre, thus favouring updraught growth on these sides (Klemp 1987). The gray shaded arrows in Figs. 1.5 represent the upward acceleration of the surface air. In response to these forcing influences, the two newly built updraughts then start to move apart. This process is called "storm splitting". Numerical simulations by Rotunno and Klemp (1982) demonstrated that updraught splitting occurs, even if the downdraught is prevented from forming, suggesting that the vertical pressure gradients are the fundamentally important factor in splitting the cloud. After splitting commences, the warm inflow to the updraughts comes from the northeast and southeast, respectively, and the storms propagate transverse to the normal shear vector, *i.e.*, towards the left (north) and right (south), giving them their names "left-" and "right-mover". These supercells may intensify further when they move at a similar speed as the gust front, thus allowing the warm and moist air to enter the updraughts. Supercells with lifetimes of more than seven hours have been observed (*e.g.*, Edwards 2006).

Strong uni-directional wind shear leads to a mirror-image pair of rotating thunderstorms which are equal in strength. However, such mirror-image storms are rare in nature (Davies-Jones 1986). In the northern hemisphere, right-movers are observed far more often than left-movers. The reason for that is that a clockwise turning hodograph[5], which is often associated with thunderstorm weather patterns in the northern hemisphere, favours the right-mover, while an anticlockwise turning hodograph would favour the left-mover (see, *e.g.*, Klemp and Wilhelmson 1978). Rotunno and Klemp (1982) showed that the vortex pair, which is generated through the tilting of horizontal vortex tubes, is normal to the shear vector. In the uni-directional shear case, the shear vector points from west to east at all

---

[4]Mesoscale is a size scale, referring to weather systems smaller than synoptic-scale systems. Mesoscale systems have horizontal dimensions generally ranging from around 2 km to several hundred kilometres.

[5]A hodograph represents the vertical distribution of the horizontal wind. A clockwise turning hodograph means that the wind vector veers clockwise with height.
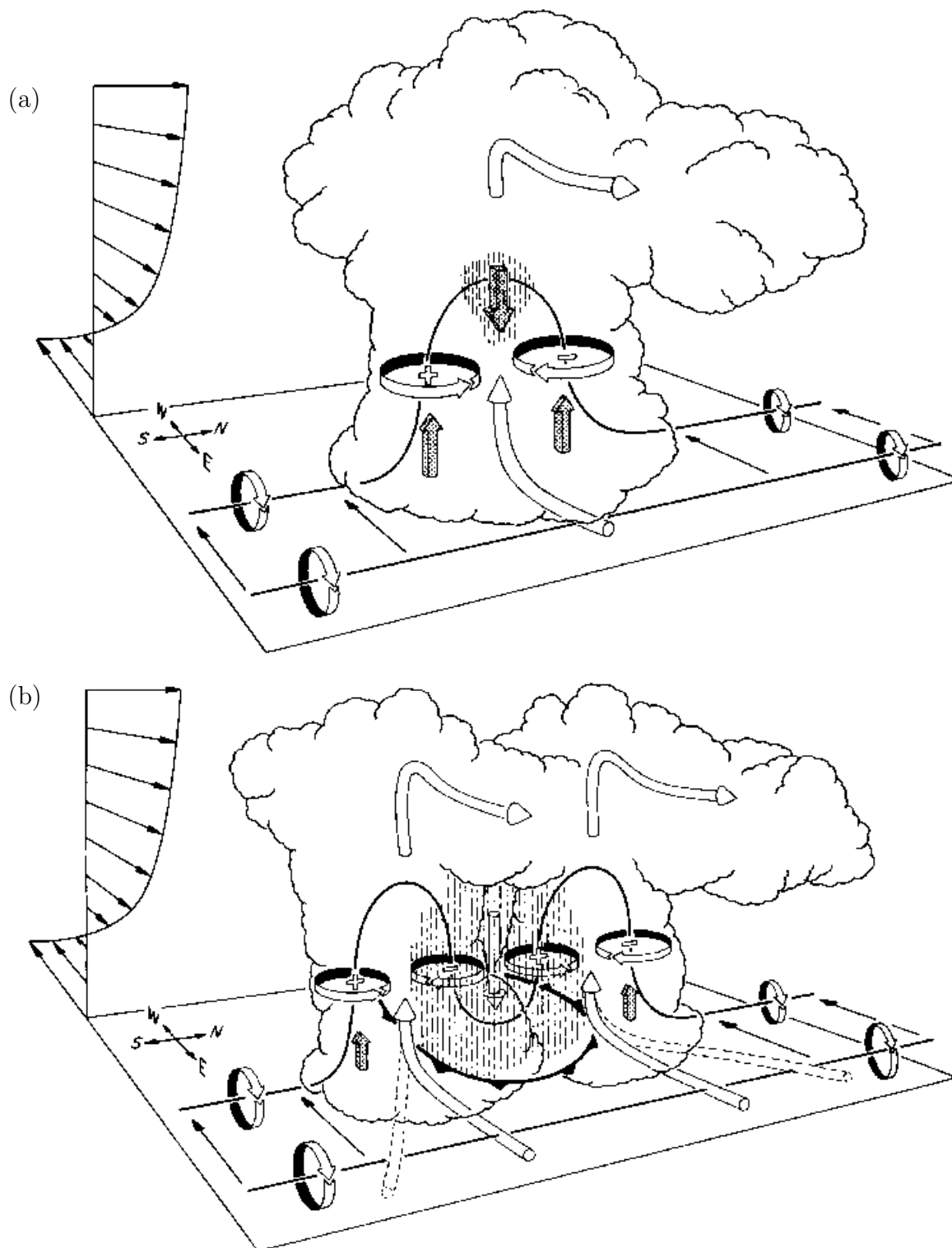
Figure 1.5: Schematic, illustrating how vortex tubes (solid lines) contained within an environment with unidirectional wind shear $[u = f(z), v = 0]$ are deformed as (a) the updraught grows, and (b) the downdraught forms between the splitting updraughts. Cylindrical white arrows show the direction of the inflow into the updraught, while gray shaded arrows represent the vertical pressure gradient forces. Precipitation is denoted by the vertical dashed lines and the barbed thick line at the ground marks the edge of the cold pool. (Adapted from Klemp 1987).
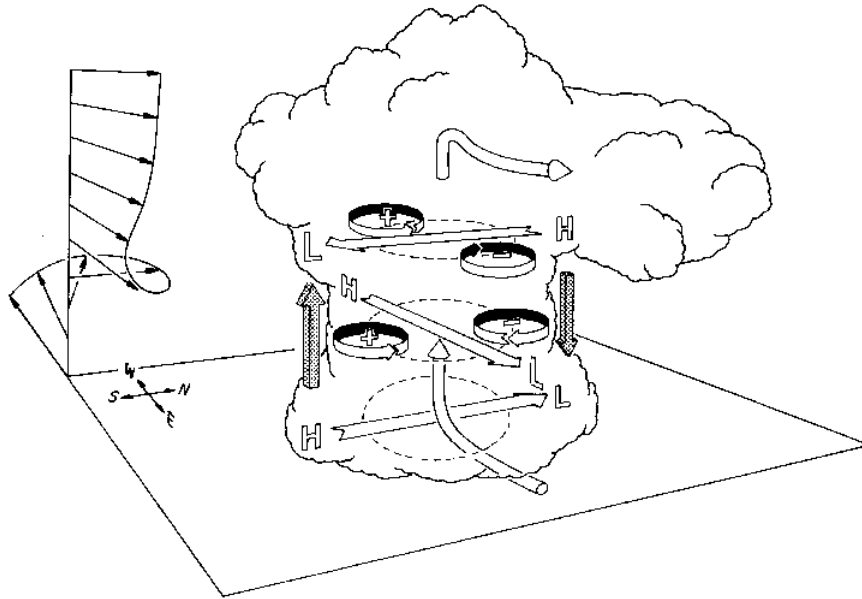
Figure 1.6: Schematic, depicting the influence of environmental wind shear turning clockwise with height on the initial updraught. Flat arrows represent the high (H) to low (L) horizontal pressure gradients parallel to the shear vectors, while grey shaded arrows depict the orientation of the vertical pressure gradients (Adapted from Klemp 1987).

height levels and mirror-image vortex pairs are created south and north of the updraught. However, when the shear vector turns clockwise with height, vertical pressure gradients favour ascent in the south and descent in the north. Figure 1.6 illustrates how these pressure gradients arise as the updraught interacts with the environmental wind shear. The development of a right-mover at the southern flank is enhanced, while the growth of the left-mover is inhibited.

## 1.5 Tropical thunderstorms – observations and forecasts

In the last two sections, the basic principles about thunderstorm dynamics were discussed, which are valid for thunderstorms in the mid-latitudes, and are presumed to be valid also for those in the tropics. However, the parameter regime in the mid-latitudes and tropics are different. For example, the tropopause height in the tropics is about 15–16 km and thus, much larger than that in the mid-latitudes which averages about 10 km. Further, the surface moisture in tropical environments is significantly larger than that in the mid-latitudes. These differences need to be considered when thunderstorms growing in these distinct environments are studied and compared with each other. In the following, some results of observations of tropical thunderstorms, and forecasting techniques used in the tropics are presented. Even though the focus is here on Darwin, much of this discussion is expected to be applicable to other tropical locations.

**Observations and measurements**

Convection around Darwin has been studied, *e.g.*, by Keenan and Carbone (1992), May and Ballinger (2007), and May and Rajopadhyaya (1999). In general, two types of flow regimes are observed in Darwin during the wet season (October to May): the monsoon flow regime and the flow during the break- and transition period. During the monsoon period, the thunderstorm systems develop in deep oceanic westerly flow with shears concentrated between $z = 0$ and 1.5 km. The thunderstorm updraughts are generally weak with storm tops between 10 and 15 km and large reflectivies, typically confined to below the melting level (Keenan and Carbone 1992).

During the break- and transition period flow, the shear regime is dominated by easterlies within the lowest 3 km. While the convective systems in this regime show, on average, smaller reflectivity than those in the monsoon period, the updraughts are more intense, thus leading to a larger electrical activity. One type of the break- and transition-season systems is the deep continental convection (with tops between 15 and 19 km), which occurs during the afternoon and evening. Another type of system is the maritime continent thunderstorm which is observed over the islands north of Darwin, among them, the famous thunderstorm complex "Hector", which develops regularly over the Tiwi Islands. Sea breeze initiated convection, which will be discussed in detail in section 1.7 and chapter 5, and the continental squall line are further types of convection occurring in the Darwin region. In northern Australia, the squall lines are sometimes initiated from a rainband of a tropical cyclone, or deep low in the Gulf of Carpentaria. The squalls occur in low CAPE and low shear environments as well as in moderate CAPE and large shear environments – comparable to those in the mid-latitudes. Indeed, the squall lines observed in the Darwin area can be very similar to those in the U.S.. However, it was found by Keenan and Carbone (1992) that these tropical systems grow in an environment with slightly larger low-level shear than the non-severe and severe U.S. squalls.

The amount of environmental CAPE in Darwin can vary significantly from day to day, and within each day. While in Keenan and Carbone (1992), environments with CAPE values of up to 3700 J kg$^{-1}$ were found, modified CAPE[6] values of more than 5000 J kg$^{-1}$ are mentioned in the Darwin Convective Analysis reports, or in the Severe Thunderstorm (STS) reports (see below and section 5.1). *To cover a large range of environmental instability, in this study thunderstorms are initialised in environments with CAPE values between 840 J kg$^{-1}$ and 6000 J kg$^{-1}$.*

An upper bound on vertical velocity $w$ in an atmosphere without vertical wind shear is given by

$$w_{max} = \sqrt{2 \times CAPE} \tag{1.6}$$

(Emanuel 1994). Using the CAPE values mentioned above, $w_{max}$ would expected to be as high as $\sqrt{2 \times 6000}$ m s$^{-1}$, however, CAPE does not consider entrainment and precipitation loading what can lead to a significant reduction in $w_{max}$. There is little literature on observations of the peak maximum vertical velocity within tropical thunderstorms. May and Rajopadhyaya (1999) reported vertical velocities in updraught cores, averaged over an 86-s time interval, greater than 15 m s$^{-1}$ - the 86-s time interval being the interval between successive measurements. As these velocities represent a time-average, and as

---

[6]The modified CAPE is the CAPE resulting from the modification of the 0000 UTC sounding, whereby the surface temperature and moisture are adjusted to provide an estimate of the afternoon convective potential.

some systematic life cycle effects are mixed into the dataset, it would be expected that the instantaneous vertical velocity is larger, although at this point it is not clear by how much. *Since the updraught strength of a thunderstorm is an important parameter, it will be investigated for modelled storms in tropical environments with different CAPE values, to examine whether Eq. (1.6) gives valid results.*

### Tropical thunderstorm forecasting and its challenges

One of the tools used at the Australian Bureau of Meteorology northwesterly Forecasting Centre in Darwin is the National Thunderstorm Forecast Guidance System (NTFGS). This system is based on the model runs carried out twice a day with the Meso-LAPS[7] model, and diagnoses favourable environments for severe weather phenomena, such as supercells, large hail, damaging winds, tornadoes, and microbursts.

The first steps of the "Darwin Convective Analysis", which is performed each morning at the Bureau of Meteorology, are the analysis of the convection that occurred during the previous 24 hours and the assessment of the NTFGS output. Data from the 0000 UTC sounding (9.30 am Central Standard Time) are input and modified to provide an estimate of the afternoon convective potential. The unmodified, "coastal", and "inland" CAPE, as well as the wind shear are then output. In further steps, the factors preventing thunderstorm occurrence, the timing, the probability of organisation, *etc.* are assessed. However, the modification of the temperature and shear profile may be difficult for the following reasons (Chappel 2001):

- The values of temperature, moisture, and wind shear, which are intended to represent afternoon conditions, can vary significantly depending on the time and location at which the convection develops (*e.g.*, ahead or behind the cooler and moister sea breeze air).

- The cold pool from pre-existing cells can trigger convection when colliding with each other or with the sea breeze boundary. The determination of the pattern of low-level convergence and of the characteristics of the lifted parcel is difficult.

- Small differences in the surface dew point temperatures may result in large CAPE differences, which might lead to incorrect forecasts.

Beside these difficulties, problems arise because of the lack of information about tropical thunderstorms. There are some numerical case studies of the island thunderstorm Hector (Crook 2001), tropical squall lines (Lafore and Moncrieff 1989), supercells in hurricane environments (McCaul and Weisman 1996), and convection behind a sea breeze front (Rao and Fuelberg 2000). However, idealised numerical simulations of tropical thunderstorms that investigate the influence of environmental parameters, such as CAPE, wind shear, and relative humidity, on the storm evolution do not exist. Moreover, it is unknown whether the findings for mid-latitude thunderstorms are applicable to those in the tropics. For example, CAPE/shear diagrams, such as in Fig. 3 of Chappel (2001) are used at the Forecasting Centre in Darwin, but represent mainly convective regimes observed in mid-latitude studies. The question is here whether the parameter regimes are the same in tropical and mid-latitude environments. Further, the NTFGS used for forecasting thunderstorms around

---

[7]Limited Area Prediction System
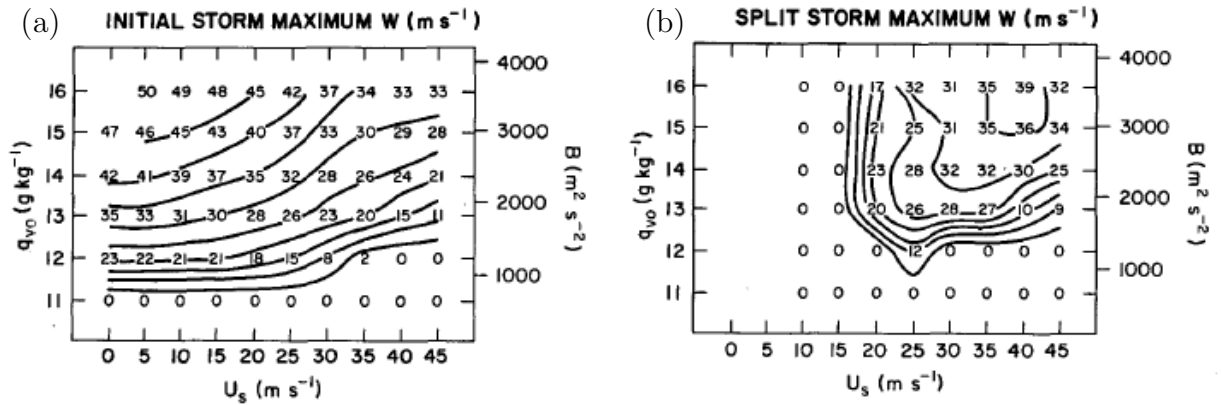
Figure 1.7: Maximum vertical velocity $w$ in m s$^{-1}$ for (a) the initial storm, and (b) split storms. The vertical wind shear magnitude $U_s$ is plotted on the abscissa, while buoyant energy, given in units of $q_{v0}$ and CAPE, is plotted on the ordinate. Zero values in (a) mean that $w < 2$ m s$^{-1}$, *i.e.*, that a strong updraught did not develop. (Adapted from WK82).

Darwin, was designed for forecasting mid-latitude storms. However, the experience of the forecasters in Darwin reveals that the NTFGS seems to over-forecast supercells within the Darwin region.

*These uncertainties and limitations due to the paucity of tropical thunderstorm studies motivated the work described in this thesis. The aim of the latter is to study deep convection using an idealised numerical model, to examine how CAPE and vertical wind shear determine the severity of a thunderstorm in a tropical environment. Further, it is investigated how the parameter regime differs in both environments and whether the diagnostic variables used to forecast mid-latitude storms are applicable also to those in the tropics.* To allow a comparison of the results obtained for tropical thunderstorms with those obtained for mid-latitude thunderstorms, I discuss next the important numerical modelling studies of mid-latitude storms.

## 1.6 Mid-latitude thunderstorms – numerical simulations

The influence of uni-directional vertical wind shear and buoyancy on deep convection in the mid-latitudes was studied in a ground-breaking paper by WK82. Deep convection was initialised in environments with different surface water vapour mixing ratios, $q_{v0} = 11$ to 16 g kg$^{-1}$, giving values of CAPE ranging from 1000 to 3600 J kg$^{-1}$. The horizontal wind was defined as:

$$u(z) = U_s \tanh\left(\frac{z}{z_s}\right), \tag{1.7}$$

where $z$ is the height, $z_s$ a constant, and $U_s$ is proportional to the vertical wind shear.

It was found that for a given amount of buoyant energy, the maximum updraught speed of the initial storm cell decreases as the wind shear increases (see Fig. 1.7a). This decrease in storm strength is due to the increased entrainment into the thunderstorm as the shear increases. If the strength of the wind shear is held constant, the updraught strength

increases with increasing CAPE. As can be seen in Fig. 1.7a, storms develop only when the amount of environmental buoyancy is sufficiently large ($q_{v0} \geq 12$ g kg$^{-1}$), and when the wind shear in environments with small CAPE is not too high.

In the experiments with a surface mixing ratio of 14 g kg$^{-1}$, single cells occur if the environmental shear is zero or weak ($U_s \leq 10$ m s$^{-1}$), while for $U_s = 15$ m s$^{-1}$, a "secondary storm" develops, that shows many features typical of observed multicells. If the shear in the model is increased even further ($U_s \geq 20$ m s$^{-1}$, see Fig. 1.7b), splitting occurs and the two resulting supercells propagate transverse to the mean wind, *i.e.*, towards the south and north. Weisman and Klemp point out that an important factor for the development of steady split storms is that the flow of environmental air into the storm is strong enough to keep the gust front from moving away from the updraught. If the cold pool is too strong, it propagates too far away from the updraught, cutting off the storm from the warm inflow, and causing the updraught to weaken. *In chapters 3 to 5, it will be shown that the gust front speed, time of occurrence, and the temperature distribution within the cold pool are of utmost importance in determining whether a thunderstorm splits.*

Weisman and Klemp chose the Richardson number

$$R = \frac{CAPE}{\frac{1}{2}\bar{u}^2} \tag{1.8}$$

as a measure of the competing effects of vertical wind shear and buoyancy on thunderstorm development. In Eq. (1.8), $\bar{u}$ is the difference between the density-weighted mean wind speed at low- and at mid-levels. Using the upper bound on vertical velocity given by Eq. (1.6), the Richardson number can be interpreted as the ratio of the potential updraught strength to the inflow kinetic energy available to the thunderstorm. WK82 gave thresholds of $R$ for when multi- and splitcells can be expected. They found that splitting occurs for $10 < R < 50$, which compares well with the observations in mid-latitude supercell cases in which $R$ lies in the range $15 < R < 35$. *The Richardson number, along with the validity of these thresholds will be examined for tropical thunderstorms in section 3.2.2.*

As described in section 1.3, uni-directional wind shear, causing two mirror-image storms, is rare in nature. It is more usual that the wind vector veers with height. The effects of a directional wind shear on storm evolution was numerically studied in Weisman and Klemp (1984, hereafter WK84) and Gilmore *et al.* (2004). WK84 used a clockwise curved hodograph and found that multicellular type growth is confined mainly to the initial storm's left flank for lower shears, while supercellular type growth is favoured on the right flank for high values of the shear. It was shown that the updraughts on the left flank are primarily forced by low-level convergence along the gust front, while those on the right flank are influenced by dynamically induced vertical pressure gradients. If a curved hodograph is used, Eq. (1.8) changes to

$$R = \frac{CAPE}{\frac{1}{2}(\bar{u}^2 + \bar{v}^2)},$$

where $\bar{u}$ and $\bar{v}$ represent the difference between the density weighted mean wind speed at low- and at mid-levels of the $u$ and $v$ wind components, respectively. In WK84, right flank cells (supercells) became stronger with decreasing $R$, however, storms were unable to develop for $R < 12$. In an environment with $R \approx 25$, supercells are considered to be most likely, although multicellular convection is possible also. WK84 note that $R$ is a useful parameter for predicting the type of modelled storms in environments with uni-directionally

and directionally varying wind shear. Further, WK84 propose a dynamically-based thunderstorm classification scheme with two major classes of convective cells: supercells and "ordinary cells", *i.e.*, single cells. Then, multicell complexes and squall lines are composed of these two major storm types. Gilmore *et al.* (2004) repeated the WK84-simulations, using, *inter alia*, ice microphysics. The inclusion of ice lead to stronger storm updraughts due to more latent heat release during fusion, and to colder downdraughts via melting of hail than in the model experiments without ice. *The inclusion of ice in the microphysics scheme is discussed in section 3.3 and how directionally varying wind shear affects tropical thunderstorms is investigated in chapter 4.*

One problem with the Richardson number $R$ is that it cannot take into account all environmental conditions and effects, *e.g.*, the shape of the buoyancy profile, convective inhibition[8], and the vertical moisture distribution. The sensitivity of the storm characteristics to the shape of the buoyancy and shear profile, as well as to the environmental moisture distribution was studied by McCaul and Weisman (2001), and McCaul *et al.* (2005). It was found that when thunderstorms grow in an environment where the buoyancy profile has a maximum at low-levels as it is typically found in the mid-latitudes, the maximum vertical velocity in the updraught is large and the downdraught is strong. In comparison, when the buoyancy is evenly distributed through the depth of the troposphere, *i.e.*, when the low-level buoyancy is smaller as is typically found in the tropics, the up- and downdraughts produced are weaker. However, this dependence of the updraught and downdraught strength on the height of maximum buoyancy was shown to be reduced once CAPE values were equal to, or exceeded 2000 J kg$^{-1}$. The study of storms growing in environments with different water vapour mixing ratios $q_v$, but where everything else is kept constant, showed that when the low-levels have a large $q_v$, the subsequent high condensation loading in the updraught can produce a strong downdraught regardless of the buoyancy profile. *The influence that the low-level moisture and precipitation loading have on the evolution of a thunderstorm will be examined in sections 3.2.3 and 4.2.2, by initialising storms in environments with different temperature and moisture profiles.*

The foregoing description covers only a small fracture of mid-latitude thunderstorm studies, but these studies are considered to be the most important ones for this thesis.

## 1.7 Tropical deep convection influenced by sea breezes

In this thesis, I investigate the effect of CAPE and environmental wind shear on thunderstorm development in the tropics and also how a density current, here a sea breeze, can influence the evolution of a thunderstorm or thunderstorm system. Studies of sea breezes in the tropics have shown that the convergence caused by sea breezes can trigger thunderstorms (*e.g.*, Carbone *et al.* 2000, Keenan and Carbone 1992). In their study of convection in the Darwin area, Keenan and Carbone (1992) found that initial convective features tend to evolve towards a line of thunderstorms, which is oriented perpendicular to the low-level shear and shows forward-moving squall-like characteristics. A particular phenomenon occurring in the Darwin region is the so-called "Northeaster", which is a multicellular storm complex approaching the coastal city from the northeast. It is believed that the sea breezes play an important role in the evolution of these storms, which can

---

[8]Convective inhibition (CIN) represents the amount of energy that will prevent an air parcel from rising from the surface to the level of free convection.
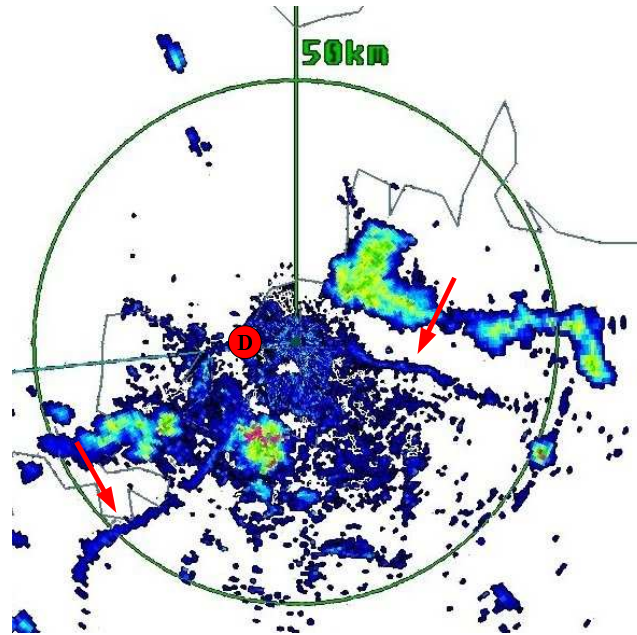
Figure 1.8: Berrimah radar image at 0420 UTC on 14 November 2005. Colours represent the reflectivity, where a reflectivity of 0 to $-20$ dBZ is shaded in dark blue, $-20$ to $-40$ dBZ in light blue/yellow, and $-40$ to $-65$ dBZ in green/red. The city of Darwin is marked by a large red dot, and the red arrows point to convective development at the sea breeze fronts. Courtesy of the Australian Bureau of Meteorology northwesterly Forecasting Centre in Darwin.

even be severe. However, no numerical studies exist which might confirm this hypothesis, or which can help to understand the phenomenon in detail.

Rao and Fuelberg (2000) investigated deep convection behind the Cape Canaveral sea breeze front with the use of a three-dimensional numerical model. They found that in a region where storm development was suppressed by subsidence from a neighboring cell, a new storm developed within this region when surface lifting was provided by an outflow boundary. Kingsmill (1995) examined the initiation of convection associated with the collision of a sea breeze front and a gust front using observational data collected in summer months in Florida. He found that inflections or kinks in the boundary layer convergence zone can be preferred areas of convection initiation. However, the studies of Kingsmill (1995) and Rao and Fuelberg (2000) did not address the role of the low-level vertical wind shear provided by the sea breeze.

Figure 1.8 shows a radar image of the Darwin region at 0420 UTC on 14 November 2005, where the northerly and the northwesterly sea breeze front are apparent due to convective development (red arrows). Both the southward and southeastward moving sea breezes have triggered strong convection already, and the thunderstorm system (a Northeaster) behind the northerly sea breeze front intensifies further to cross the city of Darwin at about 0500 UTC. *In chapter 5 of this thesis, the overall evolution of two Northeasters will be investigated, with the focus on examing how the additional lifting and low-level vertical wind shear provided by the sea breeze(s) lead to the formation of a severe multicell complex.*

## 1.8　Overview of chapters

In the following chapter, the two numerical cloud-models used to conduct the experiments are described and the general settings are specified. The influence of uni-directional vertical wind shear and buoyancy on deep convection is examined in chapter 3. This investigation attempts to identify the differences between the evolution of thunderstorms in the tropics and the mid-latitudes, and to explore whether the Richardson number, along with its thresholds used to classify the thunderstorm type in the mid-latitudes, apply for thunderstorms in the tropics. In chapter 4, the effect of directionally-varying wind shear on the evolution of a tropical thunderstorm is discussed and compared to the results obtained for mid-latitude thunderstorms. In chapter 5, the results of the simulations of a severe and a non-severe northeaster are presented. The focus lies on the question under which circumstances a long-lived multicell complex can form and to which extent the environmental wind and the sea breeze have an influence on the formation of a thunderstorm system behind the sea breeze front. A summary of the important findings and parameters used in the study is given in chapter 6, and suggestions are made how these findings are applicable to improve the forecasts of severe thunderstorms. A summary of the results and conclusions are presented in chapter 7.

# Chapter 2

# The numerical models

The two numerical models used in this study are the three-dimensional, non-hydrostatic cloud-scale model of Bryan and Fritsch (2002) and Bryan (2002) and the three-dimensional, non-hydrostatic Clark-Hall cloud-scale model (Clark 1977). This chapter provides a short description of both numerical models. The model configurations for specific experiments are described at the beginning of each individual chapter where they are used. A list of principal symbols utilised in the following sections is given in Appendix B.

## 2.1   Clark-Hall cloud-scale model

The simulations of deep convection in an environment with uni-directional wind shear presented in chapter 3 of this thesis are, *inter alia*, carried out with Clark's model. This three-dimensional non-hydrostatic cloud model was developed at the National Center for Atmospheric Research (NCAR) in the 70s and 80s. During the last decades, phenomena such as convective clouds, squall lines (Lafore and Moncrieff 1989), sea breezes, and cloud lines (*e.g.*, Goler *et al.* 2006) have been studied with Clark's model. Details of the model can be found, *inter alia*, in Clark (1977), and Clark (1979). The model equations, model flow structure, parameters and switches, data flow and storage, filters, pressure solvers, nesting procedures, and physical parameterisations are described in detail in the model documentation (Clark *et al.* 1996). A brief summary is given below.

### 2.1.1   The governing equations

The model uses the deep anelastic approximation of Ogura and Phillips (1962), with the momentum equations given by

$$\frac{Du}{Dt} + f^* w - fv = -\frac{1}{\bar{\rho}}\frac{\partial p}{\partial x} + \frac{1}{\bar{\rho}}M_1 + RF_1, \tag{2.1}$$

$$\frac{Dv}{Dt} + fu = -\frac{1}{\bar{\rho}}\frac{\partial p}{\partial y} + \frac{1}{\bar{\rho}}M_2 + RF_2, \tag{2.2}$$

$$\frac{Dw}{Dt} - f^* u = -\frac{\partial}{\partial z}\frac{p}{\bar{\rho}} + B + \frac{1}{\bar{\rho}}M_3 + RF_3, \tag{2.3}$$

where the material derivative is defined as

$$\frac{D}{Dt} = \frac{\partial}{\partial t} + u\frac{\partial}{\partial x} + v\frac{\partial}{\partial y} + w\frac{\partial}{\partial z}. \tag{2.4}$$

In equations (2.1) to (2.4), $(u, v, w)$ are the Cartesian velocity components in the $(x, y, z)$ directions, $p$ is the perturbation pressure, and $\bar{\rho}$ is the density. The buoyancy $B$ is given as

$$B = g\left[\frac{\theta - \bar{\theta}}{\bar{\theta}} + \epsilon_c \left(q_v - \bar{q}_v\right) - q_c - q_r - q_{iA} - q_{iB}\right], \tag{2.5}$$

where $\theta$ is the potential temperature, and $q_v$, $q_c$, $q_r$, $q_{iA}$, and $q_{iB}$ are the mixing ratios of water vapour, cloud water, rain water, ice Type A, and ice Type B, respectively. The two types of ice are defined in section 2.1.3. Variables with overbars represent unperturbed environmental (vertical) profiles. $M_1$, $M_2$, and $M_3$ are the subgrid-scale momentum closure terms in the $x$, $y$ and $z$ direction, respectively. The terms $RF_1$, $RF_2$, and $RF_3$ describe the Rayleigh friction absorber used in conjunction with the upper boundary (described in section 2.1.2). $\epsilon_c$ is a constant, given by $R_v/R_d - 1$, and the Coriolis parameter $f$ is $2\Omega \sin \phi$, and $f^* = 2\Omega \cos \phi$, with $R_v$ and $R_d$ being the gas constants for moist and dry air, respectively, $\phi$ being the latitude, $\Omega$ being the angular speed of rotation of the Earth and $g$ being the acceleration due to gravity. Note, that the Coriolis parameter is set to zero in all simulations of this study. The anelastic continuity equation is given as

$$\frac{\partial u}{\partial x} + \frac{\partial v}{\partial y} + \frac{1}{\bar{\rho}}\frac{\partial \bar{\rho}w}{\partial z} = 0, \tag{2.6}$$

and the thermodynamic equation is

$$\frac{D\theta}{Dt} = S_\theta + \frac{1}{\bar{\rho}}M_h, \tag{2.7}$$

where $S_\theta$ is the local source term for $\theta$, and $M_h$ is the subgrid-scale heat closure.

## 2.1.2 Numerics

### Boundary conditions

In Clark's model, the upper boundary is rigid and formulated as a "no-stress" boundary where the vertical velocity $w$ vanishes. In order to suppress vertically propagating wave reflections from the rigid wall, a Rayleigh friction absorber (damper) is included via the terms $RF_1$, $RF_2$, and $RF_3$ [see Eqs. (2.1) – (2.3)]. In the calculations presented in chapter 3, this "sponge-layer" occupies the uppermost 10 levels (10 km) of the model domain.

The surface boundary is rigid, also, but is imposed with a surface stress, which is related to the fluid velocity at the first grid level and to the drag coefficient. The drag coefficient is zero and thus, produces a free-slip lower boundary for the studies presented in this thesis. The lateral boundary conditions in the model experiments are set to be "open".

### Grid coordinates

The complete set of equations is approximated on a regular finite difference grid where $x$, $y$, and $z^*$ are defined as

$$x = \left(i - \frac{3}{2}\right)\Delta x, \;\; y = \left(j - \frac{3}{2}\right)\Delta y, \;\; z^* = \left(k - \frac{3}{2}\right)\Delta z^*,$$

with $i$, $j$, $k$ running from 1 to $NX$, $NY$, and $NZ$, respectively. The field variables are located on a staggered grid:

$$u = u\left(i \pm \frac{1}{2}, j, k\right), \quad v = v\left(i, j \pm \frac{1}{2}, k\right), \quad w = w\left(i, j, k \pm \frac{1}{2}\right), \qquad (2.8)$$

and

$$\psi = \psi(i, j, k),$$

where $\psi$ stands for the density $\rho$, temperature $T$, potential temperature $\theta$, or perturbation pressure $p$. The finite difference equations are integrated forward in time using the Smolarkiewicz multi-dimensional positive definite advection scheme, which ensures second-order accuracy in space and time.

### 2.1.3   Cloud microphysics

The cloud microphysics in Clark's model is represented by a Kessler-type, or warm rain, parameterisation, where only vapour and liquid processes are considered, and a parameterisation of two ice types A and B. Type A ice represents particles that are initially small and are created either by heterogeneous ice nucleation from water vapour or by homogeneous ice nucleation from cloud water. Type B ice particles are initially larger, having been created when a raindrop freezes after the collision with a type A ice particle. Simulations using the Kessler and ice microphysics scheme were carried out for this thesis. However, during the course of this study it was found that Clark's model is less suitable for simulations of deep convection with the ice phase included, as in some cases no, or only an extremely weak gust front was produced. This shortcoming was deemed to be unrealistic. Thus, only the simulations using the warm rain microphysics scheme in Clark's model are presented in chapter 3.

## 2.2   Bryan Cloud Model (CM1)

The majority of the numerical calculations presented in this thesis, including the wind shear experiments of chapters 3 and 4, and the sea breeze simulations of chapter 5, are performed using Bryan's model (CM1, Version 1, Release 11 from 23 October 2006). By rerunning the wind shear experiments, which are carried out also with Clark's model, the sensitivity of the results to a particular model can be assessed (see chapter 3). In contrast to Clark's model, it is found that CM1 produces physically realistic gust front characteristics when an ice microphysics scheme is used.

CM1 is a three-dimensional, non-hydrostatic numerical model that was developed by Bryan and Fritsch at The Pennsylvania State University. Designed primarily for idealised research, the difference between this and other modern cloud-models is that CM1 conserves mass and energy better [*e.g.*, Pennsylvania State University/National Center for Atmospheric Research mesoscale model (MM5), Advanced Regional Prediction System (ARPS), Regional Atmospheric Modeling System (RAMS)]. Details about the model can be found in Bryan and Fritsch (2002) and Bryan (2002) and can be obtained from the CM1 webpage[1].

---

[1]http://www.mmm.ucar.edu/people/bryan/cm1

## 2.2.1 The governing equations

**Thermodynamic and pressure equation**

In Bryan (2002), prognostic equations for the non-dimensional pressure (or Exner Function)

$$\pi \equiv \left(\frac{p}{p_{00}}\right)^{\frac{R_d}{c_p}}, \tag{2.9}$$

and for the dry air potential temperature

$$\theta \equiv \frac{T}{\pi}, \tag{2.10}$$

are derived:

$$
\begin{aligned}
\frac{D\ln\pi}{Dt} =& -\frac{R_d}{c_p}\frac{c_{pml}}{c_{vml}}\frac{\partial u_j}{\partial x_j} + \\
&+\frac{R_d}{c_p}\left[\left(\frac{L_v}{c_{vml}T} - \frac{R_v c_{pml}}{R_m c_{vml}}\right)\dot{q}_{cond} + \left(\frac{L_s}{c_{vml}T} - \frac{R_v c_{pml}}{R_m c_{vml}}\right)\dot{q}_{dep} + \frac{L_f}{c_{vml}T}\dot{q}_{frz}\right],
\end{aligned}
$$

and

$$
\begin{aligned}
\frac{D\ln\theta}{Dt} =& -\left(\frac{R_m}{c_{vml}} - \frac{R_d}{c_p}\frac{c_{pml}}{c_{vml}}\right)\frac{\partial u_j}{\partial x_j} + \frac{c_v}{c_p c_{vml}T}(L_v\dot{q}_{cond} + L_s\dot{q}_{dep} + L_f\dot{q}_{frz}) \\
&-\frac{R_v}{c_{vml}}\left(1 - \frac{R_d}{c_p}\frac{c_{pml}}{R_m}\right)(\dot{q}_{cond} + \dot{q}_{dep}),
\end{aligned}
$$

where $p_{00} = 1000$ hPa is the reference pressure; $c_p$ and $c_{pv}$ are the specific heat of dry air and water vapour at constant pressure; $R_d$, $R_m$, and $R_v$ are the gas constants of dry air, moist air, and water vapour, respectively; $L_f$, $L_s$, and $L_v$ are the latent heat of freezing, sublimation and vaporisation; $\dot{q}$ is the change of the mixing ratio with time, whereby the subscripts *cond*, *dep*, and *frz* stand for "condensation", "deposition", and "freezing", respectively.

**Momentum equation and the equation of state**

The momentum equation is expressed originally as

$$\frac{Du_i}{Dt} = -\frac{1}{\rho}\frac{\partial p}{\partial x_i} - \delta_{i3}g, \tag{2.11}$$

with the material derivative defined by

$$\frac{D}{Dt} = \frac{\partial}{\partial t} + u_j\frac{\partial}{\partial x^j}, \tag{2.12}$$

and with the density given as

$$\rho = \rho_a(1 + q_t). \tag{2.13}$$

$u_i$ is the velocity vector, with $i = 1, 2, 3$, pointing in the direction $x_i$. The symbol $\rho_a$ stands for the density of dry air and $q_t$ is the sum of the mixing ratios of water vapour $q_v$, cloud water $q_c$, rain $q_r$, snow $q_s$, ice $q_i$, and hail/graupel $q_g$. In Eqs. (2.11) and (2.12),

Einstein summation convention is used where the subscript $i = 1$, 2, 3 stands for the $x$, $y$, and $z$ components, respectively, and $\delta_{ij}$ is the Kronecker delta. With Eq. (2.9) and the equation of state

$$p = \rho_a R_d T_v = \rho_a R_d T \left(1 + \frac{q_v}{\epsilon}\right), \text{ with } \epsilon = \frac{R_d}{R_v}, \tag{2.14}$$

the pressure gradient term of Eq. (2.11) can be rewritten in terms of the non-dimensional pressure $\pi$, giving

$$\frac{Du_i}{Dt} = -c_p \theta_\rho \frac{\partial \pi}{\partial x_i} - \delta_{i3} g, \tag{2.15}$$

where $\theta_\rho$ is the density potential temperature, which includes the contribution of condensate loading to density (Emanuel 1994):

$$\theta_\rho \equiv \theta \, \frac{1 + (q_v/\epsilon)}{1 + q_t}. \tag{2.16}$$

Expressing $p$, $\pi$, $\theta$, and $q_v$ as the sum of a mean and a deviation component, assuming that the base state fields are in hydrostatic balance

$$\frac{dp_0}{dz} = -\rho_0 g(1 + q_{v0}), \tag{2.17}$$

and that the base state momentum as well as the liquid and ice water mixing ratios are zero, the final momentum equation is given by

$$\frac{Du_i}{Dt} = -c_p \theta_\rho \frac{\partial \pi'}{\partial x_i} + \delta_{i3} \, g \left(\frac{\theta_\rho}{\theta_{\rho 0}} - 1\right). \tag{2.18}$$

Bryan (2002) notes that, in contrast to that of other models, the buoyancy term, the last term on the right hand side of Eq. (2.18), is exact as no Taylor series approximations are necessary for the derivation.

The first term on the right hand side of Eq. (2.18) is often called the perturbation pressure gradient force term and the second term is named the buoyancy force term. Note that the buoyancy force is not uniquely defined because it depends on the (arbitrary) choice of a reference density (Smith *et al.* 2005). Further, the pressure perturbation $\pi'$ has a source due to buoyancy and a dynamic source. This can be seen by multiplying Eq. (2.18) with a mean density $\rho_0$ and by applying the divergence $\partial/\partial x^i$, yielding:

$$\frac{\partial}{\partial t}\left[\frac{\partial}{\partial x^i}(\rho_0 u_i)\right] = -\frac{\partial}{\partial x^i}\left(\rho_0 u_j \frac{\partial u_i}{\partial x^j}\right) - c_p \frac{\partial}{\partial x^i}\left(\rho_0 \theta_\rho \frac{\partial \pi'}{\partial x_i}\right) + \delta_{i3} \frac{\partial}{\partial x^i}\left[\rho_0 g \left(\frac{\theta_\rho}{\theta_{\rho 0}} - 1\right)\right]. \tag{2.19}$$

The term on left hand hand side of Eq. (2.19) vanishes due to the anelastic continuity equation $\partial/\partial x^i(\rho_0 u_i) = 0$, giving

$$c_p \frac{\partial}{\partial x^i}\left(\rho_0 \theta_\rho \frac{\partial \pi'}{\partial x_i}\right) = -\frac{\partial}{\partial x^i}\left(\rho_0 u_j \frac{\partial u_i}{\partial x^j}\right) + \delta_{i3} \frac{\partial}{\partial x^i}\left(\rho_0 B\right), \tag{2.20}$$

with $B = g(\theta_\rho/\theta_{\rho 0} - 1)$. In solving the pressure equation, the pressure can be divided into two parts $\pi' = \pi'_{dyn} + \pi'_B$, where $\pi'_{dyn}$ represents the contributions to pressure from the dynamic terms, the first term on the right hand side of Eq. (2.20), while $\pi'_B$ is the

contribution from the buoyancy term, the last term on the right hand side of Eq. (2.20). Thus, the momentum equation (2.18) can be rewritten as

$$\frac{Du_i}{Dt} = \underbrace{-c_p \theta_\rho \frac{\partial \pi'_{dyn}}{\partial x_i}}_{\text{dynamic forcing}} \underbrace{- \left[ c_p \theta_\rho \frac{\partial \pi'_B}{\partial x_i} - \delta_{i3} \, g \left( \frac{\theta_\rho}{\theta_{\rho 0}} - 1 \right) \right]}_{\text{buoyancy forcing}}. \tag{2.21}$$

## 2.2.2 Numerics

As in Clark's model [see Eqs. (2.8)], the grid points in CM1 on which momentum is calculated are staggered one-half grid spacing from the locations of the scalars (e.g., $\theta$, $q_n$, $\pi$). For all simulations presented in this work, the grid spacings in the horizontal directions are constant, while a stretched grid is used in the vertical (see Tables 3.1 and 4.1).

In order to maintain mass conservation in CM1, $w$ is set equal to zero at the upper and lower boundaries. Thus, as the upper boundary is a rigid lid, as in Clark's model, a sponge-layer is implemented in the uppermost 10 km to inhibit the reflection of waves from the top. In CM1, three different lateral boundary conditions can be selected: periodic, rigid walls, and open radiative. The latter boundary condition has been chosen for all the model experiments carried out for this thesis.

## 2.2.3 Cloud microphysics

In CM1, several moisture schemes are implemented. One of the schemes used for this study is the water-only parameterisation of Kessler, which is based on the equations presented in Klemp and Wilhelmson (1978). The use of this scheme in Bryan's model allows a comparison with the experiments carried out with Clark's model (see chapter 3).

The second moisture parameterisation scheme used here is the Gilmore–Straka– Rasmussen version of the Lin-Farley-Orville (LFO) scheme (see Lin *et al.* 1983, Gilmore *et al.* 2004). In this scheme the water vapour $q_v$, cloud water $q_c$, and rain water $q_r$ mixing ratios are build in, along with the cloud ice $q_i$, snow $q_s$, and hail/graupel $q_g$ mixing ratios. The smaller particles (cloud ice and cloud water) are monodisperse, while the larger particles (rain, snow, and hail/graupel) are defined by inverse-exponential size distributions. By carrying out the experiments with and without ice, the sensitivity to the results in terms of the microphysics can be studied (see chapter 3).

# Chapter 3

# The influence of uni-directional vertical wind shear on convection

Idealised model experiments of deep convection are perhaps the main tool one can use to investigate the role of environmental parameters, such as wind shear and buoyancy, on thunderstorm evolution. In this chapter the influence of uni-directional wind shear on deep convection in the tropics will be investigated and the results compared to those of numerical studies performed for mid-latitude thunderstorms. The model configuration and the experiments will be described in subsection 3.1 and the results of the model runs carried out without ice microphysics in Bryan's and Clark's model will be discussed in subsection 3.2. The effect of the inclusion of ice microphysics on thunderstorm evolution is examined in subsection 3.3 and the sensitivity of the model results to the horizontal resolution, thermal perturbation, and wind profile used is investigated in subsection 3.4. The conclusions are presented in subsection 3.6. A major part of the work in this chapter has been published in Wissmeier and Goler (2009).

## 3.1   Model configuration and experiments

The influence of uni-directional vertical wind shear on convection is studied using the Clark-Hall cloud-scale model and the Bryan Cloud Model (CM1). Table 3.1 shows an overview of the settings and parameters used here and of those chosen in Weisman and Klemp (1982, hereafter WK82). The vertical domain size in Bryan's and Clark's model is larger than in WK82, due to the need to model tropical thunderstorms, which are deeper than mid-latitude thunderstorms. Further, the horizontal grid spacing in Bryan's and Clark's model is 1 km, instead of 2 km as in WK82, and the horizontal domain size is (60 × 60) km$^2$, instead of (40 × 60) km$^2$, so that the storms remain inside the domain longer.

**Temperature and moisture profiles**

The simulations of mid-latitude thunderstorms carried out by Weisman and Klemp (1982) are rerun with Bryan's and Clark's model to provide a basis for the comparison with the tropical thunderstorm simulations. The results of these mid-latitude simulations are then compared with those of WK82 to examine the performance of Bryan's and Clark's model. Mid-latitude thunderstorms are produced by initialising Bryan's and Clark's model with

| Parameter | Bryan | Clark | WK82 |
|---|---|---|---|
| Horizontal domain size | $(60 \times 60)$ km$^2$ | $(60 \times 60)$ km$^2$ | $(40 \times 60)$ km$^2$ |
| Horizontal grid $\Delta x$, $\Delta y$ | 1 km | 1 km | 2 km |
| Vertical domain size | 36 km | 36 km | 17.5 km |
| Vertical grid $\Delta z$ | $(0.3 - 1)$ km | $(0.35 - 1)$ km | $(0.35 - 1)$ km |
| Microphysics | Kessler, ice | Kessler | Kessler |
| Warm bubble width $(2 \times r)$ | 8 km or 20 km | $(6 - 20)$ km | 20 km |
| Warm bubble depth $(2 \times h)$ | 1 km or 2.8 km | 1 km or 2.8 km | 2.8 km |
| Warm bubble excess $(\Delta\theta)$ | 8 K or 2 K | $(2 - 8)$ K | 2 K |

Table 3.1: Experiments with a straight-line hodograph: Comparison of various parameters set in Bryan's and Clark's model, and used in WK82.

the thermodynamic profile from WK82. The environmental potential temperature $\theta(z)$ and the relative humidity $RH(z)$ are given by:

$$\theta(z) = \begin{cases} \theta_0 + (\theta_{tr} - \theta_0)\left(\frac{z}{z_{tr}}\right)^{\frac{5}{4}} & \text{for } z \leq z_{tr}, \\ \theta_{tr} \exp\left[\frac{g}{c_p T_{tr}}(z - z_{tr})\right] & \text{for } z > z_{tr}, \end{cases} \quad (3.1)$$

$$RH(z) = \begin{cases} 1 - \frac{3}{4}\left(\frac{z}{z_{tr}}\right)^{\frac{5}{4}} & \text{for } z \leq z_{tr}, \\ 0.25 & \text{for } z > z_{tr}, \end{cases} \quad (3.2)$$

where $z_{tr} = 12$ km, $\theta_{tr} = 343$ K, and $T_{tr} = 213$ K represent the height, potential temperature, and actual temperature at the tropopause, respectively, and $\theta_0 = 300$ K is the potential temperature at the surface. The atmospheric instability is varied by defining surface mixing ratio values $q_{v0}$ of 12, 14, and 16 g kg$^{-1}$, which are kept constant in a 1 km deep layer near the surface to approximate a well-mixed boundary layer. The resulting CAPE[1] values are: 840 J kg$^{-1}$, 1893 J kg$^{-1}$, and 2917 J kg$^{-1}$, respectively. Figure 3.1a shows the skew$T$-log$p$ diagram where the temperature and dew-point temperature of the mid-latitude experiment with $q_{v0} = 14$ g kg$^{-1}$ are depicted in black (dashed lines).

The tropical storm environment is generated by initialising each model with the vertical temperature and moisture profile from the 0000 UTC Darwin sounding (0930 local time) on days when either severe or non-severe thunderstorms occurred. Profiles for three days are considered (YYMMDD = 051114, 011120, 041217), together with an average of three profiles (see Fig. 3.1a, blue solid lines). To represent the mid-afternoon conditions when the storms on these days developed, the lowest 1 km of each sounding is modified to give a convectively well-mixed boundary layer, as in the mid-latitude experiments. The choice of the boundary layer depth is based on radiosonde observations during the Tropical Warm Pool International Cloud Experiment (TWP-ICE), which took place in the Darwin area in 2006. As the mid-level relative humidity for most of the Darwin soundings is lower than that used in WK82, some of these cases are initialised also with the relative humidity given by Eq. (3.2). This procedure allows the sensitivity of the model results to the mid-level moisture of the sounding to be investigated.

---

[1]CAPE is calculated here assuming pseudoadiabatic processes and Bolton's formula [Eq. (43) in Bolton 1980] for the equivalent potential temperature.
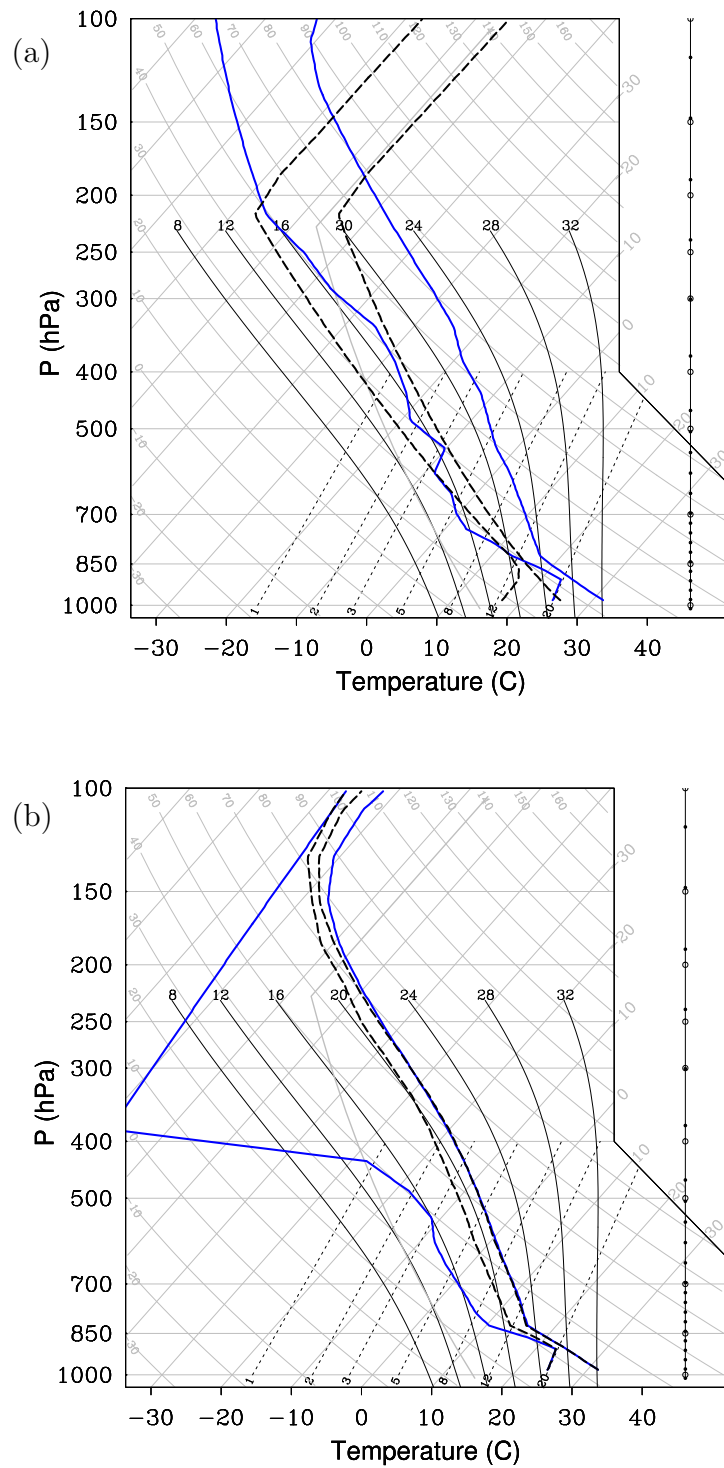
Figure 3.1: Skew$T$-log$p$ diagram showing the temperature and dew-point temperature of the (a) $q_{v0} = 14$ g kg$^{-1}$-mid-latitude (black dashed lines) and Darwin (blue solid lines) model experiments and in (b) of the Jordan (blue solid lines) and Colon (black dashed lines) model experiments. The Darwin profile plotted here is an average profile over three days (Davg, YYMMDD = 051114, 031126, 060207).
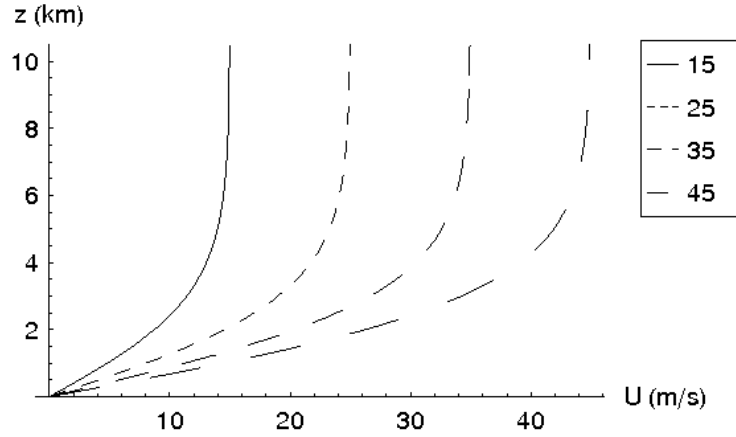
Figure 3.2:  Wind profiles as defined by Eq. (3.5) for $U_s = (15, 25, 35, 45)$ m s$^{-1}$.

To show that the tropical thunderstorm results are not specific to the Darwin thermo-dynamic profile, the tropical soundings of Colon (1953) and Jordan (1958) are considered also (see Fig. 3.1b). The latter is a mean night time sounding for the West Indies, based on the monthly aerological records from July to October for the 10-yr period 1946–1955 for Miami, Florida; San Juan, Puerto Rico and Swan Island. The Colon sounding is a Pacific mean sounding, where the night time observations from June to September at Kwajalein, Guam, and Palau for the period 1944–1947 were used. The temperature profile for the Jordan and the Colon soundings are almost identical, but the Jordan profile is considerably drier above about 850 hPa. As for the Darwin profiles, the low-levels of the Jordan and Colon profiles are modified to give a convectively well-mixed boundary layer in the lowest 1 km.

### Thermal perturbation

The numerical simulations are initialised with a horizontally homogeneous atmosphere, as described above, which contains an axially symmetric thermal perturbation ("warm bubble") with a temperature excess $\Delta\theta$ specified in the centre, decreasing to 0 K at the edge. In Clark's model the potential temperature of the perturbation is presented by

$$\theta_{wb} = \Delta\theta \sin\left[\frac{\pi}{r}\left(x - x_c + \frac{r}{2}\right)\right] \sin\left[\frac{\pi}{r}\left(y - y_c + \frac{r}{2}\right)\right] \sin\left(\frac{\pi}{r}h\right), \qquad (3.3)$$

where the horizontal and vertical radius of the warm bubble is given by $r$ and $h$, respectively, and where the bubble centre is at $(x_c, y_c)$. In Bryan's model the potential temperature of the perturbation is given by

$$\theta_{wb} = \Delta\theta \cos^2\left(\frac{1}{2}\pi\beta\right), \quad\text{with}\quad \beta = \sqrt{\left(\frac{x - x_c}{r}\right)^2 + \left(\frac{y - y_c}{r}\right)^2 + \left(\frac{z - z_c}{h}\right)^2}, \qquad (3.4)$$

which has a horizontal temperature gradient different from that described by Eq. (3.3). However, the slightly differently shaped thermals do not change the results qualitatively. As detailed in Table 3.1, different values of $\Delta\theta$, $r$, and $h$ are tested and used in the models and experiments.

**Wind profile**

The wind profile is defined as in WK82 and is given by

$$u(z) = U_s \tanh \left( \frac{z}{3000 \text{ m}} \right), \tag{3.5}$$

which represents a shear layer depth $H$ of about 6 km (see Fig. 3.2). In this study, the parameter $U_s$ is varied from 0 to 45 m s$^{-1}$ in increments of 5 or 10 m s$^{-1}$, giving a maximum shear of $7.5 \times 10^{-3}$ s$^{-1}$. A mean wind speed $u_{mean} \approx U_s/2$ is subtracted from the wind profile so that the storm remains near the centre of the domain during the simulation. As mentioned earlier, the lower boundary is defined as being free-slip, allowing the subtraction of $u_{mean}$ without influencing the boundary-layer dynamics (Note that the surface friction is not Galilean invariant).

## 3.2   Warm clouds

**Mid-latitude thunderstorm experiments – a revisit of WK82**

The simulations of mid-latitude thunderstorms performed by WK82 are rerun using Bryan's and Clark's model. This allows a comparison of the results obtained with the different models. Furthermore, it allows one to test the basic findings of WK82. In addition, definitions relating to certain storm characteristics will be introduced to be used in later sections. Therefore, the two models are initialised with a (20 km – 2.8 km – 2 K)[2] warm bubble and the Kessler-scheme, giving model conditions as in WK82 (see Table 3.1).

The amount of vertical wind shear determines whether a thunderstorm updraught splits. However, already during the developing stage of a thunderstorm, the wind profile has a large influence on the strength and shape of the convection. The effect of the vertical wind shear on the initial updraught strength is apparent from Fig. 3.3, where the maximum vertical velocity $w_{max}$ is plotted versus time. As for the thunderstorms simulated in WK82 (Fig. 3.3b), the initial updraughts in Bryan's model evolve through a cycle of growth, reaching their peak vertical velocities $w_{max}$ between 20 and 35 min after model initialisation (Fig. 3.3a). The maximum updraught strength of the initial cell decreases with increasing $U_s$ because of the increase in entrainment (WK82). In Bryan's model, the peak values of $w_{max}$ for the different shear experiments are found to be 14% larger, on average, than those in WK82, while the $w_{max}$ in Clark's model (not shown) are about 14% smaller than in WK82.

When the environmental wind shear is increased, a value $U_s$ is reached whereby the initial updraught splits. For the purpose of the following analysis, four types of thunderstorm evolution are considered: no split, incomplete split, splitting without intensification, and splitting with intensification. A "no split" situation occurs when the initial updraught decays without splitting. An "incomplete split" occurs when the storm decays just as the initial updraught begins to split and a downdraught with $w < 0$ m s$^{-1}$ fails to develop between the two updraughts. A "split without intensification" occurs when the updraught splits and the maximum updraught speed of either supercell remains smaller than the $w_{max}$ of the initial updraught. If the maximum updraught speeds of the supercells become larger than $w_{max}$ of the initial updraught, the split is defined as a "split with intensification". In

---

[2](20 km – 2.8 km – 2 K) represents a thermal perturbation with a width of 20 km, a depth of 2.8 km, and a temperature excess of 2 K. The notation (width – depth – excess) will be used throughout.
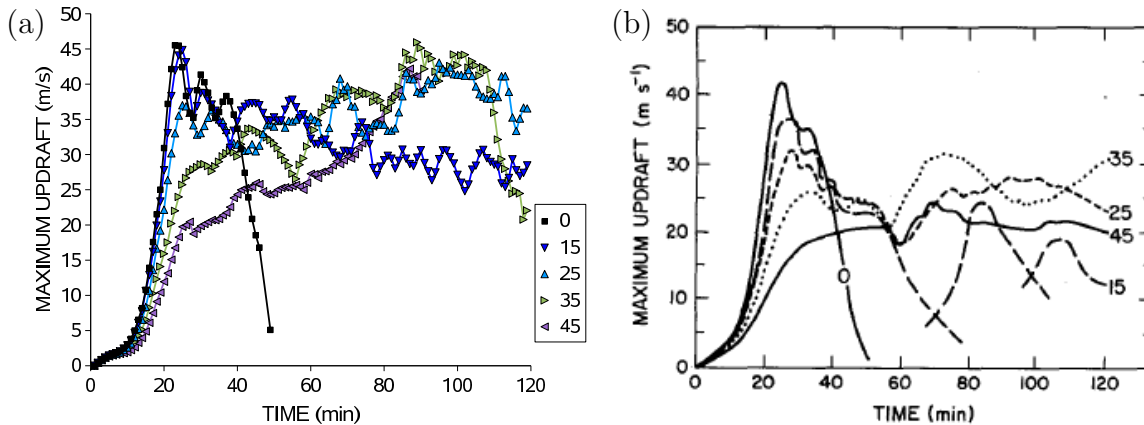
Figure 3.3:   Time series of maximum vertical velocities $w$ in the $q_{v0} = 14$ g kg$^{-1}$ experiments with $U_s = 0, 15, 25, 35, 45$ m s$^{-1}$ (a) using Bryan's model and (b) in WK82 (their Fig. 3).

WK82, complete splitting occurs for $U_s \gtrsim 20$ m s$^{-1}$ (see Fig. 1.7b). However, Bryan's and Clark's model show that complete splitting is observed already for $U_s \gtrsim 10$ m s$^{-1}$. More precisely, from Fig. 3.3a it can be seen that splitting with intensification occurs in Bryan's model if $U_s$ is equal or larger 25 m s$^{-1}$, while in WK82, $U_s \gtrsim 30$ m s$^{-1}$ is necessary to get intensifying right- and left-movers (compare the $w_{max}$ in Fig. 1.7a and 1.7b of the $q_{v0} = 14$ g kg$^{-1}$ experiment).

Explaining the reason for the slightly different peak updraught velocities and splitting behaviours in the three models is not the focus of this study, although differences in the horizontal and vertical resolution and in the parameterisations of the microphysics scheme can contribute to these differences (see section 3.4). It is important here to show that all three models produce similar results concerning the overall thunderstorm evolution including: the cycle of updraught growth; the mature stage with comparable peak updraught velocities reached at about the same time; the cycle of decline and the subsequent splitting with or without intensification when $U_s$ is sufficiently large.

### 3.2.1   Mid-latitude and tropical thunderstorms

In the course of this work it was found that the (20 km – 2.8 km – 2 K) thermal perturbation used in the previous section is not optimal to simulate mid-latitude and tropical thunderstorms with Bryan's and Clark's model (see section 3.4). The results in the following sections are obtained by simulations conducted with both cloud models using the Kessler scheme and a smaller in extent, but stronger (8 km – 1 km – 8 K) thermal perturbation. In reality such a large temperature excess within the boundary layer would not be observed. However, because surface heating is not included here, convective motions within the mixed layer are not represented. Therefore, the updraughts that develop in the boundary layer and initiate deep convection are also not represented. By trial and error, the value of 8 K was chosen so that storms are consistently produced in both models. The depth of the perturbation is set to 1 km so that the thermal lies completely within the well-mixed layer.

Thunderstorms are simulated in three mid-latitude environments and eight tropical environments (see Table 3.2). The shear magnitude $U_s$ is varied in each of these environments

| Sounding | CAPE | CAPE$_{8km}$ | Clark $w_{max}$ ($\alpha$) | Bkess $w_{max}$ ($\alpha$) | Bice $w_{max}$ ($\alpha$) |
|---|---|---|---|---|---|
| Mid-latitude $q_{v0} = 12$ g kg$^{-1}$ (mid12) | 840 | 646 | 25.7 (63) | 30.3 (74) | 32.8 (80) |
| Mid-latitude $q_{v0} = 14$ g kg$^{-1}$ (mid14) | 1893 | 843 | 39.4 (64) | 42.8 (70) | 48.8 (79) |
| Mid-latitude $q_{v0} = 16$ g kg$^{-1}$ (mid16) | 2917 | 1823 | 48.8 (64) | 54.4 (71) | 58.2 (76) |
| Darwin average-profile (Davg) | 5079 | 1857 | 41.6 (41) | 48.3 (48) | 55.7 (55) |
| Darwin average-profile WK (DavgWK) | 4890 | 1743 | 46.2 (47) | 54.4 (55) | 63.8 (65) |
| Darwin 051114 (D051114) | 5532 | 1990 | 45.4 (43) | 48.0 (46) | 56.7 (54) |
| Darwin 041217 (D041217) | 6084 | 2108 | 46.7 (42) | 51.3 (47) | 61.0 (55) |
| Darwin 011120 (D011120) | 3911 | 1405 | 35.7 (40) | 49.2 (56) | 58.7 (66) |
| Darwin 011120 WK (D011120WK) | 3787 | 1286 | 38.9 (45) | 47.2 (54) | 53.8 (62) |
| Colon | 5925 | 2085 | 52.1 (48) | 63.8 (59) | 71.8 (66) |
| Jordan | 5742 | 2141 | 49.2 (46) | 60.2 (56) | 68.7 (64) |

Table 3.2: Values of total CAPE and CAPE$_{8km}$ (in J kg$^{-1}$), and maximum updraught speed $w_{max}$ (in m s$^{-1}$) for the different models initialised with $U_s = 0$ m s$^{-1}$. The overturning efficiency $\alpha$ (in %) is given in brackets. "Bkess" and "Bice" stand for Bryan's model using the Kessler scheme and ice microphysics, respectively. The abbreviations of the model names are provided in parentheses; "WK" indicates that the model is initialised with the relative humidity profile of WK82 [Eq. (3.2)].

and in total up to 85 storm cases are examined with both Bryan's and Clark's model. In the following analysis, a thunderstorm that is simulated using a Darwin thermodynamic profile will be referred to as a "Darwin storm", while thunderstorms simulated in the other environments will be referred to as a "Colon storm", "Jordan storm", and a "mid-latitude storm" according to the sounding used. Unless otherwise noted, plots will be shown only for the results obtained with Bryan's model, as those from Clark's model are similar.

**Single cells**

The model-generated single cell storms in a mid-latitude (mid14) and a tropical (Davg) environment in the absence of an environmental flow are shown in Fig. 3.4. The storm top, which is defined as the height at which the sum of the cloud and rain water mixing ratio becomes smaller than 0.1 g kg$^{-1}$, lies at $z \approx 14.5$ km for the mid-latitude and $z \approx 17.5$ km for the tropical storm. The tropical storm has a deeper and stronger updraught than the mid-latitude storm due to the higher tropopause and larger CAPE (see Table 3.2).

**Split cells**

The time at which splitting occurs is defined as the time when, at a height level of 4.6 km, the innermost vertical velocity contour (1 m s$^{-1}$ interval) splits into two parts. The 4.6 km height level was chosen by WK82 as a representative height for mid-levels and is retained here, although it is possible that for the deeper tropical storms, a larger height might be more appropriate.

Whether the splitting is incomplete, or complete with or without intensification depends on the amount of environmental wind shear. The simulations show that with increasing $U_s$, the stages of splitting behaviour of the initial updraught are: no split $\rightarrow$ incomplete split $\rightarrow$
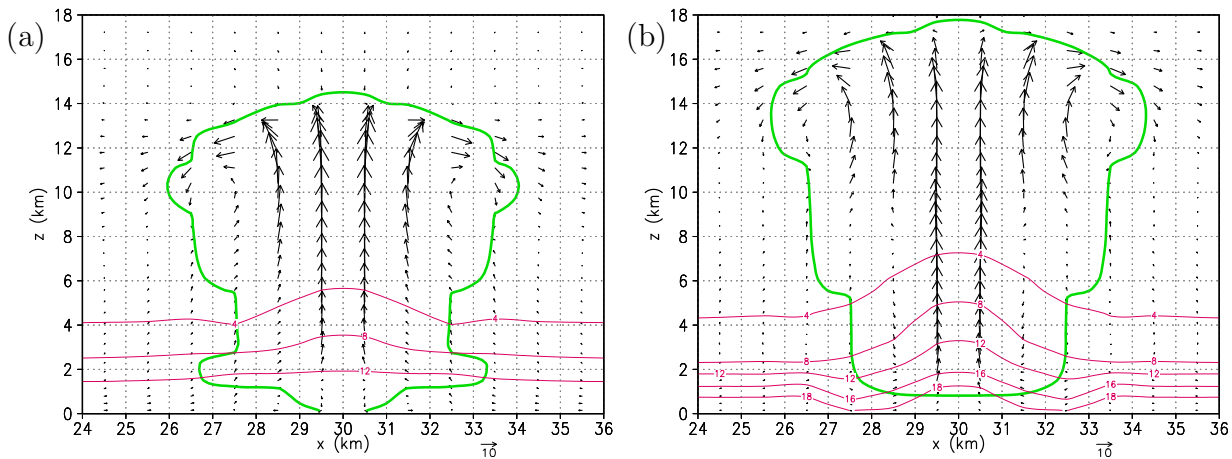
Figure 3.4:   Vertical cross-sections of a (a) mid14-storm and (b) Davg-storm initialised in environments without vertical wind shear. The cross-sections are taken at $t = 18$ min, when the cloud-top height is greatest.  Vectors represent velocity, the thick green line is the 0.1 g kg$^{-1}$ contour of $q_r + q_c$, and the water vapour mixing ratio $q_v$ is represented by the thin red lines contoured at 4, 8, 12, 16, and 18 g kg$^{-1}$.

splitting without intensification $\rightarrow$ splitting with intensification. Not every thunderstorm case exhibits all of these stages, since $U_s$ is increased in increments of 5 or 10 m s$^{-1}$ and not continuously.

   One example of storm splitting with intensification in a tropical environment is depicted in Fig. 3.5.  In this case the shear vector points towards the east.  Figure 3.5 shows horizontal cross-sections through the initial updraught (12, 33, 44 min) and through the right-moving storm (52, 66, 100 min), respectively.  Convection is initialised by a thermal perturbation at $t = 0$ min.  Twelve minutes after model initialisation, the updraught continues to grow and subsiding motion (magenta contours) is positioned to the east due to the downshear tilting of the cell.  Since the up- and downdraught are separated, the updraught is not destroyed by the subsidence.  The initial updraught reaches its peak vertical velocity ($w_{max} = 19.4$ m s$^{-1}$) at 18 min and then starts to decline.  Three minutes later, rain ($q_r > 0.1$ g kg$^{-1}$) reaches the ground and a pool of cold air develops and begins to spread out.  After 33 min, the gust front (thick black line) lies about 4 km away from the centre of the initial cell and lifts warm and moist air into the updraught.  Storm splitting occurs after 43 minutes.  As the $w$-contour interval is only 5 m s$^{-1}$, the splitting is not apparent in Fig. 3.5 (44 min).  However, the "C-shape" of the $w$-contours[3] is a typical feature which appears shortly before splitting occurs in the models.  Two equal and self-sustaining rotating cells are formed and propagate continuously to the right and left of the mean shear vector. I refer to these as supercells. Note that in Figs. 3.5, only the supercell moving to the right, or "right-mover", is shown. The cyclonic rotation of the updraught is apparent from the velocity vectors depicted at mid-levels.  Comparing the position of

---

[3]As Fig. 3.5 (44 min) shows only the southern half of the domain, the "C-shape" in the $w$-contours of the initial updraught becomes apparent only when the panel is mirrored at $y = 30$ km, thus adding the northern half of the domain.
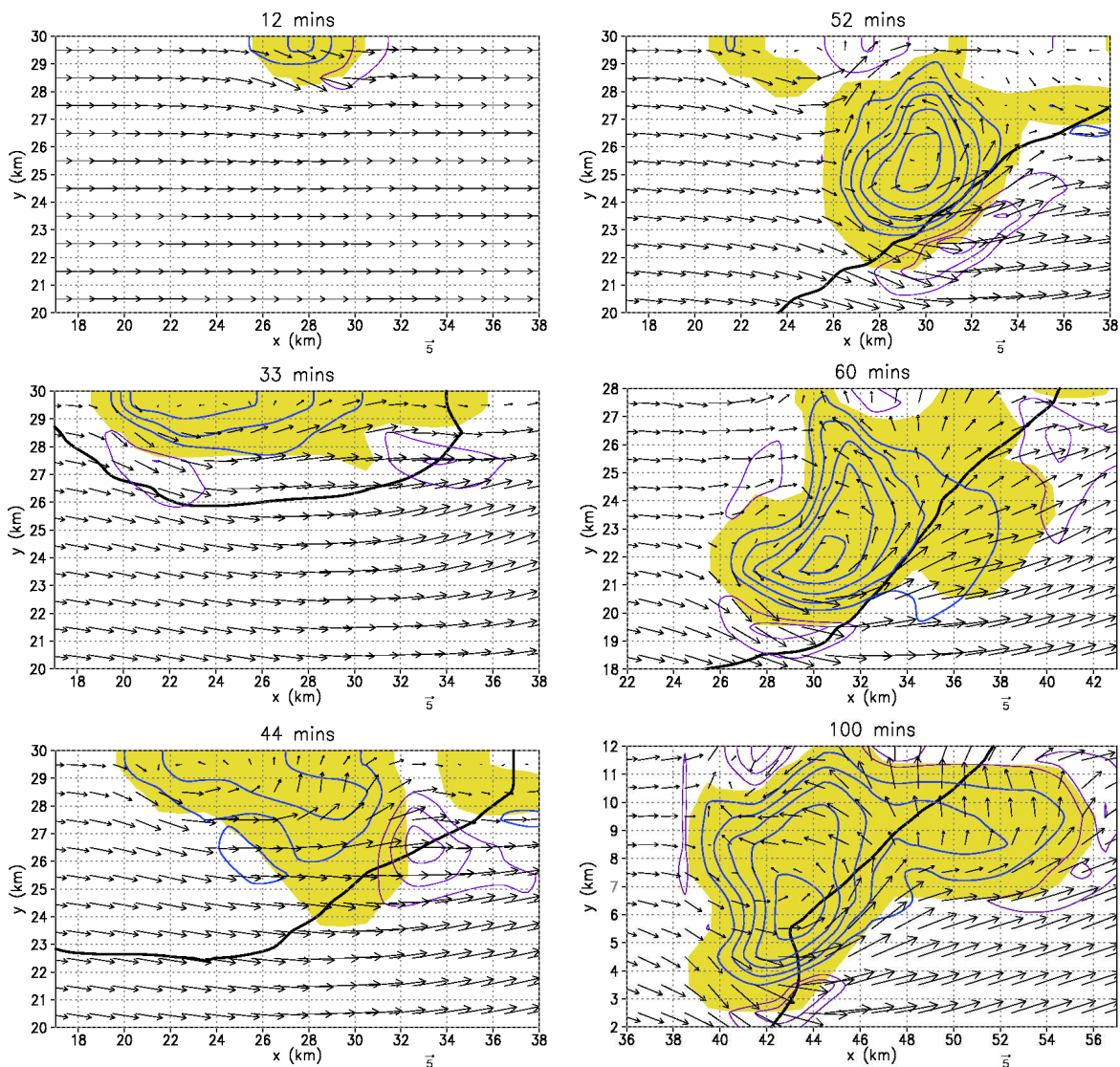
Figure 3.5:   Horizontal cross-section through a Darwin storm in an environment (Davg) with $U_s = 40$ m s$^{-1}$, (12, 33, 44, 52, 60, and 100) min after model initialisation. At mid-levels ($z = 4.6$ km), positive (negative) vertical velocity is contoured in blue (magenta) every 5 m s$^{-1}$ (3 m s$^{-1}$), and the yellow shading represents the region where the cloud water mixing ratio $\geq 0.1$ g kg$^{-1}$. The surface gust front is denoted by the thick black line and represents the $-0.5$ K temperature perturbation contour. Vectors represent storm relative mid-level horizontal winds. A mean wind speed of 20 m s$^{-1}$ is subtracted from the initial wind field. Only parts of the southern half of the domain are shown, while the northern half of the domain is a mirror-image of it (mirrored at $y = 30$ km).
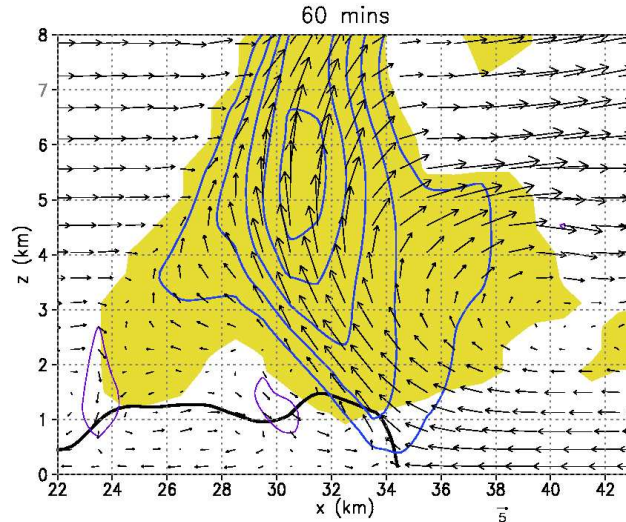
Figure 3.6: Vertical cross-section through the right-mover depicted in Fig. 3.5, at $y = 22$ km, 60 min after model initialisation. Positive (negative) vertical velocity is contoured in blue (magenta) every 5 m s$^{-1}$ (3 m s$^{-1}$) and the yellow shading represents the region where the cloud water mixing ratio $\geq 0.1$ g kg$^{-1}$. The gust front is denoted by the thick black line and represents the $-0.5$ K temperature perturbation contour. Vectors represent storm relative winds.

the right-mover relative to the gust front after 52 min, 60 min, and 100 min, one can see that the cold pool edge propagates at about the same speed as the supercell. Thus, the gust front lifts warm environmental air into the updraught enabling the storm to intensify further. This warm inflow into the storm is apparent from Fig. 3.6, which shows a vertical cross-section through the supercell and the eastward propagating gust front (thick black contour) at 60 min. While the initial updraught has a $w_{max}$ of only 19.4 m s$^{-1}$, the supercell reaches up to 37 m s$^{-1}$ and thus, this case is classified as "splitting with intensification".

Of the 85 experiments examined with Bryan's model, 63.53% of the thunderstorms are classified as non-splitting, 3.53% as incomplete splitting, 12.94% as splitting without intensification, and 20.0% as splitting with intensification. The corresponding distribution for Clark's model is: 45.88% non-splitting; 8.24% incomplete splitting; 15.29% splitting without intensification; and 30.59% splitting with intensification. An explanation for the different percentages between the models is presented later.

One of the major topics in this study is to investigate under which conditions a thunderstorm becomes severe, *i.e.*, when storm splitting occurs, leading to the formation of supercells. If the splitting behaviour of the tropical thunderstorms is compared with that of the mid-latitude thunderstorms, one distinctive feature is apparent: Complete splitting (with or without intensification) is found in the mid-latitudes for $U_s \gtrsim 10$ m s$^{-1}$, whereas $U_s \gtrsim 30$ m s$^{-1}$ is required for complete splitting in the tropics (see Fig. 3.8). The simulations conducted with Clark's model show that complete splits occur for the mid-latitude thunderstorms if $U_s \gtrsim 15$ m s$^{-1}$, whereas $U_s \gtrsim 30$ m s$^{-1}$ is required for the tropical thunderstorms. Thus, both models show that a larger wind shear is necessary for a storm to split in a tropical environment than in a mid-latitude environment.
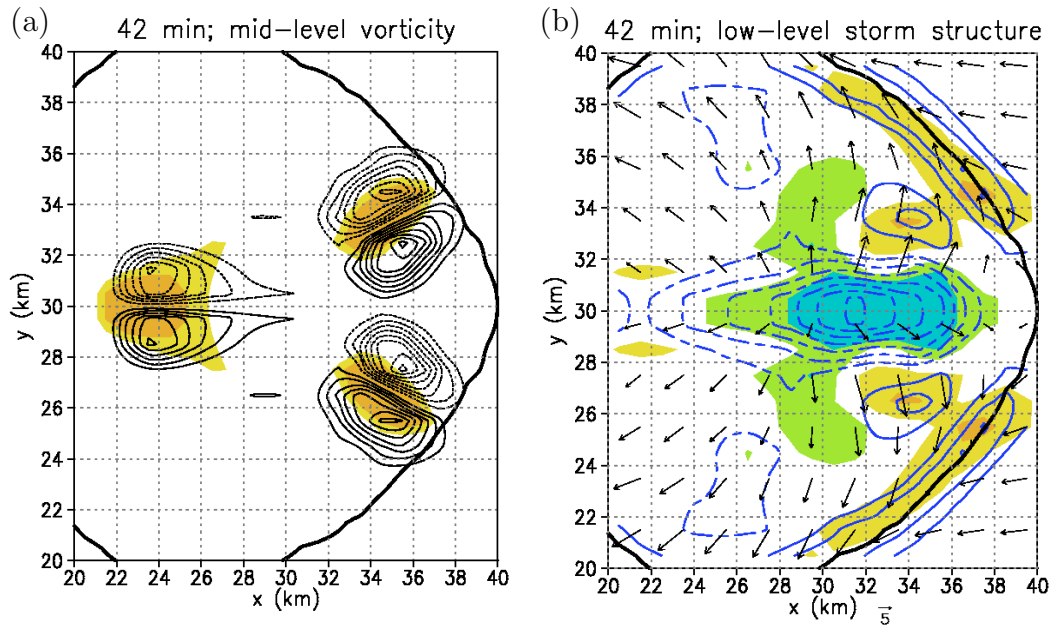
Figure 3.7:  Mid-level and low-level storm structure at $t = 42$ min for the tropical case D041217, initialised with $U_s = 30$ m s$^{-1}$. The surface gust front is denoted by the thick black line and represents the $-0.5$ K temperature perturbation contour.  (a) Regions of updraught velocities at $z = 4.6$ km larger than 5 m s$^{-1}$ and 10 m s$^{-1}$ are shaded in yellow and orange, respectively. Vertical vorticity $\zeta$ at $z = 4.6$ km is contoured every $2 \times 10^{-3}$ s$^{-1}$ with positive values depicted by the solid lines and negative values represented by the dotted lines, omitting the zero contour. (b) Vectors represent the horizontal flow at the surface and the surface divergence and convergence are contoured (dashed/solid) in blue at $2 \times 10^{-1}$ s$^{-1}$ intervals with the zero contour omitted. Regions of updraught velocities at cloud base ($z = 1.1$ km) larger than 2 m s$^{-1}$ and 5 m s$^{-1}$ are shaded in yellow and orange, while regions of downdraught $< -2$ m s$^{-1}$ and $< -5$ m s$^{-1}$ are shaded in green and light blue, respectively.

### Secondary cells

A phenomenon which occurs in some simulations, both in the mid-latitudes and in the tropics is the development of two new secondary cells on the gust front. An example is shown in Figs. 3.7a and 3.7b, where the mid- and low-level storm structure at 42 min after model initialisation are shown, respectively. The initial updraught with the vortex couplet is apparent at $(x, y)$=(24 km, 30 km) in Fig. 3.7a. The downdraught formed east of the updraught (green and blue shading in Fig. 3.7b), feeding the cold pool which spreads out along the surface in all directions. Ahead of the cold pool, the low-level horizontal convergence (blue solid lines in Fig. 3.7b) is large because the warm environmental inflow opposes the cold air. This convergence creates ascent on the northeastern and southeastern edges of the gust front. Thus, two new cells are triggered about 10 km ENE and ESE of the initial updraught. This case is classified as a "no split" case, because the innermost vertical velocity contour (1 m s$^{-1}$ interval) of the initial updraught never splits into two. Moreover, the new secondary cells contain a vortex couplet and are therefore not supercells (see section 3.2.4, Figs. 3.14a and b).

Whether these secondary cells are physically realistic or just a numerical byproduct is

unclear. Secondary cells, such as those modelled in WK82 using $U_s = 15$ m $^{-1}$, are not found in Clark's or in Bryan's model for any amount of wind shear and temperature and moisture profile. The occurrence of these secondary cells seems to be a general problem of such modelling studies (G. Bryan, personal communication). As the tropical environments contain large instability, deep convection can be triggered often somewhere in the domain, perhaps due to gravity waves excited by the initial updraught. However, focussing on the initial updraught and concentrating on the question whether splitting and thus, supercells occur using the definition of splitting given above, achieves the main goal of this study.

## 3.2.2   CAPE and updraught strength

In previous studies (WK82; Weisman and Klemp 1984, hereafter WK84), the dependence of the modelled thunderstorm structure on environmental buoyancy and wind shear was generalised in terms of the Richardson number

$$R = \frac{CAPE}{\frac{1}{2}\bar{u}^2}. \tag{3.6}$$

Table 3.2 shows the magnitudes of total CAPE as defined in section 1.2, for all the mid-latitude and tropical cases studied. The variation of $\sqrt{CAPE}$ with $U_s$ for the thunderstorm cases that use Bryan's model is shown in Fig. 3.8a. The two straight lines represent the thresholds of the Richardson number for which supercells can be expected (WK82). The light blue line on the right indicates the lower boundary of the supercell range ($R = 10$), while the dark blue line on the left indicates the upper boundary where $R = 50$. Black squares (green dots) represent the mid-latitude (tropical) cases where no splitting, or where an incomplete split occurs. Black hourglasses represent the mid-latitude cases and green stars tropical cases where complete splitting with or without intensification occurs. Thus, in Fig. 3.8a, the split cases should lie in between the two blue lines. However, of the 21 simulated mid-latitude cases, only 48% are successfully predicted[4] as being either a split or no-split, and of the 64 simulated tropical cases 67% are successfully predicted. With Clark's model, 62% of the mid-latitude storms are successfully predicted, while 89% of the tropical storms are successfully predicted. Even though the Richardson number criterion seems to be suitable for the prediction of modelled tropical and mid-latitude storms, these foregoing percentages may be fortuitous as explained below.

### Deficiencies of CAPE and $R$

On first inspection of Eq. (3.6), it may be expected that the large CAPE in the tropical environments would automatically mean that a larger wind shear is required to produce storm splitting compared to mid-latitude environments. However, when Fig. 3.8a is re-plotted with the maximum updraught speed $w_{max}$ from the model as the ordinate (Fig. 3.8c), the values of $w_{max}$ for thunderstorms in both environments are comparable. In fact, for a given wind shear and relative humidity profile, there are cases where the mid-latitude CAPE (2917 J kg$^{-1}$) is smaller than the Darwin CAPE (4890 J kg$^{-1}$), but the updraught of the mid-latitude storm (39 m s$^{-1}$) is stronger than that of the Darwin storm (32 m s$^{-1}$). These lower values of $w_{max}$ of the tropical storm, despite occurring in environments of

---

[4] "Successfully predicted" means that the value of $R$ for the split cases lies within the plotted thresholds for split storms in Fig. 3.8a and outside for the cases which do not split.
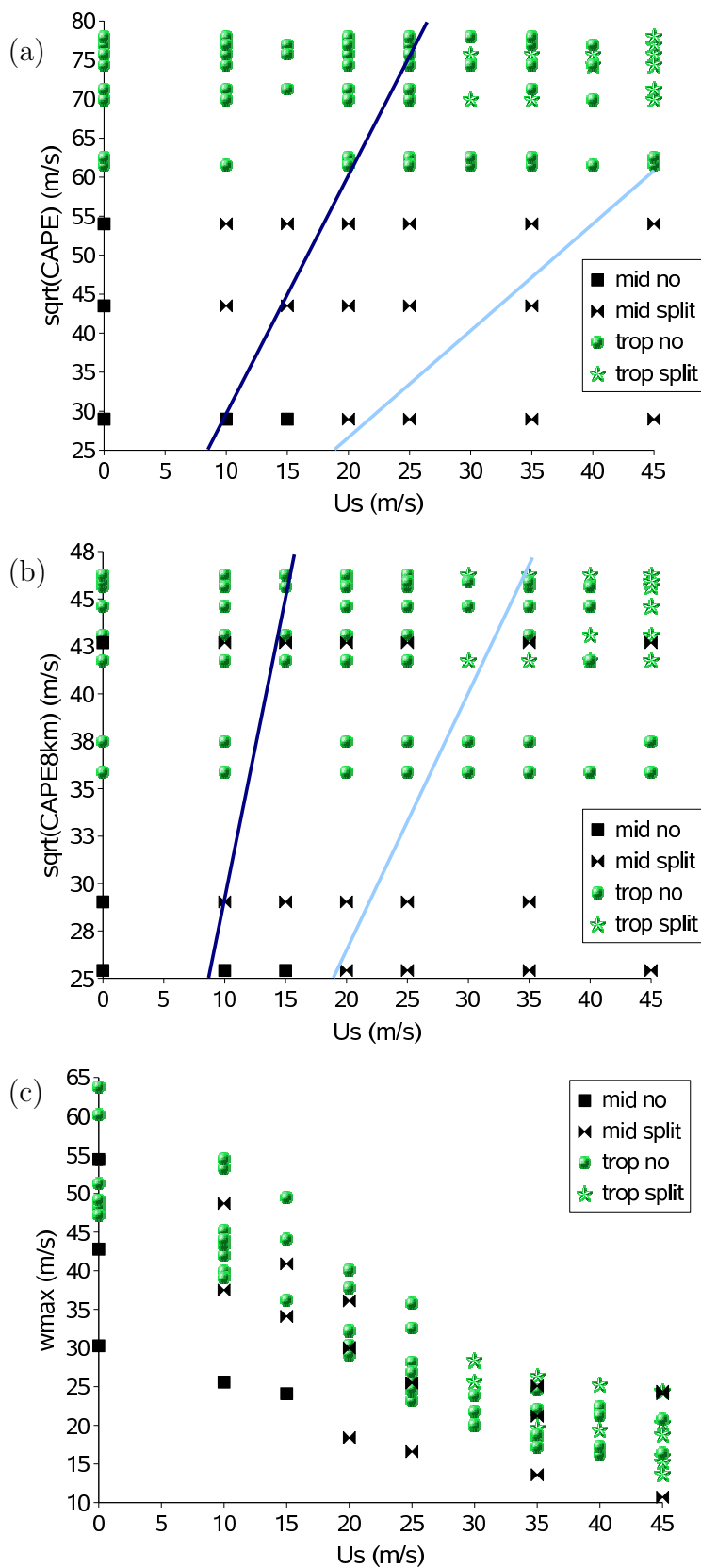
Figure 3.8: Plotted are (a) $\sqrt{CAPE}$, (b) $\sqrt{CAPE_{8km}}$, and (c) $w_{max}$ vs $U_s$. Black squares (green dots) represent the mid-latitude (tropical) cases where no splitting or an incomplete split occurs. Black hourglasses (green stars) represent the mid-latitude (tropical) cases where complete splitting with or without intensification occurs.

larger CAPE than that in mid-latitudes, highlights the known deficiencies of CAPE, in that it does not consider entrainment, precipitation loading, water vapour deficit, and vertical pressure gradient forcing (*e.g.*, Gilmore and Wicker 1998). Thus uncertainties exist in using the Richardson number as a criterion to define the regime where supercells are expected. The Richardson number $R$ predicts that large shear is required for thunderstorms to split in tropical environments which have large CAPE, as is found here. However it seems that a physical interpretation in terms of $w_{max}$, which is in some cases lower for the tropical cases compared to the mid-latitude cases, suggests that a lower shear would be required to split the tropical thunderstorms. Furthermore, Kennan and Carbone (1992) point out, that the computation of CAPE is very sensitive to the virtual temperature and the initial surface conditions: "A 1 g kg$^{-1}$ increase in mixing ratio or an increase in temperature of 1°C can increase CAPE by 500 J kg$^{-1}$". This means that if the surface temperature and moisture can not be assessed correctly for the time when thunderstorms are expected to occur, the calculated values of CAPE and $R$ can be significantly different to reality and thus, mislead the forecaster.

### Shape of buoyancy profile

Previous studies, *e.g.*, McCaul and Weisman (2001), have shown that the *shape* of the buoyancy profile influences the characteristics of deep convection. Typically, a mid-latitude sounding with large CAPE has large buoyancy at low-levels, where most of the wind shear is located. In contrast, a tropical sounding with large CAPE has a narrow buoyancy profile extending relatively evenly over a large depth. So, although a mid-latitude and a tropical sounding may have the same CAPE, the CAPE calculated from $z = 0$ to say 8 km (CAPE$_{8km}$) would be larger for the mid-latitude case than for the tropical case. However, McCaul and Weisman (2001) showed also that even though the effect of the buoyancy profile shape on convection is large for small CAPE (800 J kg$^{-1}$), it decreases as CAPE increases (2000 J kg$^{-1}$) and "must become unimportant in environments featuring extremely large values of CAPE."

To examine whether the CAPE calculated from the surface to a height of 8 km is a better energetic measure of the viability of convection, CAPE$_{8km}$ is determined for every model and presented in Table 3.2. Figure 3.8b is similar to Fig. 3.8a, but shows $\sqrt{CAPE_{8km}}$ versus $U_s$. Note that the ordinate in Fig. 3.8b has been rescaled as CAPE$_{8km}$ < CAPE. For the tropical environments, the values of $\sqrt{CAPE_{8km}}$ and $R_{8km}$ are now comparable to those of mid16. To give a specific example, the Richardson number $R_{8km}$ calculated using CAPE$_{8km}$ and $U_s = 25$ m s$^{-1}$ for the Davg and the mid16 case is nearly identical at 16. However, the mid16-storm splits, while the tropical storm does not, showing that the Richardson number so defined cannot be used to distinguish the different thunderstorm behaviour in these cases. CAPE calculated over other height levels (CAPE$_{nkm}$, with $n = 6$ and 7 km) and the respective Richardson numbers do not improve the statistics either. $R$ successfully predicts 62% of the cases in Bryan's model, but only 34% of the cases are predicted successfully when $R_{8km}$ is used. These statistics are based on the assumption that the thresholds of the Richardson number $10 < R < 50$ given in WK82 are valid also for R$_{8km}$. It can be expected that the thresholds of the Richardson number would change when CAPE$_{nkm}$ is used for calculating the Richardson number $R_{nkm}$. However, as $R_{8km}$ is less suitable for predicting supercells than $R$, no further research was undertaken to determine how the thresholds of $R$ change if CAPE is calculated over a height of $z = 0$ to

$n$ km. Section 3.5 will introduce a new diagnostic variable to aid in the forecast of split storms.

**Overturning efficiency**

Table 3.2 provides a summary of the maximum updraught speed $w_{max}$ and the overturning efficiency of the modelled storms initialised in an environment without vertical wind shear. The overturning efficiency, $\alpha$, is a measure for the ability of the thunderstorm to convert CAPE into updraught kinetic energy and is given by

$$\alpha = \frac{w_{max}}{\sqrt{2 \times CAPE}}. \tag{3.7}$$

Note that in WK82, $\alpha$ is called the "storm strength $S$". As can be seen in Fig. 3.8c, for a given CAPE, both $w_{max}$ within the modelled storms and thus, $\alpha$ decrease with increasing wind shear. Such a decrease in storm intensity has been reported also in numerical simulations by WK82 and has been shown to be due to entrainment into the storm reducing the positive buoyancy of the updraught, which increases as the shear increases. From Table 3.2 it is apparent that $\alpha$ is significantly larger for the mid-latitude cases than for the tropical cases. The values of $\alpha$ are comparable to those reported in McCaul and Weisman (1996), where $\alpha \approx 70\%$ for the mid-latitude thunderstorm and $\alpha \approx 40\%$ for the supercells simulated in a tropical cyclone environment. The environmental conditions, and thus the characteristics of the resulting supercells in McCaul and Weisman (1996), are different to those in this study. McCaul and Weisman explained the difference in $\alpha$ between mid-latitude and tropical cyclone storms to be due to the larger pressure forcing in the tropical cyclone supercells, which boosts updraught strength at low levels, but quickly destroys it at higher altitudes. Furthermore, they note that the small diameters of updraughts in tropical cyclone make them more prone to turbulent mixing, which leads to smaller overturning efficiencies. In the present work, the width of the updraught of a mid-latitude and a tropical thunderstorm are comparable (see Fig. 3.4), but the deeper tropical storms are more exposed to mixing than the smaller mid-latitude updraughts. Another reason for the different values of $\alpha_{mid}$ and $\alpha_{trop}$, together with the reason for the different splitting behaviour in the mid-latitudes and tropics, is discussed below.

### 3.2.3 Downdraught and gust front

To investigate why a larger vertical wind shear is required for tropical thunderstorms to split compared with mid-latitude thunderstorms, the effect of the vertical wind shear on the downdraught and subsequent cold pool of the storm will be examined.

**Previous work**

As described in section 1.3, previous research on mid-latitude thunderstorms has shown that the gust front is important for the evolution of the storm. If the cold-air outflow produces a gust front which moves too fast relative to the translation speed of the updraught, the supply of warm air to the updraught and its flanks will be cut off by the spreading cold pool.

The influence of the shape of the buoyancy profile on the updraught and subsequent downdraught has been investigated extensively in the COMPASS project (*e.g.*, McCaul
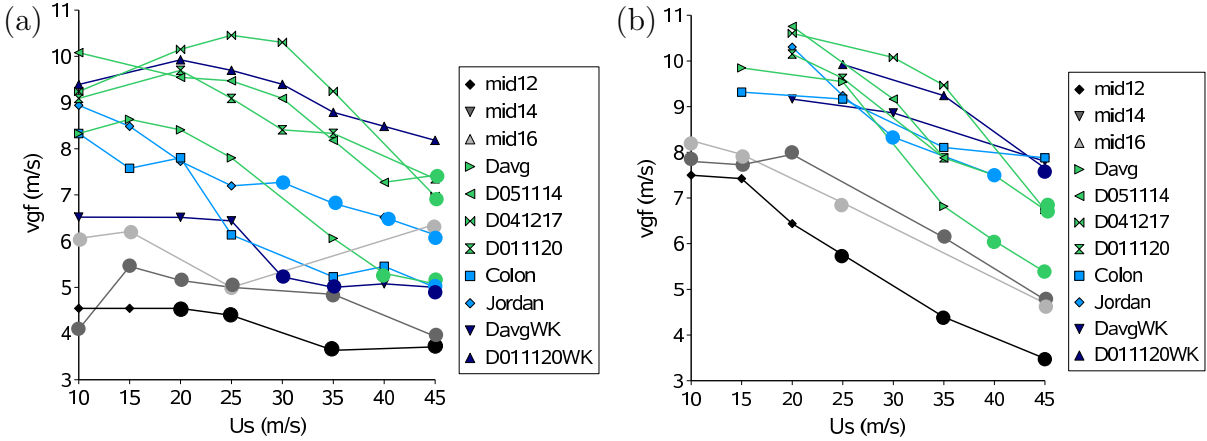
Figure 3.9: Speed of the gust front $v_{gf}$ (in north-south direction) versus $U_s$, for all mid-latitude and tropical cases simulated with the microphysics of (a) warm clouds (Bkess) and (b) cold clouds (Bice). The large circles represent the cases where complete splitting occurs.

and Weisman 2001, McCaul *et al.* 2005). McCaul and Weisman (2001) define an altitude of maximum parcel buoyancy, $z_b$, and show that as $z_b$ decreases, $w_{max}$ increases along with the temperature deficit of the subsequent cold pool. This response was observed to be strong for cases where the total CAPE is relatively small (800 J kg$^{-1}$) and decreases as the CAPE increases to and above 2000 J kg$^{-1}$. Since all but two of the cases examined here have CAPE values exceeding 2000 J kg$^{-1}$ (Table 3.2), this effect is expected to be small.

McCaul *et al.* (2005) investigated further how variations of the temperature at the lifted condensation level, which is a good proxy for the environmental precipitable water, affects the storm structure. They found that for a warmer and moister sounding, more condensation was produced in the updraughts due to the higher available water vapour mixing ratio in the subcloud layer, $q_{v0}$, which led to a larger fallout of precipitation. The downdraught of this storm was found to be stronger and the outflow colder than that of a storm produced in a cooler, drier environment. It will be shown later (see Fig. 3.11a, large symbols) that tropical storms growing in environments with the same mid-tropospheric relative humidity as the mid-latitude storms, but where CAPE, $q_{v0}$, and $z_b$ are larger, have higher amounts of water loading and comparable or stronger downdraughts than the mid-latitude storms.

I investigate now the characteristics of the downdraught and subsequent cold pool of the initial cell for all modelled cases (see Table 3.2). Even though several of the key parameters addressed by McCaul *et al.* (2005), such as $z_b$, $q_{v0}$, CAPE, and the relative humidity, vary from case to case, it will be shown that general statements can be made for the mid-latitude and tropical thunderstorms regarding the speed or timing of the gust front.

## Gust front characteristics

Twelve minutes after the gust front appears, the gust front speed, $v_{gf}$, is measured perpendicular to the shear vector. The speed perpendicular to the shear vector, *i.e.* in north-south direction, is chosen here since the strongest low-level convergence occurs along the north-
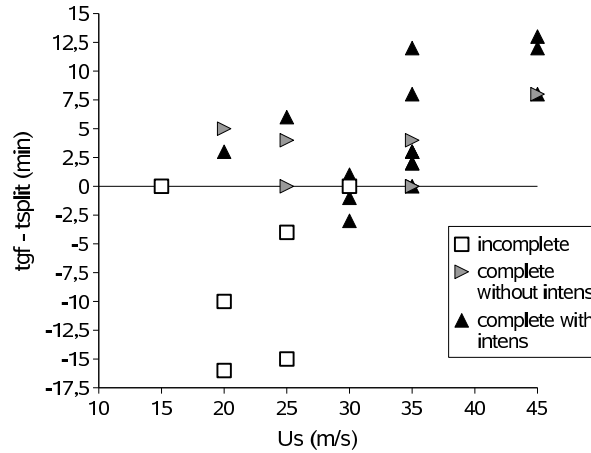
Figure 3.10:   Difference between the time of gust front appearance, $t_{gf}$, and the time of split-ting, $t_{split}$, (in min) versus $U_s$ for all mid-latitude and tropical split-cases simulated with Clark's model. White squares represent the incomplete splits, grey triangles the complete splits without intensification, while black triangles represent splitting with intensification.

ern and southern flanks of the initial updraught (not shown), and because then $v_{gf}$ is not affected directly by the environmental wind. The indirect influence of the wind shear on the gust front speed is shown in Fig. 3.9a for simulations performed with warm clouds (Bkess). From Fig. 3.9a, three characteristic features are apparent. First, for a particular environment, the speed of the gust front of the initial cell, $v_{gf}$, decreases as the shear, $U_s$, increases. Second, the modelled mid-latitude thunderstorms have slower gust fronts than the tropical thunderstorms. Third, the split cases (large dots in Fig. 3.9a) coincide with small gust front speeds of less than about 7.5 m s$^{-1}$.

In Bryan's and Clark's models the time of gust front occurrence relative to the time of maximum updraught strength is almost independent ($\pm 4$ min) of the wind shear for a particular model environment. This means that the time that the initial updraught has to develop before being cut off by its cold pool is governed mainly by how fast the gust front expands outwards. Since the speed of the gust front decreases with increasing $U_s$ (Fig. 3.9a), a thunderstorm in a highly sheared environment will have more time to evolve and possibly split before it becomes cut off from the warm inflow by the gust front. The tropical thunderstorms examined here exhibit a faster gust front than the mid-latitude thunderstorms. Thus, a greater wind shear is required in the tropics to reduce the gust front speed sufficiently so that the updraught has enough time to evolve and to split.

While the thunderstorms simulated with Bryan's model showed a clear correlation between the gust front speed and the wind shear, those in Clark's model did not. To clarify the role that the cold pool plays in determining whether splitting occurs in Clark's model, only the split storms are examined now. The time of gust front occurrence is calculated now relative to the time at which splitting occurs and depicted in Fig. 3.10 as a function of shear. Incomplete split cases coincide with relatively low shears; they occur when the gust front appears before splitting starts ($t_{gf} - t_{split} < 0$). Complete split cases coincide with relatively high shears and occur primarily when the gust front appears, either at the time of splitting, or after splitting has commenced ($t_{gf} - t_{split} \geq 0$). This means, the later the gust front appears, the more time the updraught has to split and to develop.
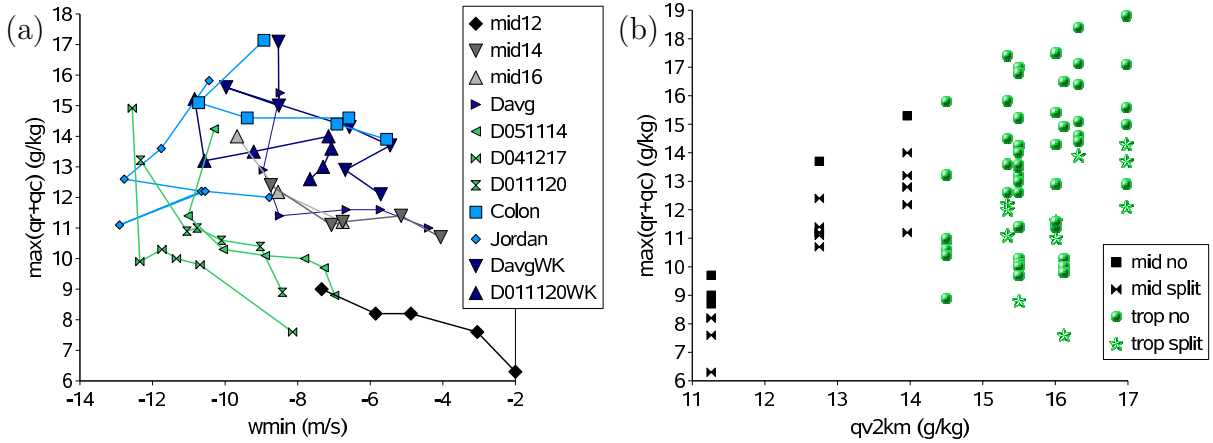
Figure 3.11:   Maximum of total liquid water versus (a) peak minimum downdraught speed $w_{min}$ measured at cloud base ($z = 1.1$ km), and (b) water vapour mixing ratio averaged over the lowermost 2 km. For each case, $U_s$ is varied giving different points in the $\max(q_r + q_c)$-$w_{min}$ phase space and $\max(q_r + q_c)$-$q_v$ phase space, respectively. The cases with an average relative humidity taken between $z = 2.6$ km and 6.9 km larger than 70% (Colon, mid12, mid14, mid16, DavgWK, D011120WK) are marked with large symbols in panel (a).

In summary, the different splitting behaviour of the initial updraught in Bryan's and Clark's model can be explained by the differences in the time of development and speed of the gust front. The gust front and downdraught characteristics depend, *inter alia*, on the microphysics scheme implemented in the model (*e.g.*, Gilmore *et al.* 2004, hereafter GSR04). However, it is not the focus of this work to determine exactly the differences between these two idealised models, since both models produce the consistent results that a higher shear is needed for tropical storms to split compared with that for mid-latitude storms and that the gust front speed is slower, or occurs later, for the mid-latitude than for the tropical cases.

**Water loading and evaporative cooling**

Two factors which determine the strength of the downdraught and thus, the gust front properties are investigated: the water loading and the evaporative cooling. In this study, the sum of the mixing ratios of cloud, $q_c$, and rain water, $q_r$, is used as a measure for the liquid water loading. Figure 3.11a shows the correlation between the maximum of the liquid water content $\max(q_r + q_c)$ and the downdraught strength, $w_{min}$, measured at cloud base. The results for a storm in a particular environment where $U_s$ is varied are connected by straight lines and environments with a mid-tropospheric relative humidity larger than 70% are denoted by large symbols. For each case the shear, $U_s$, increases along the line from left to right. Focussing on one storm case in Fig. 3.11a, the downdraught strength $|w_{min}|$ becomes smaller as $\max(q_r + q_c)$ decreases. This decrease occurs as the shear, $U_s$, increases. If the environmental relative humidity is identical in all cases, one would expect the strength of the downdraught to be controlled primarily by the amount of liquid water loading within the storm. Comparison of the experiments with large mid-tropospheric relative humidity shows that the tropical cases (Colon, DavgWK, D011120WK) exhibit larger $\max(q_r + q_c)$
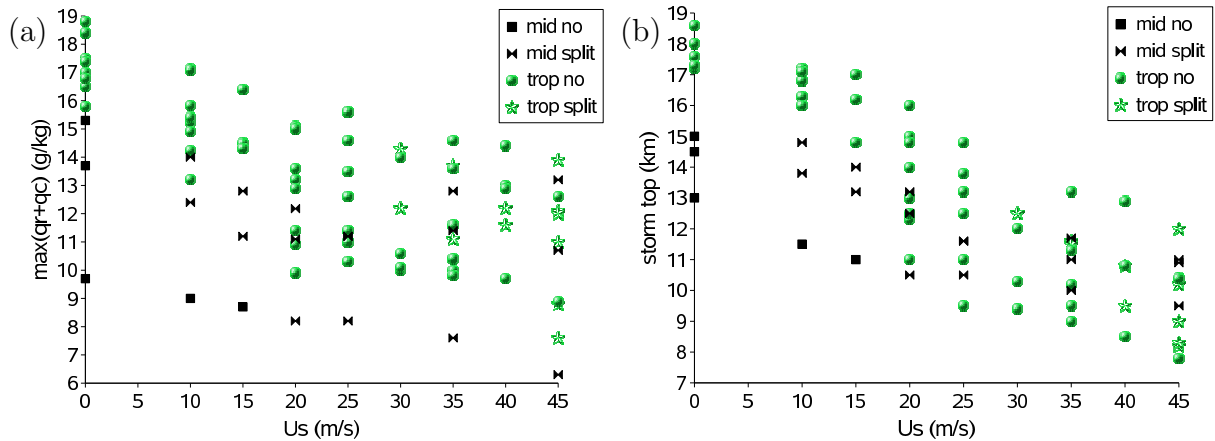
Figure 3.12: Plotted are the (a) maximum of total liquid water versus $U_s$, and (b) the storm top versus $U_s$. The storm top is defined as the height of the 0.1 g kg$^{-1}$ contour of $q_r + q_c$.

and slightly larger $|w_{min}|$ than the mid-latitude cases (mid12, mid14, mid16). When the environmental relative humidity decreases, the contribution of evaporative cooling to the downdraught strength increases. For thunderstorms forming in relatively dry environments (D051114, D042117, D011120, Jordan), the amount of water loading is slightly lower than that in the moister tropical environments (Colon, DavgWK, D011120WK). However, due to more entrainment of dry environmental air leading to more evaporative cooling (small symbols in Fig. 3.11a), $|w_{min}|$ is larger for the cases simulated in dry environments than for those in moist environments (large symbols in Fig. 3.11a). Thus, the tropical storms have stronger downdraughts than the mid-latitude storms either because they grow in an environment with a dryer mid-troposphere, or because the amount of water loading within the updraught is larger. The weaker downdraught in the mid-latitude cases thus leads to a smaller gust front speed than in the tropical cases (see Fig. 3.9).

As discussed before, the overturning efficiency $\alpha$ for a modelled tropical thunderstorm is 20% smaller, on average, than that of a mid-latitude thunderstorm (see Table 3.2). Despite being deeper and thus more prone to the entrainment of environmental air, the tropical updraught has a larger amount of liquid water than the mid-latitude thunderstorm. The drag caused by precipitation loading will reduce the storm's ability to convert CAPE into updraught kinetic energy $w_{max}^2/2$, thereby leading to a smaller overturning efficiency.

The reason for the larger amount of water loading in the tropical storms can be explained with the aid of Fig. 3.11b, where $\max(q_r + q_c)$ versus the water vapour mixing ratio averaged over the lowest 2 km is shown. The water vapour mixing ratio in the lowest 2 km, $q_{v2km}$, for the mid-latitudes ranges between 11 and 14 g kg$^{-1}$ (black squares and hourglasses), while for the tropics, $q_{v2km}$ ranges from 14.5 to 17 g kg$^{-1}$ (green dots and stars). The higher values for $q_{v2km}$ in the tropics account for the large CAPE-values and for the higher liquid water content within tropical storms compared with those in the mid-latitudes. For a given surface $q_v$, the split cases (black hourglasses and green stars) have smaller values of $\max(q_r + q_c)$ than the cases where no split, or an incomplete split occurs (black squares and green dots). The large amount of $\max(q_r + q_c)$ in the tropical storms confirms the assumption of Keenan and Carbone (1992) in that the role of water loading has a relatively greater importance in the dynamics of tropical storms than for

mid-latitude storms due to the moister boundary layer observed in the tropics (Darwin).
The variations of the liquid water content and storm top with wind shear are shown in
Figs. 3.12a and 3.12b, respectively. As $U_s$ increases, the amount of water loading within
the storm decreases owing to the increased entrainment into the storm. Furthermore, with
increasing $U_s$, the storm top decreases as entrainment reduces the strength of the initial
updraught. Thus, at high shears, entrainment reduces the depth and the water loading
of the tropical storms, resulting in a weaker downdraught and thus, in a reduction of the
gust front speed (Fig. 3.9) and/or in a delayed gust front initiation (Fig. 3.10), which then
allows storm splitting to occur.

### 3.2.4   Vertical vorticity

The dynamics of thunderstorms together with the generation of vertical vorticity is de-
scribed in section 1.3 and will be studied now in detail for a selection of the mid-latitude
and tropical thunderstorm cases. For this purpose, time series plots of the maximum mid-
and low-level ($z = 4.6$ km and $z = 0.19$ km) vertical vorticity are presented in Fig. 3.13
for DavgWK where the shear is varied from $U_s = 10, 20, 25$ to $35$ m s$^{-1}$ (Figs. 3.13a, c),
and for mid14, Jordan, Davg, DavWK where $U_s = 35$ m s$^{-1}$ (Figs. 3.13b, d).

#### Initial updraught

The generation of vertical vorticity in the experiments is as described by Rotunno (1981).
During the first 20 minutes of storm growth, mid-level vertical vorticity develops due to
the tilting of the horizontal vortex tubes by the growing updraught. The resulting vortex
couplet is apparent in Fig. 3.14a, where vertical vorticity at mid-levels ($z = 4.6$ km) is
contoured. The southern vortex has $\zeta > 0$ (solid lines), while the northern vortex has
negative values of $\zeta$ (dotted lines). The centre of the updraught (black dot) is located at
$y = 30$ km, $i.e.$ in between the vortex pair.

Figure 3.13a and b show the time evolution of mid-level vertical vorticity of the cyclonic
member of the vortex pair in different experiments. In the DavgWK cases, the peak value
of $\zeta$ for each initial updraught becomes larger with increasing $U_s$ and is largest for the $U_s =
25$ m s$^{-1}$ and $35$ m s$^{-1}$ experiments, at about $t = 15$ min after model initialisation (Fig.
3.13a). The reason for the comparable maxima in mid-level vorticity in these two cases is
that the vertical vorticity production is proportional to the cross-shear horizontal gradient
of vertical velocity and the magnitude of shear, described by the tilting term in Eq. (1.5):

$$\frac{\partial w}{\partial y}\frac{\partial u}{\partial z} - \frac{\partial w}{\partial x}\frac{\partial v}{\partial z}. \tag{3.8}$$

During the first 20 min of the each simulation, the magnitude of vertical velocity $w$ de-
creases with increasing shear (Fig. 3.8c), whereas $\partial u/\partial z$ increases with increasing $U_s$ [see
Eq. (3.5)]. Thus, although the contribution to vorticity production due to shear is larger
in the $U_s = 35$ m s$^{-1}$ case than for the $U_s = 25$ m s$^{-1}$ case, the contribution due to the
gradient of vertical velocity is larger in the $U_s = 25$ m s$^{-1}$ case than in the $U_s = 35$ m s$^{-1}$
case, and this accounts for the comparable size of the tilting terms. The vorticity for the
$U_s = 45$ m s$^{-1}$ case is comparable to that of the $U_s = 20$ m s$^{-1}$ experiment, indicating that
the small gradient of vertical velocity is the dominant term.
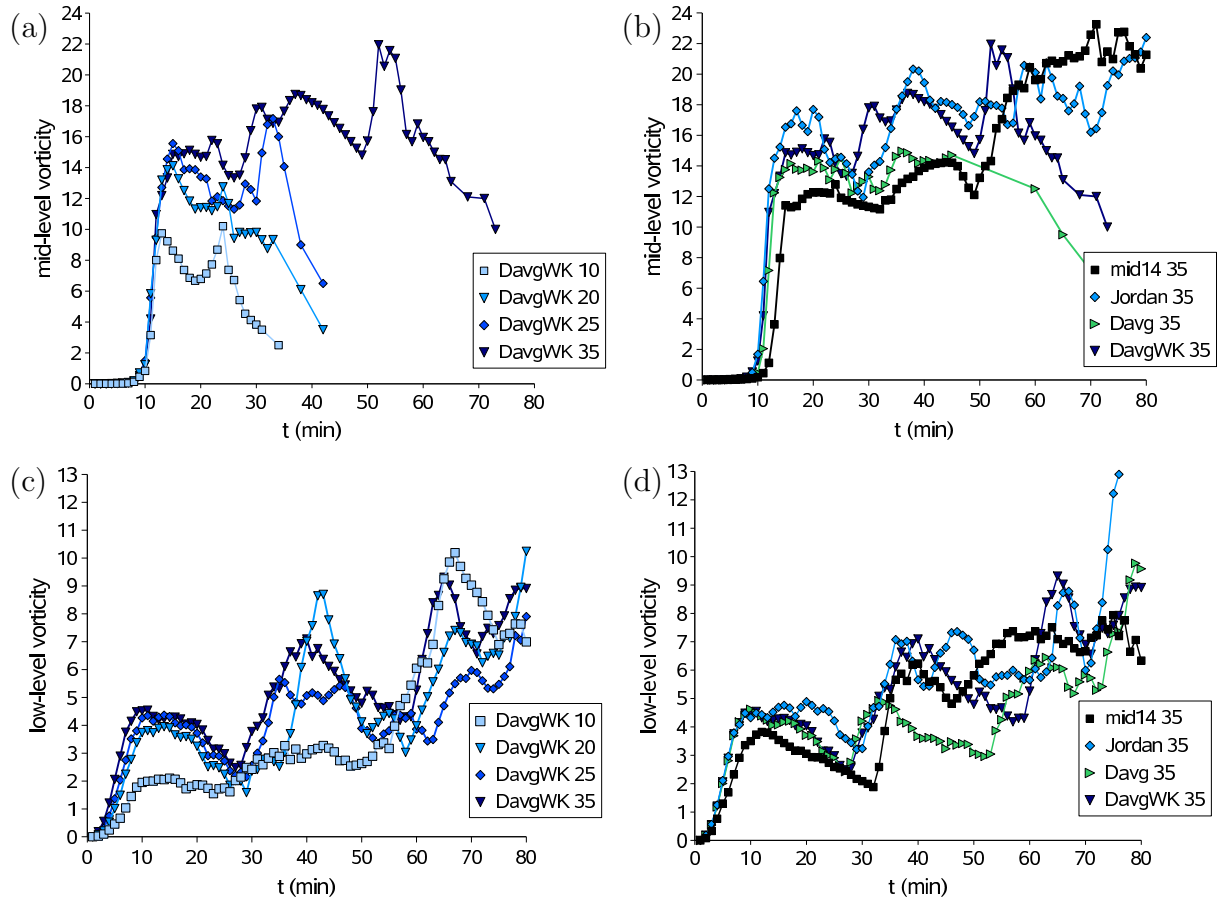
Figure 3.13:  Time series cross-section of mid- ($z = 4.6$ km) and low-level ($z = 0.19$ km) vertical vorticity maximum (in $10^{-3}$ s$^{-1}$) for experiments in different tropical (Jordan, Davg, DavgWK) and mid-latitude (mid14) environments. The number after the model name indicates the shear $U_s$ (in m s$^{-1}$) used.

## Further development

With the weakening initial updraught, the mid- and low-level vorticity decrease about 20 min after model initialisation and the DavgWK storms initialised in environments with $U_s = 10$, 20, and 25 m s$^{-1}$ decay. The DavgWK storm where $U_s = 35$ m s$^{-1}$ splits after 39 min and the mid-level vorticity of the right-mover becomes larger than that of the cyclonic member of the vortex pair within the initial updraught. The vorticity of the left- and right-mover of the Davg $U_s = 35$ m s$^{-1}$ case is shown in Fig. 3.14b. The right-mover possesses cyclonic rotation while the left-mover rotates anticyclonically, with the vortex centres being almost congruent with the centre of the respective updraughts (black dots).

In WK82, significant surface vorticity $\zeta$ did not develop until 40 minutes into the model simulations. However, Figs. 3.13c and 3.13d show that in Bryan's model, low-level vertical vorticity with values up to $5 \times 10^{-3}$ s$^{-1}$ is already present before 40 min due to the tilting of the horizontal vortex tubes and the subsequent stretching of vertical vorticity. The second peak in low-level vertical vorticity at about 40 to 45 minutes coincides with the development of the cold surface outflow, as increased convergence along the gust front is important in creating and tilting the low-level vorticity.
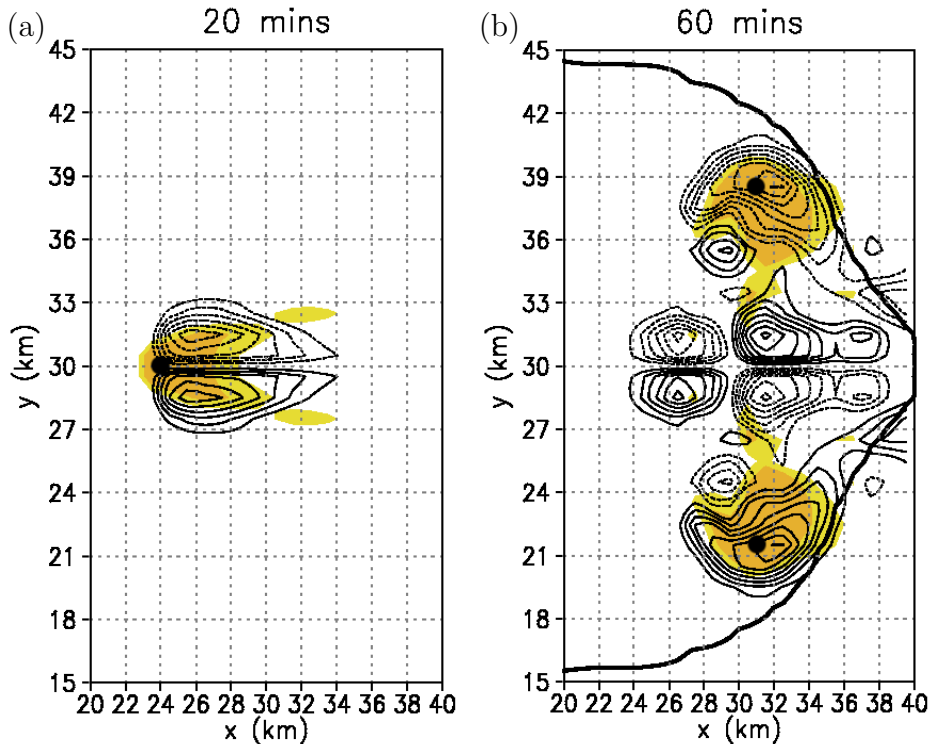
Figure 3.14: Mid-level storm structure depicted at $t = 20$ and 60 min for the Davg case initialised with $U_s = 35$ m s$^{-1}$. The surface gust front is denoted by the thick black line and represents the $-0.5$ K temperature perturbation contour. Regions of updraught velocities at $z = 4.6$ km larger than 5 m s$^{-1}$ and 10 m s$^{-1}$ are shaded in yellow and orange, respectively. The locations of the strongest updraught centres are denoted by black dots. Vertical vorticity $\zeta$ at $z = 4.6$ km is contoured every $2 \times 10^{-3}$ s$^{-1}$, with positive values depicted by the solid lines and negative values represented by the dotted lines.

Examining the four cases in Fig. 3.13b, where the thunderstorms are initialised in environments with $U_s = 35$ m s$^{-1}$, mid-level vorticity is largest in the Jordan case with a peak value of $17.6 \times 10^{-3}$ s$^{-1}$ and smallest for the mid14 case with a peak value of $12.3 \times 10^{-3}$ s$^{-1}$. After 20 minutes into each experiment, the mid-level vorticity in all cases decreases as the initial updraught weakens. While the Davg storm decays without splitting, the Jordan and DavgWK storms undergo splitting without intensification (after 34 and 39 min, respectively), and the mid14 updraught splits with intensification after 46 min. At the time of updraught splitting, the DavgWK case exhibits the largest mid-level vorticity followed by the Jordan and Davg storm, while the mid14 case has the lowest mid-level vorticity until 55 min. A strong mid-level rotation on the updraught flanks acts to lower the pressure and thereby induces updraught growth on the flanks enhancing the splitting (Klemp 1987). As the Davg case has a larger mid-level vorticity than the mid14 case until 55 minutes, one would expect that the Davg storm would be more likely to split than the mid-latitude storm. However, the mid14 storm undergoes splitting with intensification, while the Davg initial updraught decays. This contradiction shows that in the cases studied here, the amount of mid-level vorticity at the time of splitting is not a good indicator for the likelihood of splitting and plays a minor role in comparison with the

gust front.

The vertical vorticity in Clark's model is smaller, on average, than that in Bryan's model (see Wissmeier and Goler 2009). This difference can be explained by the smaller updraught vertical velocities of the thunderstorms simulated with Clark's model than of those simulated with Bryan's model (see Table 3.2). The weaker updraughts lead to less tilting and subsequent stretching of the vortex tubes. However, the evolution of the vorticity is similar in both models.

## 3.3   Cold clouds

The effect of including the ice phase in Bryan's model (Bice) is investigated now. As for the simulations with warm clouds (Bkess), thunderstorms are initialised in three mid-latitude and eight tropical environments with a range of $U_s$ values. The cases examined here are summarised in Table 3.2.

### 3.3.1   Updraught strength

Table 3.2 shows the maximum updraught velocities $w_{max}$ attained by the thunderstorms in the different environments with $U_s = 0$ m s$^{-1}$. The variation of the updraught strength with height $z$ and time is shown in Figs. 3.15a and 3.15b for Bkess and Bice, respectively. The thunderstorms are initialised in a tropical environment (Davg) with zero vertical wind shear. The inclusion of ice in the model produces stronger updraughts than in the models without ice. While the Davg-Bkess storm produces a $w_{max}$ of 48.3 m s$^{-1}$, the maximum updraught speed reached by the Davg-Bice storm is $55.7$ m s$^{-1}$. The faster updraught when ice is included is due to the additional heat released during freezing and deposition, which increases the buoyancy of the updraught, and has been found in other numerical studies of convection (*e.g.*, GSR04). The larger $w_{max}$ in Bice results in overturning efficiencies, $\alpha$, which are 14% larger, on average, than those in Bkess (see Table 3.2).

The time evolution of $w_{max}$ for a mid-latitude, a Darwin, and a Colon storm is plotted in Fig. 3.16. All three cases are initialised with a wind shear of $U_s = 35$ m s$^{-1}$ and are simulated with Bkess and Bice. When ice is included, the updraught speed of all mid-latitude storms is larger than for the storms without ice at a time of approximately 15 to 20 minutes after model initialisation. However, the updraught speed of the Darwin storms simulated with Bice becomes larger than that in Bkess after 35 minutes. The reason why it takes longer for $w_{max}^{ice}$ to become larger than $w_{max}^{kess}$ in the Darwin ice-case than in the mid-latitude ice-case, is because the ice level[5] lies approximately 1.1 km higher in the Darwin environment than in the mid-latitude environment considered here. As the updraught speeds within the Darwin storms are similar to those of the mid-latitude cases (Fig. 3.16), a longer time is required to transport air above the ice level for it to affect the updraught strength. When ice is included for the Colon storm, the updraught strength becomes larger than that when ice is not included after approximately 18 minutes. This is earlier than for the mid-latitude cases due to the ice level lying just above that of the mid-latitudes, and the initial updraught being stronger than those of the mid-latitude cases. Thus, as soon as the ice level is reached, the additional latent heat release leads to further acceleration of the updraught. Such an "acceleration above the freezing level" was observed by May

---

[5]The ice level is defined here as the height $z$ at which $q_i > 0.1$ g kg$^{-1}$.
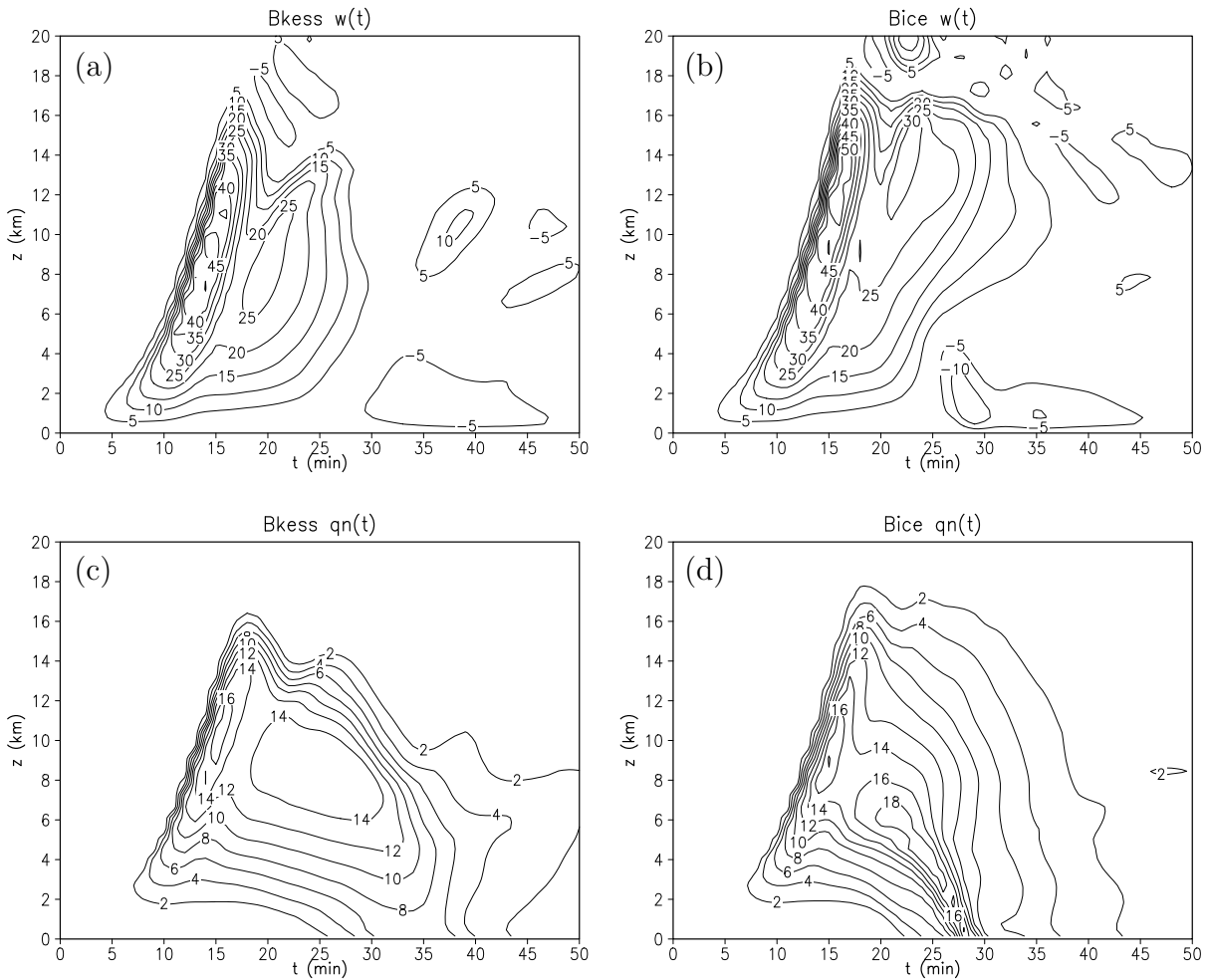
Figure 3.15:  Time-height plots taken at the centre of initial updraught of a tropical thunderstorm (Davg) initialised with (a, c) Bryan's model using the Kessler scheme (Bkess) and (b, d) Bryan's model using ice microphysics (Bice).  Upper panels:  the vertical velocity $w$ is plotted every $5 \text{ m s}^{-1}$, omitting the zero velocity contour. Lower panels: the mixing ratios of (c) liquid water ($q_n = q_r + q_c$) and (d) liquid water and ice ($q_n = q_r + q_c + q_i + q_s + q_g$) are depicted every $2 \text{ g kg}^{-1}$.
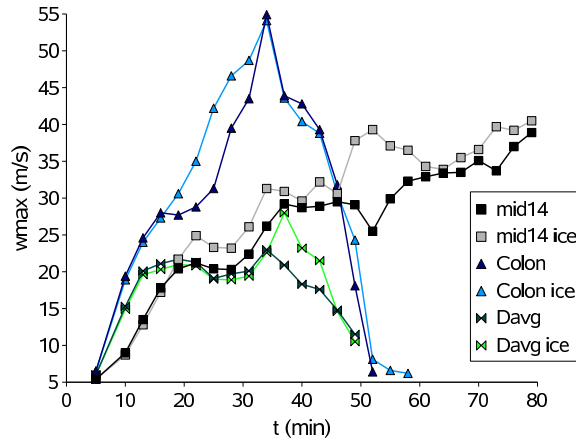
Figure 3.16: Time series plot of maximum vertical velocity $w_{max}$ for the mid14, Davg and Colon experiment, with $U_s = 35$ m s$^{-1}$, each simulated with Bkess and Bice, respectively.

and Rajopadhyaya (1999) in deep convection over Darwin and was attributed to glaciation releasing latent heat.

### 3.3.2 Downdraught and gust front

Figure 3.9b shows the variation of the gust front speed $v_{gf}$ with shear obtained with Bice, where the large dots represent the split-cases. As in Bryan's model without ice, the split-cases can be found at high $U_s$ and small $v_{gf}$ ($< 8.5$ m s$^{-1}$). However, a comparison of Figs. 3.9a and Fig. 3.9b reveals that, on average, the gust front speeds are 25% larger when ice is included. The larger gust front speeds are the result of more hydrometeors produced in Bice than when ice is omitted. This greater density of hydrometeors can be seen by comparing Fig. 3.15c and Fig. 3.15d where the water loading $q_n = q_r + q_c$ of the thunderstorms simulated with Bkess and the water and ice loading $q_n = q_r + q_c + q_i + q_s + q_g$ of those simulated with Bice are depicted, respectively. In addition, heat is extracted from the air in the melting and sublimation of hail/graupel (see GSR04), resulting in a downdraught $w_{min}$, which, on average, is twice as strong in Bice than in Bkess. The strong downdraught in Bice is apparent in Fig. 3.15b, where the peak $w_{min}$ at the cloud base is $-14.8$ m s$^{-1}$ after 29 min, while $w_{min}$ in Bkess is only $-9.1$ m s$^{-1}$ at 37 min (Fig. 3.15a).

### 3.3.3 Storm splitting

The stronger downdraughts and larger gust front speeds in the Bice models result in a slightly different splitting behaviour than in the Bkess experiments. Of the 85 experiments examined with Bice, 68.24% are classified as non-splitting, 3.53% as incomplete splitting, 9.41% as splitting without intensification, and 18.82% as splitting with intensification. The corresponding percentages for Bkess are 63.53% non-splitting, 3.53% incomplete splitting, 12.94% splitting without intensification, and 20.0% splitting with intensification. Thus, when ice is included in the model, the likelihood of a split either with or without intensification is lower than without ice, due to the stronger gust front. However, the main finding of the warm cloud section is confirmed by the simulations with cold clouds in that complete

splitting (with or without intensification) is found in the mid-latitudes for $U_s \gtrsim 10$ m s$^{-1}$, whereas in the tropics $U_s \gtrsim 30$ m s$^{-1}$ is required for complete splitting.

## 3.4    Sensitivity studies

In this section the sensitivity of the updraught strength, the subsequent evolution, and the splitting behaviour to the horizontal resolution, the warm bubble characteristics, and the initial wind profile will be examined.

### 3.4.1    Horizontal resolution

In all simulations presented in this thesis, the horizontal grid spacing is set to 1 km (see Tables 3.1 and 4.1) to enable the large number of experiments to be performed. Two experiments (mid12, Davg) are rerun with Bkess, using $\Delta x = \Delta y = 500$ m. The differences in the peak updraught velocity $w_{max}$ in the high and low resolution models are smaller than 6%, whereby no tendency as regards larger or lower $w_{max}$ for the higher resolution model simulations is apparent.

The splitting behaviour of the modelled thunderstorms is found to be slightly different for the higher horizontal resolution. While the mid12 storm initialised in an environment with $U_s = 15$ m s$^{-1}$ shows no signs of splitting for the $\Delta x = \Delta y = 1$ km case, incomplete splitting occurs for the $\Delta x = \Delta y = 500$ m experiment. For $U_s = 20$ m s$^{-1}$, both experiments show splitting without intensification. In the Davg high and low-resolution experiments, no splitting occurs for $U_s = 35$ m s$^{-1}$, while for a shear with $U_s = 40$ m s$^{-1}$, the thunderstorm in the experiment with $\Delta x = \Delta y = 1$ km splits with intensification, while the storm in the higher resolution run splits without intensification. Thus, the change in resolution leads to slight changes in the updraught strength and splitting behaviour, but no qualitative differences in the thunderstorm evolution were found. Tropical thunderstorms split at higher shears than those in the mid-latitudes, independent of the horizontal resolution used in the numerical model.

### 3.4.2    Thermal perturbation

The sensitivity of the storm's initial updraught strength on the warm bubble parameters (width – depth – excess) is investigated in a tropical environment (Davg) without vertical wind shear. Table 3.3 shows that the maximum vertical velocity of the initial cell and the time at which the peak in $w$ is reached, changes significantly as the characteristics of the warm bubble change. In general, if the depth and width of the bubble are kept constant, a 1 K increase in the temperature excess leads to an increase in $w_{max}$ between about 1 and 8 m s$^{-1}$. Furthermore, larger temperature excesses lead to early peaks in the updraught velocity. When the depth and temperature excess of the warm bubble are kept constant, an increase in the bubble diameter of 1 km leads to an increase of $w_{max}$ of up to 2.6 m s$^{-1}$. In this case, the time of $w_{max}$ occurs later. Thus, a deep and wide warm bubble with a large excess leads to strong updraught velocities, $w_{max}$, as more and/or warmer buoyant air rises and condenses.

Depending on the environmental low- and mid-tropospheric relative humidity and on the amount of vertical wind shear, there are different thresholds for the three parameters

| temperature excess | depth | width 8 km | width 12 km | width 20 km |
|---|---|---|---|---|
| 1 K | 1 km | 35.2 (25) | 45.7 (27) | 57.9 (36) |
| 2 K | 1 km | 43.2 (21) | 51.2 (23) | 60.5 (30) |
| 4 K | 1 km | 48.6 (17) | 54.0 (20) | 61.4 (25) |
| 8 K | 1 km | 48.3 (15) | 57.3 (17) | 64.3 (22) |
| 1 K | 2.8 km | 45.8 (19) | 51.4 (22) | 56.2 (28) |
| 2 K | 2.8 km | 47.0 (16) | 55.0 (19) | 64.0 (25) |
| 4 K | 2.8 km | 51.8 (14) | 58.8 (17) | 67.6 (22) |
| 8 K | 2.8 km | 55.4 (12) | 62.0 (14) | 70.4 (18) |

Table 3.3:   Values of maximum vertical velocity $w_{max}$ (in m s$^{-1}$) of the initial updraught in the Davg model, run with Bkess. The time at which the peak strength is reached is given in parentheses (in min). The depth of the thermal perturbation is set to 1 km (top) and 2.8 km (bottom), the diameter is varied from 8 km, to 12 km, to 20 km, and the temperature excess is chosen as (1, 2, 4, 8) K.

(width – depth – excess) for which the thermal perturbation can still overcome adverse effects. If the environment is too dry and/or if the environmental wind shear is too large, entrainment reduces the buoyant energy of the thermal and it may dissipate soon after initialisation. Often in Clark's model, convection in tropical environments with dry mid-levels could not be triggered with a (20 km – 2.8 km – 2 K) bubble when the wind shear $U_s \geq 25$ m s$^{-1}$. Therefore, a (8 km – 1 km – 8 K) bubble is chosen in the experiments presented in chapters 3 and 4 so that thunderstorms are consistently produced in both Clark's and Bryan's models.

The choice of the warm bubble parameters has an influence also on the timing and characteristics of the downdraught and gust front and thus, on the splitting behaviour. A warm bubble with a large excess causes the development of the initial updraught to be faster than one with a small excess, while a broad warm bubble (20 km) leads to a slower development of the initial updraught than a thin one (8 km). If an updraught develops too rapidly, it may decay even before splitting occurs. A series of experiments, where the three parameters of the warm bubble are varied was carried out with Clark's model. It is found, that the amount of wind shear $U_s$ at which complete splitting occurs, varies at most by 5 m s$^{-1}$, depending on the bubble parameters. However, no matter which bubble parameters are chosen, complete splitting of the mid-latitude updraughts occurs for $U_s \gtrsim 15$ m s$^{-1}$, while a shear of $U_s \gtrsim 25$ m s$^{-1}$ is required for the splitting of tropical storms.

In summary, the choice of the width, depth, and temperature excess of the warm bubble has an influence on the updraught strength and splitting behaviour, but no qualitative differences in the thunderstorm evolution were found. The main finding, that larger wind shears are required for storm splitting in the tropics than in the mid-latitudes is still valid, no matter how the parameters of the thermal which triggered the convection were chosen.

### 3.4.3   Wind profile

The wind profile in the experiments presented so far is given by $[u, v] = [U_s \tanh(z/z_s), 0]$, with $z_s = 3000$ m, giving a shear layer depth $H$ of 6 km (see Fig. 3.2). In order to study
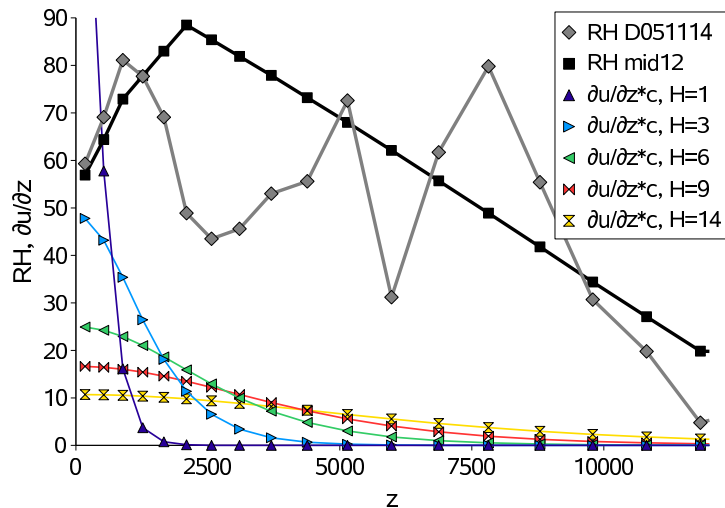
Figure 3.17: Plotted is the relative humidity (RH, in %) versus height $z$ for the D051114 (grey) and mid12 (black) case. Further, $\partial u/\partial z \times c$ (in s$^{-1}$) for different shear layer depths $H$ (in km) is shown. For scaling, $c$ is chosen to be 3000. $\partial u/\partial z$ is given by Eq. (3.9), where $U_s = 25$ m s$^{-1}$.

the sensitivity of the model results to the shear layer depth, $z_s$ is set to (500, 1550, 3000, 4500, 7000) m, giving $H = (1, 3, 6, 9, 14)$ km, respectively. These sensitivity experiments are carried out with Bice for a tropical (D051114) and a mid-latitude (mid12) case. The relative humidities of the D051114 and mid12 environments are shown in Fig. 3.17 in grey and black, respectively.

In D051114, no splitting occurs for the $U_s = 40$ m s$^{-1}$ cases, no matter which shear layer depth is chosen. The increase of the wind shear to $U_s = 45$ m s$^{-1}$ leads to splitting for the case where $H = 6$ km. In the mid-latitude experiments, no splitting is found for the $U_s = 20$ m s$^{-1}$ experiments with $H = 1$ km, 3 km, and 6 km, but $H = 9$ km leads to an incomplete split, and $H = 14$ km results in storm splitting without intensification. An increase of $U_s$ to 25 m s$^{-1}$ shows, that for shallow shear layers ($H = 1$ km and 3 km), the updraught does not split, while for $H = 6$ km and 9 km splitting with intensification, and for $H = 14$ km a split without intensification occurs. Thus, the tendency for an updraught to split is largest when the shear layer depth $H$ is moderate and is smallest when $H$ is small.

This splitting behaviour can be explained by writing the vertical wind shear as

$$
\begin{aligned}
\frac{\partial u}{\partial z} &= \frac{\partial}{\partial z}\left[ U_s \tanh\left(\frac{z}{z_s}\right) \right] \\
&= \frac{U_s}{z_s \cosh^2(z/z_s)}.
\end{aligned}
\tag{3.9}
$$

Figure 3.17 shows $\partial u/\partial z$ versus $z$ for all shear layer depths $H$. When the shear layer has a depth of only 1 km, the updraught is influenced strongly by the immense amount of vertical wind shear, $\partial u/\partial z$, which is concentrated at low-levels. If the buoyancy is sufficiently large, the updraught overcomes the adverse effects of the shear and develops above the shear layer where $\partial u/\partial z$ and thus, entrainment, are negligible. The storm attains large vertical velocities as shown in Fig. 3.18, where the change of the maximum vertical
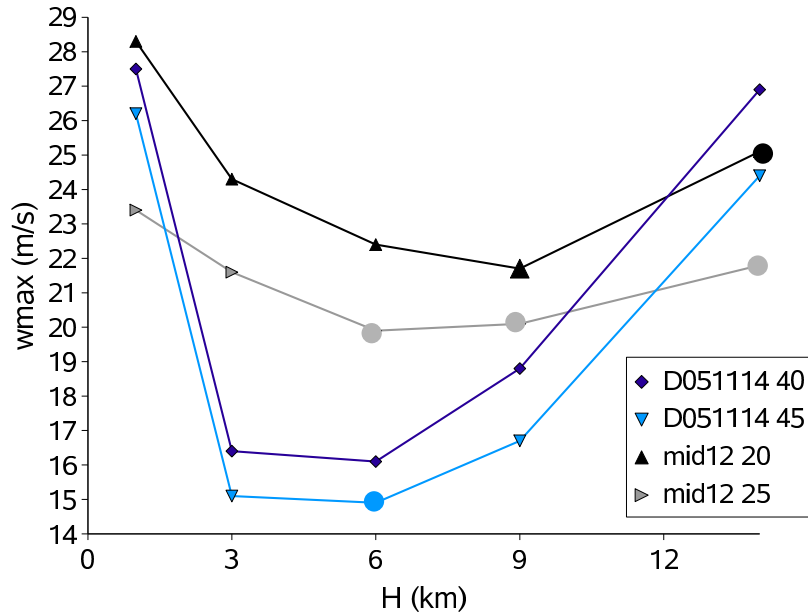
Figure 3.18: Change of maximum vertical velocity $w_{max}$ (in m s$^{-1}$) with shear layer depth $H$ in the D051114 and mid12 experiments, computed with Bice. The number following the model name is $U_s$ (in m s$^{-1}$). Small and large symbols represent the no split and incomplete split cases, respectively, while the dots mark the complete split cases. Note that the amount of shear in the experiments is different.

velocity $w_{max}$ with the shear layer depth $H$ is presented. However, the life time of the storm is short, since the updraught above the shear layer is no longer tilted and the downdraught falls into the updraught. The storm decays immediately after the gust front occurs and thus, has no time to split.

For moderate shear layer depths, $\partial u/\partial z$ is still large at low- and mid-levels, resulting in large entrainment which reduces the updraught strength $w_{max}$ (see Fig. 3.18). Since the relative humidity between $1.5 - 4.5$ km in the tropical case is significantly smaller than that in the mid12 case, for a given $H$ the tropical updraughts are weaker due to the entrainment of dry air. However, the mid12 and D051114 storms in the environment with moderate $H$ live longer than those in environments with small $H$ due to the storm tilting caused by the environmental shear. Moderate amounts of ice and water loading, $\max(q_r + q_c + q_i + q_s + q_g)$, lead to a moderate gust front speed which enables the storm to split.

When $H$ is large, the shear, $\partial u/\partial z$, at low- and mid-levels is weaker than for moderate $H$, resulting in a large $w_{max}$ (Fig. 3.18). The strong updraughts are capable of carrying a large amount of ice and water, which results in a fast moving gust front when the hydrometeors fall and evaporate. The storm becomes cut off from the warm inflow by the fast-spreading gust front before splitting can commence. Thus, the study of storms in environments with different shear layer depths reveals again that the gust front plays an important role in the evolution of the thunderstorm. In the next chapter, the influence of directional wind shear on the thunderstorm strength and evolution will be studied and compared with the results found for the uni-directional shear experiments.

## 3.5    Diagnostic variables to forecast thunderstorm splitting

A diagnostic variable is some quantity, valid at a specific instant in time, that either is a basic observed variable or can be calculated from those variables (Doswell and Schultz 2006). Often such variables are referred to as forecast parameters, even though they are not verified rigorously. The applicability of two diagnostic variables, CAPE and the Richardson number $R$, have been discussed in the previous sections. The aim of this section is to determine a better diagnostic variable that can be used to forecast the likelihood of storm splitting.

For the modelled cases here, it was found that the thresholds of $R$ as given by WK82 are not optimal for predicting storm splitting in the tropics and mid-latitudes. It is apparent from Fig. 3.8a that for the tropical cases modelled with Bkess, where CAPE ranges from 3787 J kg$^{-1}$ to 6084 J kg$^{-1}$, the prediction of whether the storm splits is improved when $U_s \geq 30$ m s$^{-1}$ is taken as an indicator rather than the Richardson number. Then, 77% of the cases are predicted correctly, instead of only 67% when $R$ is used. Of the 21 modelled mid-latitude cases with CAPE values between 840 J kg$^{-1}$ and 2917 J kg$^{-1}$, 90% of the cases are predicted correctly when $U_s \geq 10$ m s$^{-1}$ is taken as an indicator for complete splitting. With the thresholds of the Richardson number, $10 < R < 50$, given in WK82, only 48% of the mid-latitude cases are successfully predicted. Furthermore, Fig. 1.7b (WK82, their Fig. 10c) shows that thresholds for the vertical wind shear can be as good as those for $R$ to predict whether split storms can occur, where all of the cases with CAPE values between 1500 J kg$^{-1}$ and 3600 J kg$^{-1}$ would have been predicted successfully if $U_s = 20$ m s$^{-1}$ is taken as threshold. However, it should be noted that with this technique, one needs to take into account if the thunderstorm environment is characteristic of a mid-latitude or tropical environment.

Rasmussen and Blanchard (1998) established a climatology of parameters commonly used in supercell thunderstorm forecasting and research, with the climatology derived from 0000 UTC soundings from the United States. As in this thesis, they found also that the Richardson number is a poor discriminator between supercell and non-supercell sounding populations, whereas the "energy-helicity index (EHI)" and the "vorticity generation parameter (VGP)" were shown to substantially improve the use of soundings in discriminating between the events. It is not the focus of this work to test every common diagnostic variable, such as EHI and VGP, for all the mid-latitude and tropical cases. Rather it will be shown in the following analysis that with the findings discussed in this chapter, a new diagnostic variable can be derived which predicts split or no-split cases better than the Richardson number and is applicable for forecasting mid-latitude and tropical supercells.

In the previous sections it was found that the likelihood of thunderstorm splitting and thus, for severe storms to occur, increases if

1. the wind shear, $U_s$, increases,

2. the mid-tropospheric relative humidity, $RH_{mid}$, increases (then evaporative cooling is decreased thus reducing the strength of the downdraught and subsequent gust front, allowing the thunderstorm more time to develop and split), and

3. the surface moisture ($q_{v2km}$) decreases (then the amount of hydrometeor loading within the updraught is decreased, leading to a weaker downdraught and gust front).

| quantity / points | 1 | 2 | 3 | 4 | 5 | 6 |
|---|---|---|---|---|---|---|
| $U_s$ (m s$^{-1}$) | < 10 | 10, 15 | 20, 25 | 30, 35 | 40 | 45 |
| $RH_{mid}$ (%) | < 30 | 30–50 | 51–70 | > 70 | – | – |
| $q_{v2km}$ (g kg$^{-1}$) | > 15.5 | 14.1–15.5 | 12.5–14.0 | < 12.5 | – | – |
| CAPE (J kg$^{-1}$) | < 1000 | 1000–2000 | 2001–3000 | 3001–4000 | 4001–5000 | > 5000 |

Table 3.4: Definition of the points system, to be used in Eq. (3.10), indicating the points $P$ (1–6) assigned to the ranges of values for the wind shear magnitude $U_s$, the mid-tropospheric relative humidity $RH_{mid}$ averaged between $p = 850$ and 500 hPa, the surface water vapour mixing ratio averaged over the lowermost 2 km $q_{v2km}$, and CAPE.

For the four parameters $U_s$, $RH_{mid}$, $q_{v2km}$, and CAPE, a "points system" is introduced which is shown in Table 3.4. The system is constructed so that the number of points increases as the likelihood of splitting increases (see items 1–3). The assigned points to the four parameters are then added:

$$\Pi = P_{U_s} + P_{RH_{mid}} + P_{q_{v2km}} + \frac{P_{CAPE}}{3}, \tag{3.10}$$

whereby a large $\Pi$ indicates that splitting is most likely. By trial and error, the factor $1/3$ for $P_{CAPE}$ is included to give the best result for a successful prediction. By applying the points system and Eq. (3.10) to all experiments carried out with Clark's and Bryan's (Bkess, Bice) model, the threshold value for discriminating split and no-split cases is found to be $\Pi_{th} = 10.5$. For example, for the Davg-case with $U_s = 40$ m s$^{-1}$ ($P_{U_s} = 5$), the mid-tropospheric relative humidity is 53.5% ($P_{RH_{mid}} = 3$), the surface moisture is $q_{v2km} = 16.0$ g kg$^{-1}$ ($P_{q_{v2km}} = 1$), and CAPE = 5079 J kg$^{-1}$ ($P_{CAPE} = 6$), giving $\Pi = 11$. The Davg storm splits with intensification, which is predicted correctly by $\Pi = 11$ being larger than $\Pi_{th}$. If $U_s = 35$ m s$^{-1}$ ($P_{U_s} = 4$), $\Pi = 10$ is smaller than the threshold, correctly indicating that the thunderstorm does not split.

The points system, along with Eq. (3.10) and the threshold $\Pi_{th} = 10.5$, successfully predict 85% of all mid-latitude and tropical cases computed with Bryan's and Clark's model. Specifically, for Bryan's model with the Kessler scheme, 86% of the tropical and 81% of the mid-latitude cases are predicted correctly, while the corresponding percentages for the Richardson number are 67% and 48%, respectively. Thus, by using a simple points system and taking into account the findings of the previous sections, the forecast of supercells in the model experiments can be enhanced. Of course, the system cannot and should not be used without thorough climatological verification and further development. For example, the ranges of values given in Table 3.4 and the threshold $\Pi_{th}$ fit well for the experiments computed here, but might change when the points system is tested in reality or applied to the results of other models. Furthermore, even though the points were assigned according to the findings listed as items 1–3, the simple addition of $P_{U_s}$, $P_{RH_{mid}}$, $P_{q_{v2km}}$, and $P_{CAPE}$ has no deeper physical reason than adding probabilities. But for all that, the points system suggested here applies well for the 63 mid-latitude and 192 tropical cases simulated with both cloud-models and using two different microphysics schemes, and provides a basis for the development of new diagnostic variables and forecasting parameters for the mid-latitudes and tropics.

## 3.6   Summary

The influence of vertical wind shear on deep convection in tropical and mid-latitude environments has been investigated using two cloud models. Three vertical temperature and humidity profiles from the mid-latitudes, six Darwin profiles, plus the Colon and Jordan mean profiles were used in the simulations, and the vertical wind shear was varied between 0 and 0.0075 s$^{-1}$. Up to 255 thunderstorm cases were examined. While Clark's model was initialised only with a Kessler-warm-rain-parameterisation, Bryan's model was run with an ice microphysics scheme also.

The principal findings are as follows:

- Thunderstorms that develop in tropical environments require a larger vertical wind shear to split ($U_s \gtrsim 30$ m s$^{-1}$) compared with thunderstorms in mid-latitude environments ($U_s \gtrsim 10$ m s$^{-1}$).

- The propensity for thunderstorms to split depends on the speed at which the gust front expands outwards. A slow gust front allows the updraught more time to split and subsequently develop. The tropical storms modelled here exhibited faster gust fronts than the mid-latitude storms.

- The speed of the gust front increases with the total water loading within the storm and with decreasing mid-tropospheric relative humidity in the environment. The greater water vapour mixing ratio in the tropical subcloud layer leads to more condensation in the tropical updraughts and thus, to more water loading than in the mid-latitude updraughts.

- High wind shears lead to a reduced water loading within the storm, which in turn reduces the speed of the gust front. Larger wind shears are required in the tropical cases than in the mid-latitude cases to reduce the water loading and thus, the speed of the gust front.

- Although CAPE can be significantly larger in tropical environments than in mid-latitude environments, the updraughts of the tropical storms are similar to, and in some cases weaker than, those of mid-latitude storms. The Richardson number with its thresholds for supercells in the mid-latitudes should be used with great caution when applied to the forecast of tropical supercells. Defining a CAPE quantity which excludes the upper tropospheric portion (*i.e.*, considering only the CAPE between 0 and 8 km) was found to be a less useful parameter for the prediction of storm splitting of mid-latitude and tropical storms than the full CAPE.

I examined the sensitivity of the model results to the cloud model, the microphysics, the horizontal resolution, the warm bubble characteristics, and to the wind profile used. Even though quantities such as the maximum vertical velocity within an updraught can vary, no qualitative differences in the thunderstorm evolution and in the splitting behaviour could be found and the principle findings were confirmed.

The study of simulated tropical and mid-latitude storms supports the experience of forecasters at the Bureau of Meteorology in Darwin that the operational storm forecasting tool developed for mid-latitude thunderstorms over-forecasts supercells within the tropics. Thus, there is a need to develop new forecasting tools for severe thunderstorms valid in

the tropics. This work is seen as a first step in such a development. Diagrams such as Fig. 3.8c may be helpful as they indicate both for mid-latitude and tropical environments when split cells are to be expected for a particular wind shear and for the modelled updraught strength $w_{max}$. The combination of Figs. 3.11a and 3.11b might help to estimate the amount of water loading and thus, the strength of the downdraught and gust front if the relative humidity and low-level moisture of the environment are known. If there is a way to estimate the gust front speed, a diagram such as Fig. 3.9 would aid to predict the likelihood of splitting for a given wind shear. A points system which takes into account the findings of this chapter was introduced to diagnose the likelihood of storm splitting and was shown to be successful for the storms modelled here. However, this is just a first step and such a points system would need to be verified using actual observations and/or other modelling studies.

# Chapter 4

# The influence of directional wind shear on convection

Often the environments in the vicinity of severe thunderstorms show considerable veering[1] of the wind shear vector with height. Thus, it is of great importance to understand how a curved wind hodograph affects thunderstorm splitting. In the present chapter the influence of directional wind shear on tropical convection is examined and compared with the results of mid-latitude simulations. The results of the mid-latitude simulations will be based on the model experiments presented herein and on previous work by Weisman and Klemp (1984, hereafter WK84) and Gilmore *et al.* (2004, hereafter GSR04). In the first subsection, the model configuration is explained, while in subsection 4.2 results of experiments in a mid-latitude and in two tropical environments are studied and compared with those of chapter 3. A summary will be given in the last subsection.

## 4.1 Model configuration and experiments

The simulations of deep convection in directionally sheared environments are performed with Bryan's model using ice microphysics. The model configuration, such as the domain size and grid spacing, as well as the parameters of the thermal perturbation are summarised in Table 4.1 along with those chosen in WK84 and GSR04.

The model is initialised with three different temperature and humidity profiles which were described in section 3.1. Two of the profiles represent tropical environments (Darwin average-profile Davg, Colon profile), while the third profile is representative of a mid-latitude environment with a surface mixing ratio of $q_{v0} = 14$ g kg$^{-1}$ (mid14). The convection is triggered using a thermal perturbation of the same size and temperature excess as in the model runs with uni-directional shear, so that a comparison with these experiments can be made.

The wind profile is defined as in WK84 and GSR04, where the shear vector turns through 180° over the lowest $h = 5$ km of the sounding (see Fig. 4.1), and is constant for $h > 5$ km. For $0 < z < h$, the horizontal wind components are given by

$$u(z) = \frac{u_{max}}{2} \left[ 1 - \cos\left(\frac{z\pi}{h}\right) \right] \tag{4.1}$$

---

[1]A veering wind in the northern (southern) hemisphere is a wind which rotates clockwise (anticlockwise) with increasing height.

| Parameter | Bryan | WK84 | GSR04 |
|---|---|---|---|
| Horizontal domain size | $(60 \times 60)$ km$^2$ | $(60 \times 60)$ km$^2$ | $(90 \times 90)$ km$^2$ |
| Horizontal grid $\Delta x$, $\Delta y$ | 1 km | 1 km | 1 km |
| Vertical domain size | 36 km | 17.5 km | 20 km |
| Vertical grid $\Delta z$ | $(0.3 - 1)$ km | $(0.35 - 1)$ km | 0.5 km |
| Microphysics | ice | Kessler | Kessler, ice |
| Warm bubble width | 8 km | 20 km | 20 km |
| Warm bubble depth | 1 km | 2.8 km | 2.8 km |
| Warm bubble excess | 8 K | 1 K | 1 K |

Table 4.1:   Experiments with a curved hodograph: Comparison of various parameters set in Bryan's model and chosen in WK84 and GSR04.

and

$$v(z) = \frac{u_{max}}{2} \sin\left(\frac{z\pi}{h}\right), \tag{4.2}$$

where $u_{max} = 2U_s/\pi$ and $U_s$ is the magnitude of the velocity variation measured along the arc of the hodograph curve. $U_s$ is proportional to the shear vector magnitude, giving a similar distribution of shear magnitudes as in the uni-directional wind shear experiments. Model simulations are performed using $U_s = (15, 25, 35, 45)$ m s$^{-1}$, corresponding to mean shear magnitudes of $(3, 5, 7, 9) \times 10^{-3}$ s$^{-1}$, respectively. The domain is translated at a constant velocity $(u_{move}, v_{move}) = (U_s/4, U_s/7)$, which was determined through trial and error.

## 4.2   Mid-latitude and tropical thunderstorms

### 4.2.1   Thunderstorm evolution

The tropical thunderstorm initialised in the Davg environment, where the hodograph is curved with $U_s = 35$ m s$^{-1}$, is depicted in Figs. 4.2 and 4.3. The upper panels show the mid-level storm structure with total precipitation contoured in grey, while the lower panels depict the low-level storm structure with horizontal divergence

$$\nabla_h \cdot \mathbf{u}_h = \frac{\partial u}{\partial x} + \frac{\partial v}{\partial y} \tag{4.3}$$

and convergence represented by dashed and solid blue lines, respectively. Yellow and orange shadings represent the regions of updraught, while green and blue shadings denote the regions of downdraught at cloud base ($z = 1.1$ km). The locations of the strongest updraught centres at $z = 4.6$ km are marked by black dots.

By 20 min into the simulation, the updraught is located at $(x, y) = (15.5$ km, $30.0$ km) (black dot in Fig. 4.2a) and is still in its developing stage. The rising air leads to convergence at low-levels, which is apparent in Fig. 4.2b (blue solid lines). The environmental winds tilt the updraught towards the east (compare orange shading in Figs. 4.2a and b). After 30 min, the initial updraught attains its maximum vertical velocity of 27.0 m s$^{-1}$. Prior to this time, a downdraught (green shading in Fig. 4.2b) forms northeast of the updraught. After 21 min, the downdraught produces a surface gust front that spreads out,
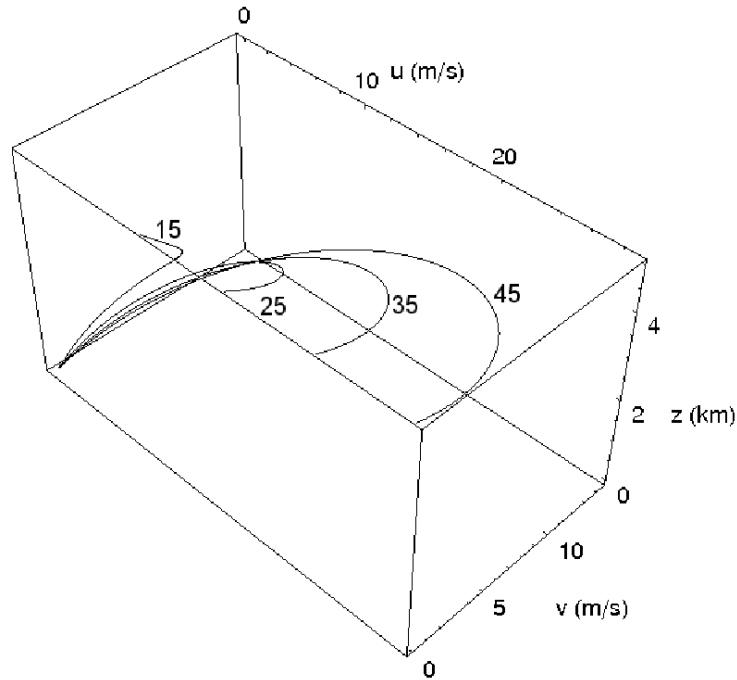
Figure 4.1: Schematic, showing the horizontal wind components $u$ and $v$ below $z = 5$ km given by Eqs. (4.1) and (4.2), for different magnitudes of wind velocity $U_s = (15, 25, 35, 45)$ m s$^{-1}$.

causing low-level convergence at the leading edge, which results in upward motion on the right (southern) and left (northern) flanks of the storm. The updraught splits at 39 min, and both updraught cores are apparent in Fig. 4.2c. In general, surface convergence is larger on the left flank than on the right flank (see Fig. 4.3b), as the low-level outflow on the left flank is more strongly opposed to the storm relative inflow. New updraughts develop on the storm's left flank in response to this strong low-level convergence (Fig. 4.3a). The right flank storm, located at $(x, y) = (20.5$ km, 25.5 km) in Fig. 4.3a, moves to right of the mean wind, as shown by Figs. 4.3a and 4.3c. By 60 min into model simulation, the updraught on the right flank reaches a speed of 33.6 m s$^{-1}$, which increases further due to the continuous supply of warm and moist low-level air lifted by the gust front. The right moving updraught is correlated with positive vertical vorticity and has the structure of a supercell. A peak updraught speed of $w = 50.1$ m s$^{-1}$ is reached after 80 min and the updraught survives the model time of 120 minutes.

The evolution of the tropical thunderstorm (Davg) is similar to that of the mid-latitude thunderstorms (mid14) simulated here (not shown), and to that described in WK84 and GSR04. However, while in WK84 and here, the splitting of the mid-latitude updraught occurs for $U_s \gtrsim 20$ m s$^{-1}$ and $U_s \gtrsim 15$ m s$^{-1}$, respectively, a shear of $U_s \gtrsim 35$ m s$^{-1}$ is necessary for storm splitting in the tropical Davg-case. For shears lower than 35 m s$^{-1}$, the Davg initial updraught decays without the evolution of left and/or right flank cells. However, the tropical thunderstorm growing in the environment initialised with the Colon profile splits when $U_s = 25$ m s$^{-1}$, although the right flank cell is weak and decays after about 60 min (not shown). Thus, the magnitude of shear needs to be larger in the tropics than in the mid-latitudes for splitting to occur with subsequent evolution of the left and right flank cells. This result is consistent with that found in chapter 3, where complete
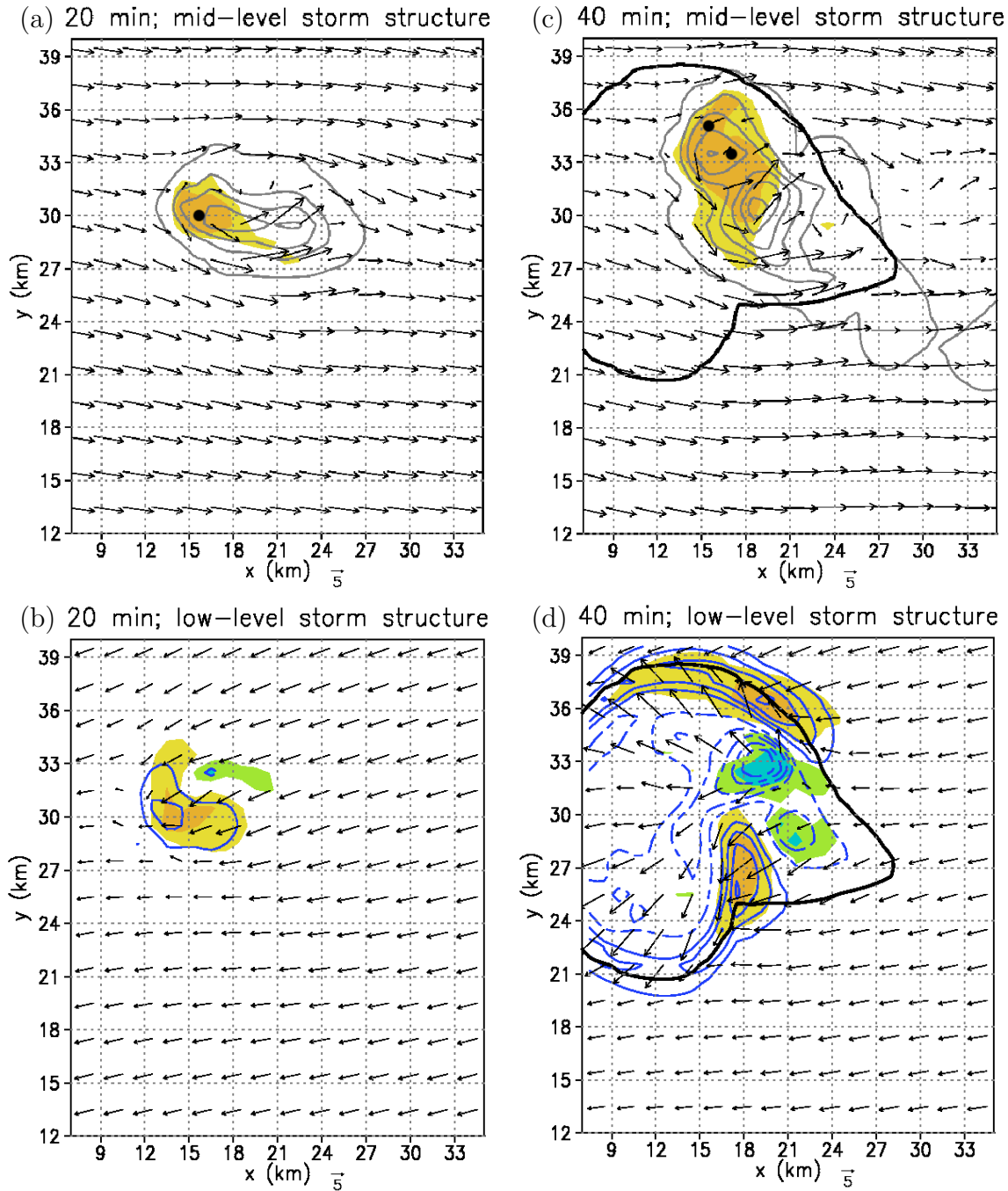
Figure 4.2:   Mid-level and low-level storm structure depicted at $t = 20$ and $40$ min for the Davg-case initialised with $U_s = 35$ m s$^{-1}$. The surface gust front is denoted by the thick black line and represents the $-0.5$ K temperature perturbation contour. Panels (a) and (c): Vectors represent horizontal flow at $z = 4.6$ km and the total precipitation mixing ratio $q_n = q_r + q_s + q_g$ is contoured in grey at 2 g kg$^{-1}$ intervals, with the zero contour omitted. Regions of updraught velocities at $z = 4.6$ km larger than 5 m s$^{-1}$ and 10 m s$^{-1}$ are shaded in yellow and orange, respectively. The locations of the strongest updraught centres are denoted by black dots. For the explanation of the panels (b) and (d), see Fig. 4.3.
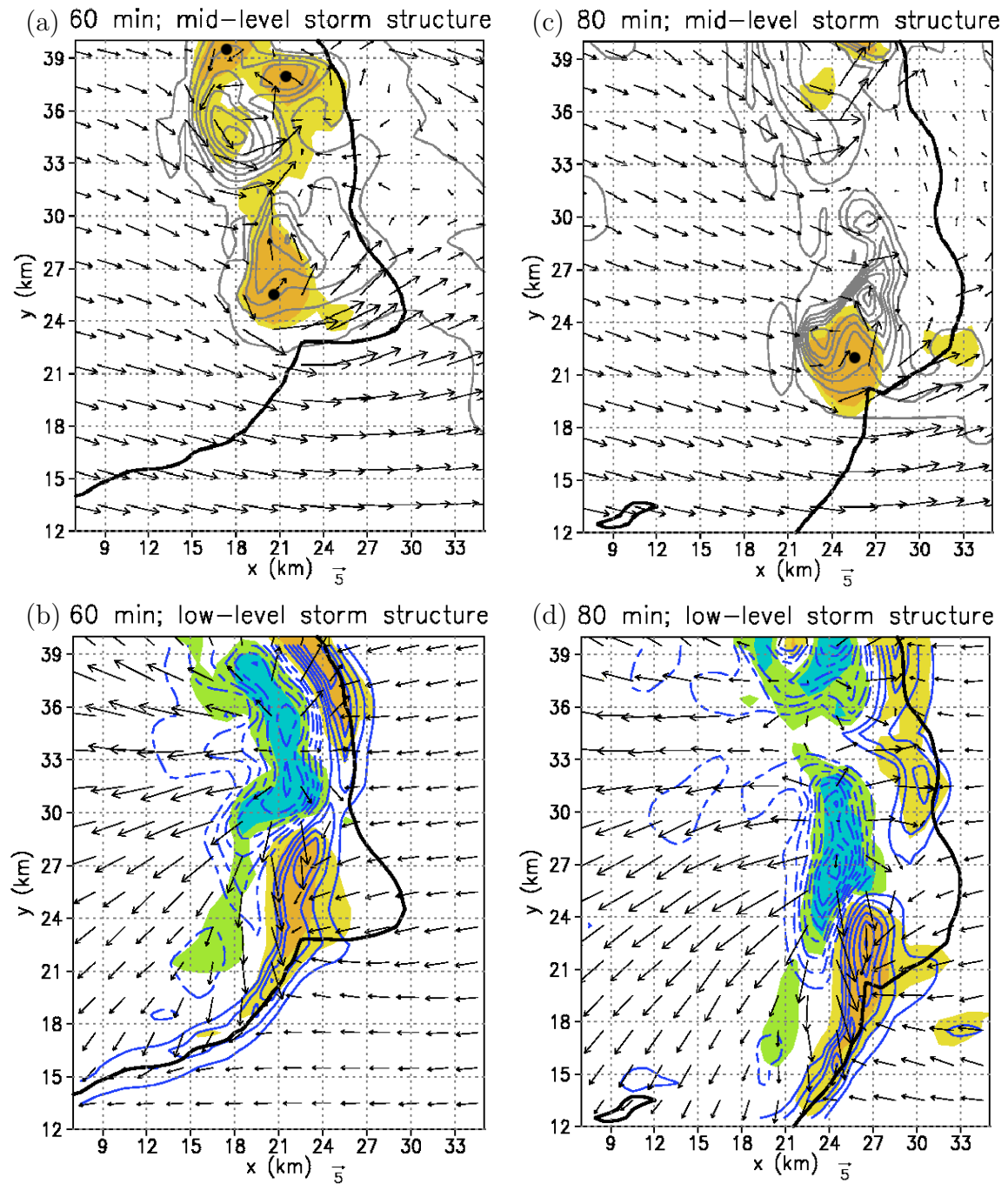
Figure 4.3: Same as in Fig. 4.2, but for $t = 60$ and 80 min. Panels (b) and (d): Vectors represent the horizontal flow at the surface, and the surface divergence and convergence are contoured (dashed/solid) in blue at $2 \times 10^{-3}$ s$^{-1}$ intervals, with the zero contour omitted. Regions of updraught velocities at cloud base ($z = 1.1$ km) larger than 2 m s$^{-1}$ and 5 m s$^{-1}$ are shaded in yellow and orange, while regions of downdraught $< -2$ m s$^{-1}$ and $< -5$ m s$^{-1}$ are shaded in green and light blue, respectively.
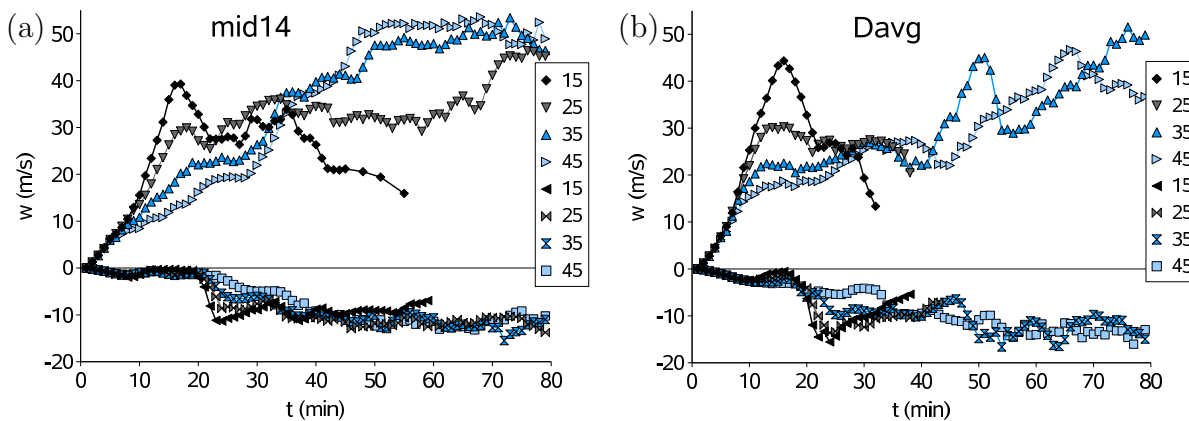
Figure 4.4: Maximum updraught velocity, $w_{max}$, of the initial cell and eventually subsequent right flank cell, and their minimum downdraught velocity, $w_{min}$, taken at cloud base ($z = 1.1$ km) as a function of time for the (a) mid14, and (b) Davg experiment. The amount of wind shear is varied by altering $U_s$ from (15, 25, 35 to 45) m s$^{-1}$.

splitting occurs in the mid-latitudes for a straight-line hodograph with $U_s \gtrsim 10$ m s$^{-1}$, whereas in the tropics a much larger wind shear ($U_s \gtrsim 30$ m s$^{-1}$) is required for complete splitting to occur.

## 4.2.2 Updraught and downdraught

The nature of the wind shear – storm structure relationship is reflected in the $w(t)$-plots Fig. 4.4a for the mid-latitude (mid14) and Fig. 4.4b for the tropical (Davg) storms. The peak updraught velocity, $w_{max}$, is determined within the whole domain for the initial updraught and the right flank cell. The downdraught strength, $w_{min}$, is measured at cloud base ($z = 1.1$ km). The amount of wind shear is varied by altering $U_s$ from (15, 25, 35 to 45) m s$^{-1}$.

A comparison of the maximum vertical velocity of the Davg and Colon storms in directionally sheared environments with those in uni-directionally sheared environments shows that the Davg-$w_{max}$ are 16.5% larger, and the Colon-$w_{max}$ 41.6% larger when the hodograph is curved. The comparison of the $w_{max}(t)$-plots in Weisman and Klemp (1982) (their Fig. 3) and WK84 (Fig. 5a), confirms this finding for the mid-latitude cases in that the updraught is stronger when the hodograph is curved rather than a straight-line. The reason for this difference is explained in section 4.2.3.

The updraught strength of the Davg initial cells in the curved hodograph experiments is comparable to that of the mid14 updraughts. However, the peak downdraught strength $|w_{min}|$ in Davg is 38.5% larger, on average, than in mid14 (compare Figs 4.4a and b). The downdraughts of the Colon storms are even 69.9% greater than those of the mid-latitude storms. The stronger downdraughts in the tropical storms result from a larger amount of precipitation loading within the storm than that in the mid-latitude storms, as explained in chapter 3. The difference in precipitation loading is apparent from Figs. 4.5a and 4.5b, where the maximum of the total mixing ratio $q_n = q_r + q_c + q_i + q_s + q_g$ is plotted with time for the mid14 cases and Davg cases, respectively. An intense downdraught results in
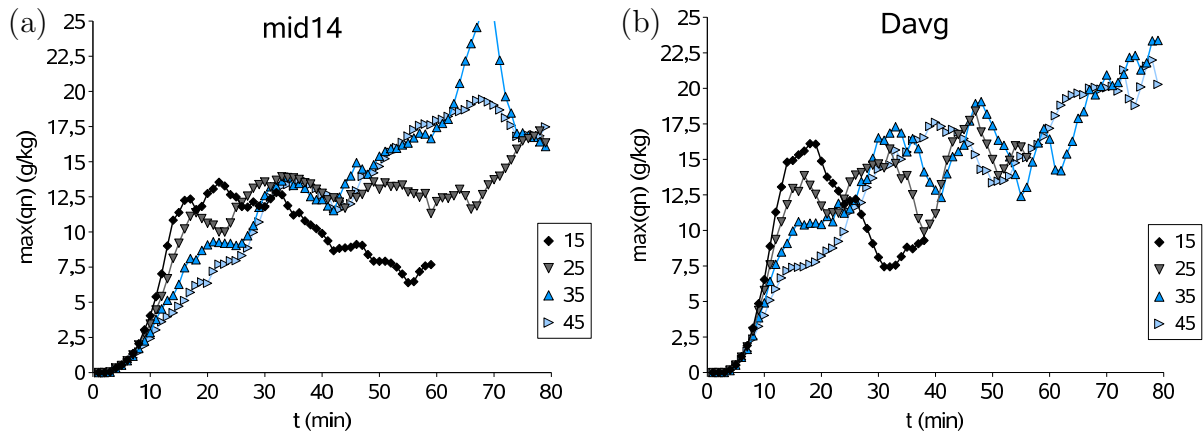
Figure 4.5: Maximum of the total mixing ratio $q_n = q_r + q_c + q_i + q_s + q_g$ of the initial updraught and eventually subsequent right-mover as a function of time for the (a) mid14, and (b) Davg experiment. The amount of wind shear is varied by altering $U_s$ from (15, 25, 35 to 45) m s$^{-1}$.

a stronger gust front in the tropical cases than in the mid-latitude cases, which cuts off the supply of warm air earlier in the storm's lifetime, leading to its dissipation.

For the cases where left and right flank cells developed (all but the Davg $U_s = 15$ and 25 m s$^{-1}$ cases), the maximum updraught speed of the right flank cell of the mid14 and Davg experiments is depicted in Figs. 4.4a and 4.4b, respectively ($t > 25$ min). Figure 4.4a shows that the strength of the right moving supercell increases with increasing wind shear. This intensification of the right flank cell at large wind shears is apparent also for the Colon cases (not shown) and was found in WK84 (their Fig. 5a). The dynamics of this effect will be discussed in section 4.2.3.

## 4.2.3 Thunderstorm dynamics

Rotunno and Klemp (1982) have shown that, in supercell development, the vortex pair which is generated through the tilting of horizontal vortex tubes is normal to the shear vector. Thus, in the uni-directional shear cases with $u(z) > 0$, mirror-image vortex pairs are created south and north of the initial updraught. This feature is confirmed by numerical experiments examined in chapter 3, which showed that the southern cell rotates cyclonically, while the northern cell rotates anticyclonically (Fig. 3.14b).

### Early stages

In environments where the hodograph is curved clockwise, the southern updraught is favoured because of vertical pressure gradient forces which are larger on the southern flank than on the northern flank of the storm system. Pressure gradient forces contribute to the acceleration of vertical momentum, described by

$$\frac{Dw}{Dt} = \underbrace{-c_p \theta_\rho \frac{\partial \pi'}{\partial z}}_{\text{pressure gradient}} + \underbrace{g \left( \frac{\theta_\rho}{\theta_{\rho 0}} - 1 \right)}_{\text{buoyancy}}, \tag{4.4}$$

(a)



straight-line
hodograph

curved
hodograph

(b)
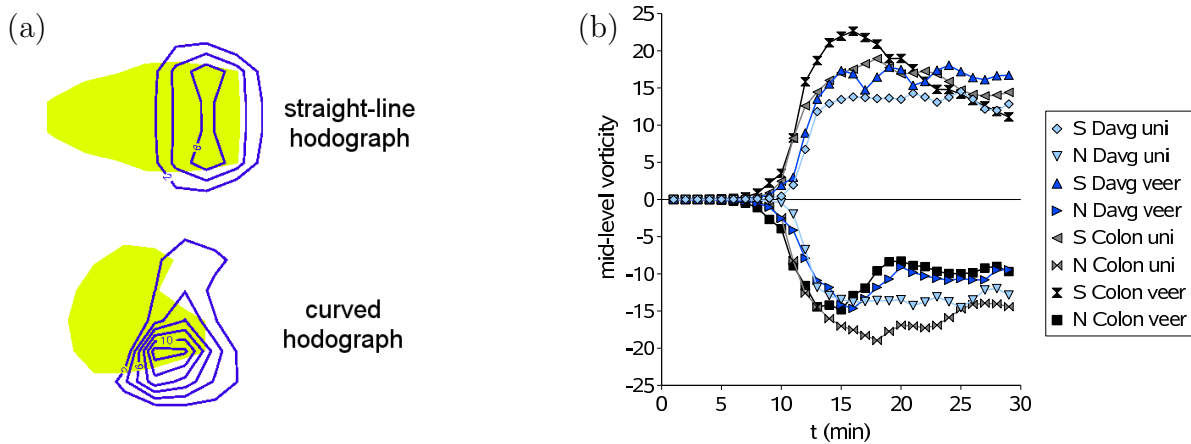


Figure 4.6:   (a) Horizontal cross-section through the Davg $U_s = 35$ m s$^{-1}$-storm, initialised in an environment with a straight-line (top) and a curved (bottom) hodograph. The cross-section is through $z = 3$ km, 15 min after model initialisation. Shading represents regions of ascent with $w > 5$ m s$^{-1}$, and the contours show the positive contributions of the pressure gradient force to the vertical acceleration with interval $2 \times 10^{-2}$ m s$^{-2}$, and the zero-contour omitted. (b) Time series cross-section of mid-level ($z = 4.6$ km) vertical vorticity maxima (in $10^{-3}$ s$^{-1}$) for the Davg and Colon experiments with $U_s = 35$ m s$^{-1}$. $S$ and $N$ represent the southern or northern vortex of the couplet, and "uni" and "veer" stand for the uni-directional wind shear experiments, and experiments with veering wind shear, respectively.

where $\theta_\rho$ is the density potential temperature and $\pi'$ is the perturbation of the non-dimensional pressure (see section 2.2.1 for the derivation of the momentum acceleration equation). Figure 4.6a shows horizontal cross-sections through an updraught initialised in an environment with a straight-line hodograph (top) and with a curved hodograph (bottom). Regions of $w > 5$ m s$^{-1}$ are shaded, and the contribution of the pressure gradient term to the vertical momentum acceleration [Eq. (4.4)] is contoured every $2 \times 10^{-2}$ m s$^{-2}$. In the uni-directional shear case, the perturbation pressure gradient force on the southern and northern flanks of the updraught centre is the same, with values of about $7 \times 10^{-2}$ m s$^{-2}$ (Fig. 4.6a, upper panel). When the hodograph is curved clockwise (lower panel), the pressure gradient force is $13 \times 10^{-2}$ m s$^{-2}$ on the southern flank, compared with $2 \times 10^{-2}$ m s$^{-2}$ on the northern flank. Rotunno and Klemp (1982) showed that these favourable vertical pressure gradients on the southern flank are dynamically induced through the change in direction of the shear vector with height. Since in the curved hodograph experiments the strong pressure gradients supply a large positive contribution to the vertical acceleration, the updraughts are stronger than those in environments with uni-directional wind shear, as found in section 4.2.2.

**Vertical vorticity**

In Figs. 4.7a to 4.7d, the mid-level vertical vorticity within a Davg storm is contoured, with positive and negative values of $\zeta$ depicted by solid and dashed lines, respectively. Regions of $w > 5$ m s$^{-1}$ are shaded and the black dots mark the centre of the updraughts. As the updraught grows in a vertically sheared environment, a vortex couplet is generated
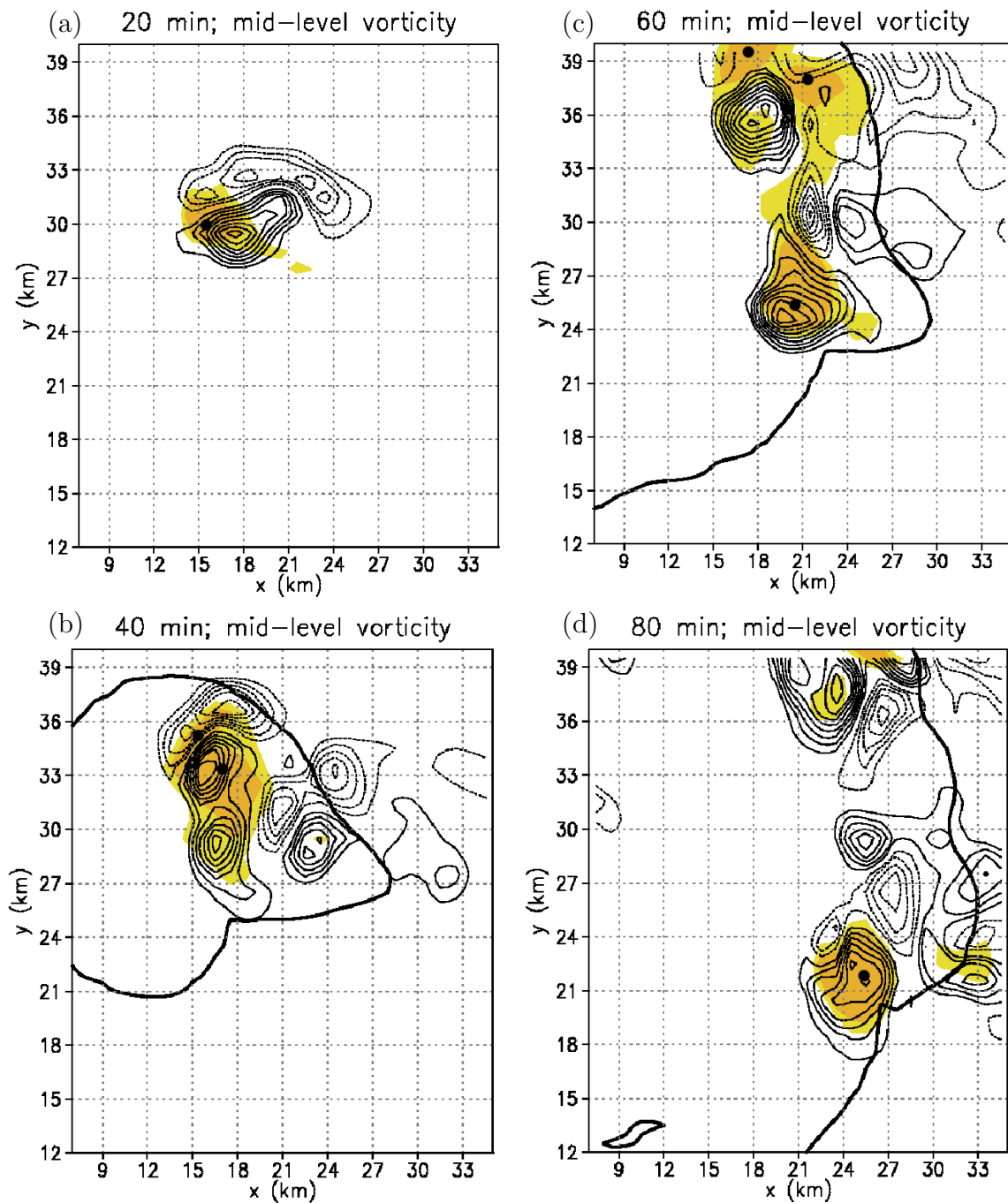
Figure 4.7:   Mid-level storm structure depicted at $t = 20$, 40, 60, and 80 min for the Davg case initialised with $U_s = 35$ m s$^{-1}$. The surface gust front is denoted by the thick black line and represents the $-0.5$ K temperature perturbation contour. Regions of updraught velocities at $z = 4.6$ km larger than 5 m s$^{-1}$ and 10 m s$^{-1}$ are shaded in yellow and orange, respectively. The locations of the strongest updraught centres are denoted by black dots. Vertical vorticity $\zeta$ at $z = 4.6$ km is contoured every $2 \times 10^{-3}$ s$^{-1}$ with positive values depicted by the solid black lines, negative values represented by the dotted black lines, omitting the zero contour.
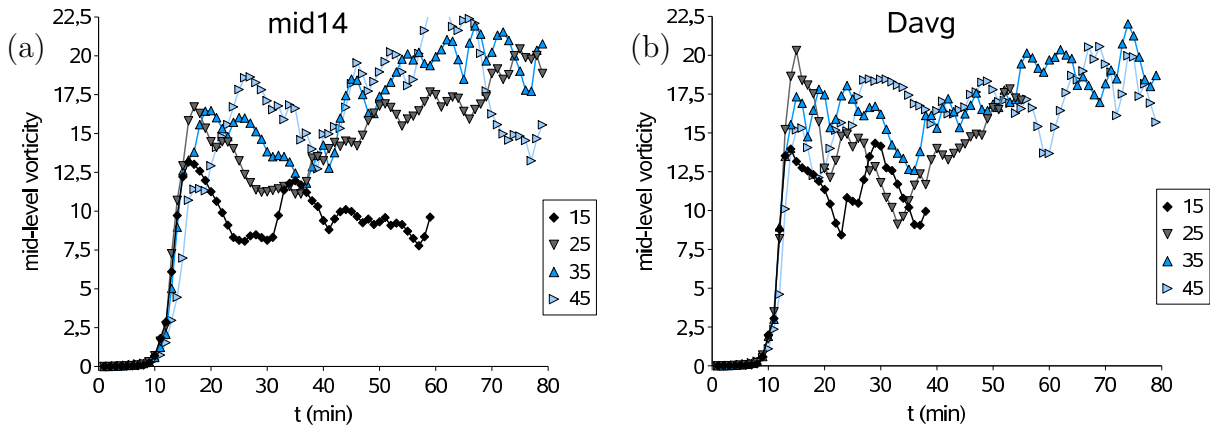
Figure 4.8:   Time series cross-section of mid-level ($z = 4.6$ km) vertical vorticity maxima (in $10^{-3}$ s$^{-1}$) for the (a) mid14, and (b) Davg experiment. The amount of wind shear is varied by altering $U_s$ from (15, 25, 35 to 45) m s$^{-1}$.

due to the tilting of the initially horizontal vortex tubes. Such a vortex couplet is apparent in Fig. 4.7a, where the southern vortex is stronger in terms of $w$ and $\zeta$ than the northern one.

Figure 4.6b shows the change of mid-level vertical vorticity with time for the Davg and Colon experiments carried out with $U_s = 35$ m s$^{-1}$. The peak vertical velocity, $w_{max}$, of the initial updraughts is reached between 16 and 21 minutes and thus, only the first 30 min of storm evolution will be studied now. As the southern vortex possesses cyclonic rotation, its mid-level vorticity is depicted by the curves with $\zeta > 0$ in Fig. 4.6b, while the northern vortex exhibits anticyclonic rotation with $\zeta < 0$. From Fig. 4.6b it is apparent that the vertical vorticity of the southern vortices is larger than that of the northern vortices in the veering shear experiments. Furthermore, the vertical vorticity of the southern vortex is larger in the experiments with a veering shear vector than in those with uni-directional wind shear, while the reverse is true for the vorticity of the northern vortex. The different amounts of vorticity are caused by the different pressure gradient forces which is smallest for the northern flank of the veering shear case, followed by the uni-directional shear case, and largest for the southern flank of the veering shear cases (Fig. 4.6a).

The evolution of mid-level vorticity of the mid14 and Davg storms, initialised in environments with different values of wind shear, is shown in Fig. 4.8a and 4.8b, respectively. In these figures, the vorticity of the initial updraught and that of the subsequent right flank cell is depicted. As found for the uni-directional shear experiments, the peak vertical vorticity of the initial updraught is smallest for the weak shear experiment and increases for larger values of $U_s$. The lack of the monotonic increase of $\zeta$ with increasing $U_s$ can be explained by the two counteracting factors described in section 3.2.4. Although the contribution to vorticity production due to shear is large in the experiments with large $U_s$, the contribution to vorticity production due to the gradient of vertical velocity is larger in the experiments with small $U_s$ [see Figs. 4.4, and Eq. (1.5)].

**Later stages**

So far, only the dynamics of the initial updraught with the favouring of the right flank of the storm system was described. I focus now on the further development. After about 20 to 30 min into the model simulation, the left and right flank Davg storms start to propagate. From Figs. 4.7c and 4.7d it is apparent that the Davg right flank storm possesses cyclonic rotation, $\zeta > 0$, with the vortex centre close to the centre of the updraught. However, the left flank updraughts in Fig. 4.7c exhibit no preferred sense of rotation and furthermore, show no significant correlation between the centre of the vortex and the centre of the updraught. This lack of correlation for the left flank updraughts was found also in WK84 and in Weisman and Klemp (1982) for secondary cells (multicells).

The dynamic character of the left and right flank storms was studied in WK84 and will not be addressed here in detail. However, the relevant equations are given in section 2.2.1. In WK84, contributions to the perturbation pressure $\pi' = \pi'_{dyn} + \pi'_B$ from dynamic terms $(\pi'_{dyn})$ and from the buoyancy term $(\pi'_B)$ were examined and it was found that two different mechanisms lead to the low-level convergence at the right and left flank gust front. The strong convergence on the left flank is forced mainly by the high pressure due to the cold pool spreading against an inflowing stream of environmental air. While $\pi'_B$ is the dominant contribution to pressure forcing on the left flank of the storm system, the convergence is generated by the dynamic interaction $(\pi'_{dyn})$ of the storm with the environmental wind shear on the right flank. This interaction leads to a lowered pressure which enhances the horizontal convergence of warm environmental air into the updraught. Thus, even though the low-level convergence is smaller on the right flank than on the left flank (see Fig. 4.3b), the right flank storm can exist if the wind shear is large enough so that a strong mesolow[2] is generated. For example, for $U_s = 25$ m s$^{-1}$, the Colon storm splits, but the right flank cell decays after about 60 min (not shown). However, when the wind shear is increased to $U_s = 35$ m s$^{-1}$, the Colon right flank cell is steady and survives the model time of 120 min.

## 4.2.4 Wind shear vector turns through 90°

In the next chapter, the influence of a sea breeze on convective development will be studied. The environmental winds at mid-levels are easterly, while the northerly sea breeze produces strong shear below $z = 2$ km. Thus, the wind profile in the sea breeze experiments is characterised by a shear vector which turns through 90° below $z = 2$ km. To provide a connection between the curved hodograph experiments presented in this chapter and those presented in the following chapter, some of the curved hodograph experiments (mid14, Davg) are rerun with a shear vector turning through 90°, instead of 180°. With a shear layer depth of 5 km, the initial updraught characteristics in the 90° cases are similar and the splitting behaviour is the same as in the 180° experiments. When the shear layer depth is decreased to 2 km, splitting with intensification occurs for larger values of shear, as found in section 3.4.3. However, the main finding that a larger vertical wind shear is required to split tropical storms than mid-latitude storms is confirmed.

---

[2]A mesolow is a mesoscale low-pressure centre.

## 4.3   Summary

The influence of directional wind shear on tropical and mid-latitude convection has been studied using Bryan's cloud model. Thunderstorms were initialised in a mid-latitude and two tropical environments where the shear vector turns clockwise with height; the amount of vertical wind shear was varied by altering the parameter $U_s$. The model results were compared to those in WK84 and GSR04 and with those of the straight-line hodograph simulations described in chapter 3. The principal findings are as follows:

- The initial updraughts are stronger, on average, when the hodograph is curved rather than straight-line. The reason for the stronger updraughts in environments with a veering shear vector than in uni-directionally sheared environments is the stronger vertical pressure gradient which forces significant updraught growth on one flank of the storm system.

- While the generation of the left and right flank cells in the mid-latitude experiments occurs for wind shears $U_s \gtrsim 15 \text{ m s}^{-1}$, the shear needs to be larger than $U_s \gtrsim 25 \text{ m s}^{-1}$ for splitting with subsequent evolution of the left and right flank cells to occur in the tropical experiments. This result is consistent with that found in the uni-directional shear experiments, where a larger $U_s$ was required to produce split storms in the tropics than in the mid-latitudes.

- As for the uni-directional shear cases, it was found also for the curved hodograph experiments that the tropical thunderstorms contain a larger amount of ice and water within the updraught than those in the mid-latitudes. This results in a peak downdraught strength, $|w_{min}|$, in the tropical cases, which is up to 70% larger than in the mid-latitude cases. As described in chapter 3, a strong downdraught results in a strong gust front, which cuts off the warm inflow from the thunderstorm, leading to storm demise before the evolution of left and right flank cells is possible.

- After the splitting process, the resulting right flank storm possesses cyclonic rotation with the vortex centre close to the centre of the updraught. However, the left flank updraughts exhibit no preferred sense of rotation and show no significant correlation between the centre of the vortex and the centre of the updraught.

In general, the evolution and dynamics of the tropical thunderstorms was found to be the same as that of the mid-latitude thunderstorms, except that a larger vertical wind shear is required in the tropics to achieve left and right flank storms. As suggested in section 3.6, this finding can help to develop new diagnostic variables and parameters which are useful in forecasting mid-latitude and tropical thunderstorms.

# Chapter 5

# Sea breeze convection in a vertically sheared environment

In the previous two chapters, idealised simulations of tropical thunderstorms were performed to examine how vertical wind shear controls their evolution. Environmental influences on the thunderstorms such as orography, sea breezes, or the synoptic situation were thereby ignored. These highly idealised experiments helped to provide a deeper understanding of the conditions necessary for severe thunderstorms to form in the tropics.

In this chapter, a slightly more realistic, but still idealised, modelling study is presented, discussing the influence of sea breezes on thunderstorm evolution in an environment with directional wind shear. This study is motivated by the non-severe and severe "Northeasters" which are multicell thunderstorm complexes that affect the coastal city of Darwin in northern Australia, approaching from the northeast. It is believed that sea breezes play an important role in the evolution of these thunderstorm systems. From observations and previous studies it is known that sea and land breezes are important as initiation mechanisms for convection, and that interactions between existing storms and these local circulations can generate new thunderstorms (*e.g.*, Keenan and Carbone 1992, Wilson and Schreiber 1986, Rao and Fuelberg 2000). In the first section of this chapter, a Northeaster which occurred on 14 November 2005 is described. The model configuration used to simulate this Northeaster is specified in section 5.2, and the basic experiment is presented in section 5.3. Changes to this experiment are discussed and analysed in sections 5.4 and 5.5, with the focus lying on the investigation of possible mechanisms for post-sea breeze convection. A non-severe Northeaster which occurred on 7 February 2006 is examined in section 5.6, and a summary will be given in the last section.

## 5.1   Severe Northeaster on 14 November 2005

During the afternoon of 14 November 2005, a thunderstorm passed over Darwin from the northeast. The automatic weather station at the airport was hit by lightning and stopped recording during the storm. However, prior to this outage, 25 mm of rain were recorded between 9 am and 3 pm local time, most from the start of the thunderstorm. Trees were uprooted or snapped (see Fig. 5.1) along a 1 km stretch of a highway adjacent to the airport, and the outward bound section of the highway was blocked. Power supplies to many residents were disrupted for up to an hour.

Figure 5.1:  Photographs of damage due to a Northeaster which occurred on 14 November 2005 in the Darwin area. Courtesy of Michael Foley.

A sequence of radar images from the Berrimah radar, located to the east of Darwin, is shown in Figs. 5.2a to 5.2d. An explanation of the evolution of the storm system is given in section 5.3, where it is compared to the model output of the basic experiment. Most of the information about this event is taken from the Severe Thunderstorm report of the Australian Bureau of Meteorology Regional Forecasting Centre in Darwin.

For the forecasters in Darwin, the storm system was hard to classify as it first lacked "organisation", but in the end it showed alignment, as it is typical for squall lines (see section 1.1). In an analysis of storm systems in the Darwin region, the event of 14 November 2005 is, indeed, classified as a "squall line" (Todd Smith, personal communication). However, due to the lack of obvious structure of the storm system, it will be referred to here as a "multicell complex".

## 5.2   Model configuration

The Northeaster of 14 November 2005 (YYMMDD = 051114), and the circumstances which led to the formation of such a strong multicell complex are studied here using Bryan's cloud model with ice microphysics included. Convection is initialised in an environment with the wind profile and the vertical temperature and moisture profiles from the 051114-0000 UTC Darwin sounding (see Fig. 5.3). To represent the mid-afternoon conditions when the Northeaster developed, the lowest 1 km of the sounding is modified to give a convectively-mixed boundary layer where $\theta_0 = 306.75$ K, and $q_{v0} = 19.34$ g kg$^{-1}$ (see Fig. 5.3, blue solid lines). The values for $\theta_0$ and $q_{v0}$ are chosen to coincide with the data recorded in one minute intervals at Darwin airport. The calculated CAPE[1] based on these values is 4129 J kg$^{-1}$, which is 18.5% lower than the modified CAPE calculated by the Darwin Bureau of Meteorology (5069 J kg$^{-1}$). It is difficult to determine the precise reason for the different value of CAPE obtained by the Bureau of Meteorology, but I have confidence in the accuracy of my value as the algorithm has been checked against that of a prominent

---

[1]CAPE is calculated here using pseudoadiabatic processes and Bolton's formula [Eq. (43) in Bolton 1980] for equivalent potential temperature.
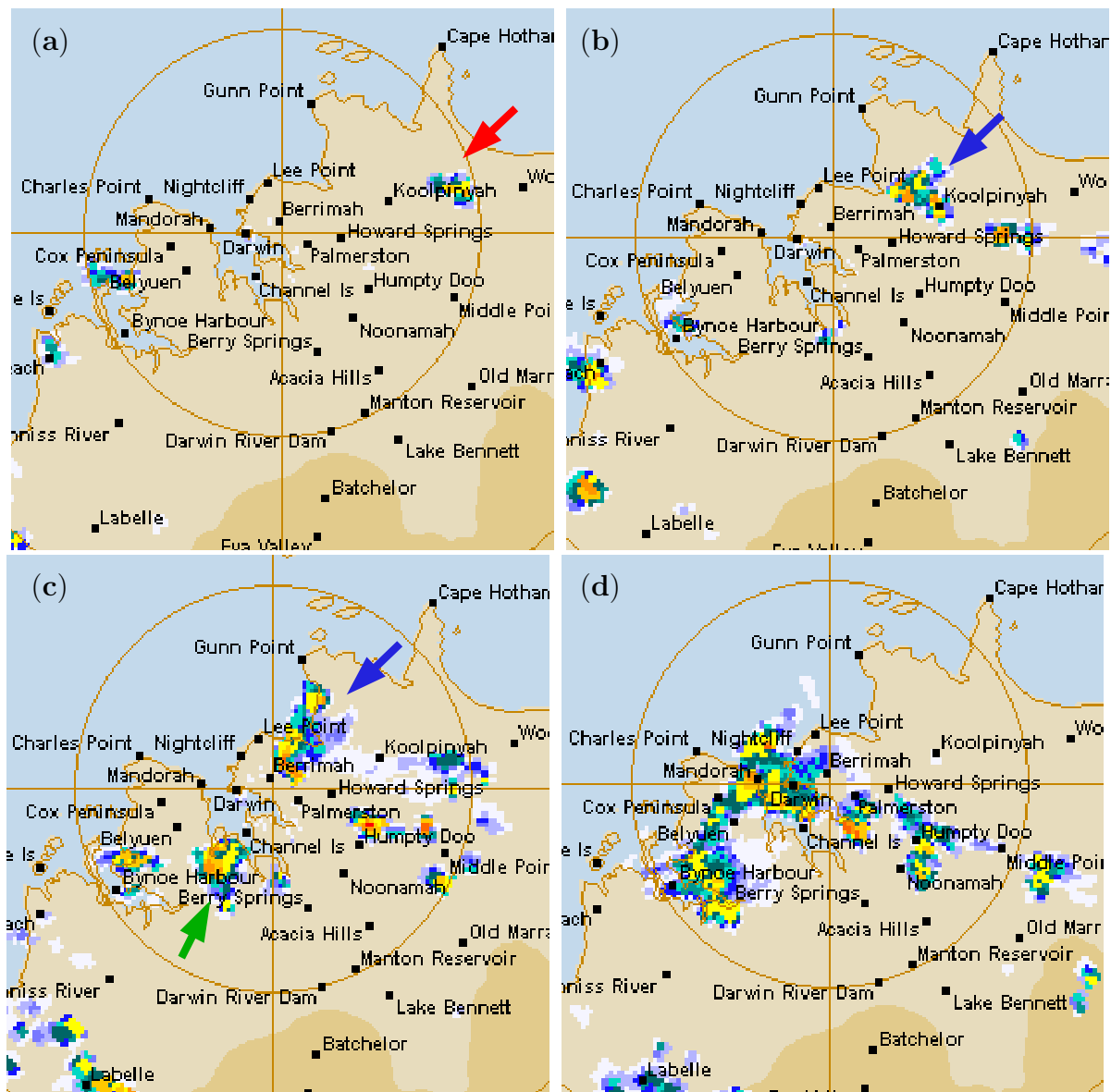
Figure 5.2: Berrimah radar images at (a) 0318 UTC, (b) 0358 UTC, (c) 0438 UTC, and (d) 0518 UTC on 14 November 2005, showing the evolution of the Northeaster. Colours represent the rain rate, whereby white and blue stands for light, green and yellow for moderate, and red for heavy rain. The circle has a radius of 50 km. The red arrow in panel (a) points to the initial updraught, which developed into a multicell complex at later stages [blue arrows in (b) and (c)]. The green arrow in panel (c) points at a second storm system which formed south of Channel Island. Courtesy of the Australian Bureau of Meteorology Regional Forecasting Centre in Darwin.
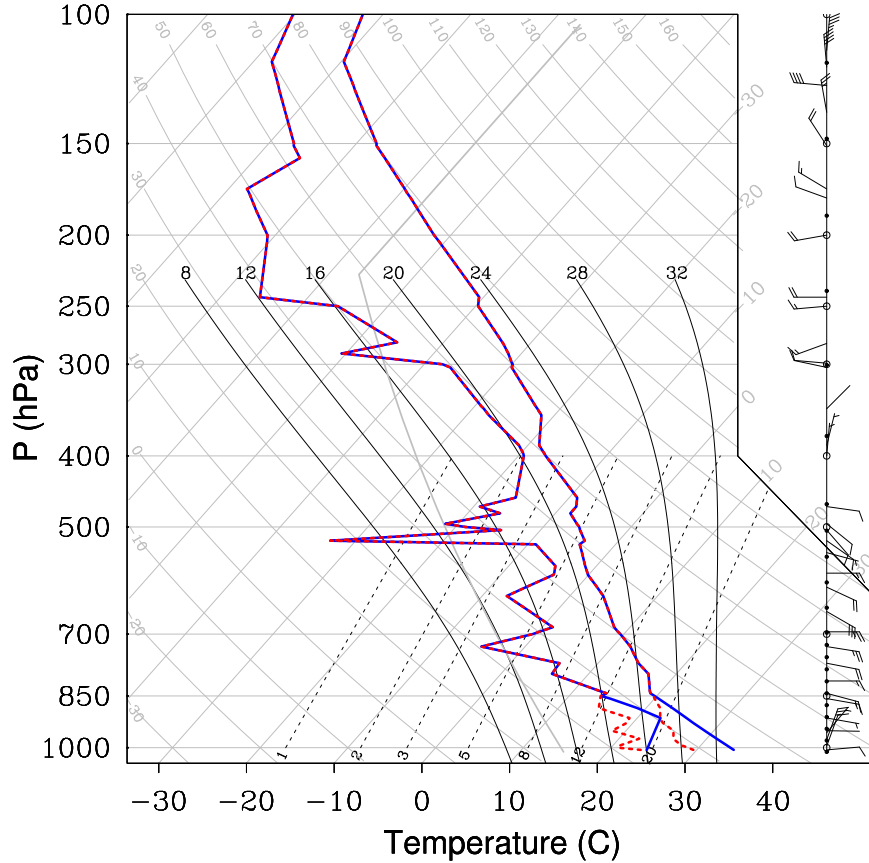
Figure 5.3: Skew$T$-log$p$ diagram showing the temperature and dew-point temperature of the 14 November 2005, 0000 UTC sounding as used in the simulations (blue, solid lines) and unmodified (red, dashed lines). Every second wind barb is plotted on the right, pointing in the direction from which the wind is blowing.

scientist in the field. One general problem with calculating a modified CAPE is that a small difference in the surface dew point temperature can result in a large difference in CAPE (*e.g.*, Mapes and Houze 1992, Chappel 2001). The values of $\theta_0$ and $q_{v0}$ taken here may be slightly different to those used by the Bureau of Meteorology, which results in differrent values of CAPE.

The model domain size is defined as $(90 \times 60 \times 28)$ km$^3$, with a horizontal grid spacing of 1 km, and a vertical grid, stretched from 120 m at the bottom of the domain to 1 km at the top. This stretching scheme improves the numerical resolution near the surface, where it is most needed. Convection is triggered by a 8 km wide, 1 km deep, and 2 K warm bubble which is initialised 10 min after model initialisation.

A number of experiments are performed with a combination of a northerly sea breeze (Nsb), a westerly sea breeze (Wsb), and/or a northwesterly sea breeze (NWsb). Each sea breeze is initialised using a box of cold air in the north, west, and northwest of the domain at the beginning of the simulation, respectively. The potential temperature of a Nsb, with its front located at $y = y_{north}$, for example, is given by

$$\theta = \theta_{sb} \frac{z_{sb} - z}{z_{sb}} \qquad \text{for } y > y_{north}, \text{ and } z < z_{sb}, \tag{5.1}$$

where $\theta_{sb}$ is the temperature excess, and $z_{sb}$ the depth of the cold box. Values of $z_{sb} = 2$ km, and $\theta_{sb} = -2$ K are chosen, based on observations of sea breezes in the Darwin region (Todd Smith, Darwin Regional Forecasting Centre, personal communication; May *et al.* 2002). Each experiment is run for 180 minutes, thus allowing the initial updraught and the subsequent storm system enough time to develop.

# 5.3 Northerly and northwesterly sea breeze – the basic experiment

To create environmental conditions similar to those on 14 November 2005, the model is initialised with two cold boxes representing the Nsb and NWsb. A warm bubble is placed above the Nsb front[2] so that the first updraught develops directly above, to simulate convection triggered by the Nsb. This model run will be referred to below as the "basic experiment".

## 5.3.1 Initial cell

Horizontal cross-sections through the initial cell[3] and the subsequent storm system at mid-levels (upper panels) and low-levels (lower panels) are shown in Figs. 5.4 to 5.6, for $t = 30, 50, 70, 90, 110$, and $130$ min. The sea breeze fronts are depicted by thick red lines, while the gust front is marked by the thick black contour. Regions of ascent are shaded in yellow and orange, while regions of downdraught are shaded in green and blue. The model output illustrated in these figures, will be compared with the radar pictures from 14 November 2005 and with the Severe Thunderstorm report.

On 14 November 2005, 0100 UTC, the Nsb along the north coast, and the Wsb along the west coast began to move inland. At 0130 UTC, the NWsb began along the Nightcliff Lee Point coastline, and moved over Darwin airport. With the onset of the seabreeze at the Darwin airport, the modified CAPE was calculated by the Darwin Regional Forecasting Centre to be 5069 J kg$^{-1}$. The first cell formed on the Nsb front at 0310 UTC (Fig. 5.2a, red arrow). These conditions were created "artificially" in the model as described above. The cloud water mixing ratio at $z = 4.6$ km of the modelled cell becomes larger than 0.1 g kg$^{-1}$ after 30 min, and the maximum updraught speed of 28 m s$^{-1}$ is reached after 48 min. Thus, 0310 UTC corresponds to a model time of about 30 min. The updraught which is located above the Nsb front, can be seen in Fig. 5.4a. At 30 min the horizontal low-level convergence (blue solid lines in Fig. 5.4c) is large, due to the rising buoyant air.

The radar pictures (Figs. 5.2a and b) reveal that the initial cell progressed to the west, along the sea breeze boundary, with a speed of about 9.4 m s$^{-1}$. At 0350 UTC, the cell met the NWsb and collapsed, creating a spreading gust front. The westward movement of the modelled cell is apparent by comparing Figs. 5.4a and 5.4c, however, the propagation speed is 43% smaller than that observed. The cell moves towards the west due to the environmental easterly winds at low- and mid-levels. The gust front in the model forms at 42 min and leads to large convergence (blue solid lines in Fig. 5.4d) at the northern and southwestern edges, ahead of the cold pool. The modelled updraught decays after about 60

---

[2]The sea breeze front is defined as the leading edge of the advancing cool air.

[3]The terms "cell" and "updraught" are used here as synonyms and represent convection in the form of a single updraught.

min of integration, once it becomes cut off from the warm and moist environmental inflow by the expanding gust front. The lifetime of this cell is similar to that of the observed cell of 051114. However, the Severe Thunderstorm report notes that the cell decayed upon interaction with the NWsb, although this conclusion is not easy to verify from the available observations.

In the observations, new cells developed on the gust front of the initial updraught, parallel to, but behind the Nsb (see radar image Fig. 5.2c). In the model, convective development starts at the NW edge of the gust front after 66 min, and the first new updraught is apparent in Fig. 5.5a. Figure 5.5b shows that at this time, the surface convergence ahead of the cold pool is large in the region where the first cell is triggered. New cell development in the model occurs behind the sea breeze front as observed in the radar images. At 90 min after model initialisation, three new cells are present (see Fig. 5.5c).

## 5.3.2 Multicell development

According to the Severe Thunderstorm report, the system had developed into a multicell complex at 0420 UTC, which is apparent in Fig. 5.2c (blue arrow). Further, a new cell developed on the westerly seabreeze front, about 7 km south of Channel Island (see Fig. 5.2c, green arrow). 0420 UTC corresponds to a model time of about 100 min. At this time the whole system in the model can be called a multicell complex – see Figs. 5.5c and 5.6a. A multicell complex is defined here as a system of at least two updraughts with vertical velocities exceeding 5 m s$^{-1}$ at any stage of their life cycle, and with the distance between neighboring updraughts being less than 10 km. The focus of this experiment is to study the evolution of the initial updraught and the subsequent formation of the multicell complex. No cell, such as that south of Channel Island, is observed in the model as no further mechanism (second warm bubble) was used to trigger a new updraught far SW of the pre-existing complex.

Here, an extract from the Severe Thunderstorm report, which illustrates the difficulty of classifying the storm system at this time: "Given the convective analysis's outcome of moderate potential for severe convective wind gusts, the forecast strategy/thinking at this stage was that we were still waiting for convection to become "organised", and then to find evidence of severity. Generally, "organised" usually means the storms form some sort of line, typically oriented perpendicular to the steering flow (*i.e.*, squall lines), although it is a grey area. Convection was multicellular, with little organisation to it. Gusts were coming out of the southern and northern flanks of the system, which could have even indicated a dissipating trend. Knowing that storms from the northeast tend to have severe characteristics, we were leaning towards accepting the convection as being organised, however, we were still looking for signs/evidence of severity."

The observed multicell complex propagated towards the WNW, at a speed of approximately 40 km h$^{-1}$. New cells were generated along the southern flank of the system gust front, and the complex became aligned NNE/SSW (see Fig. 5.2d). The modelled multicell complex moves also towards the WNW with a speed of about 39 km h$^{-1}$. New cells develop along the gust front, south of the modelled multicell complex, leading to an alignment of the individual cells from NNE to SSW (see Figs. 5.6a and c). Thus, the line of convection is oriented perpendicular to the low-level shear vector. The latter characteristic was found also in observational studies by Keenan and Carbone (1991), where this orientation
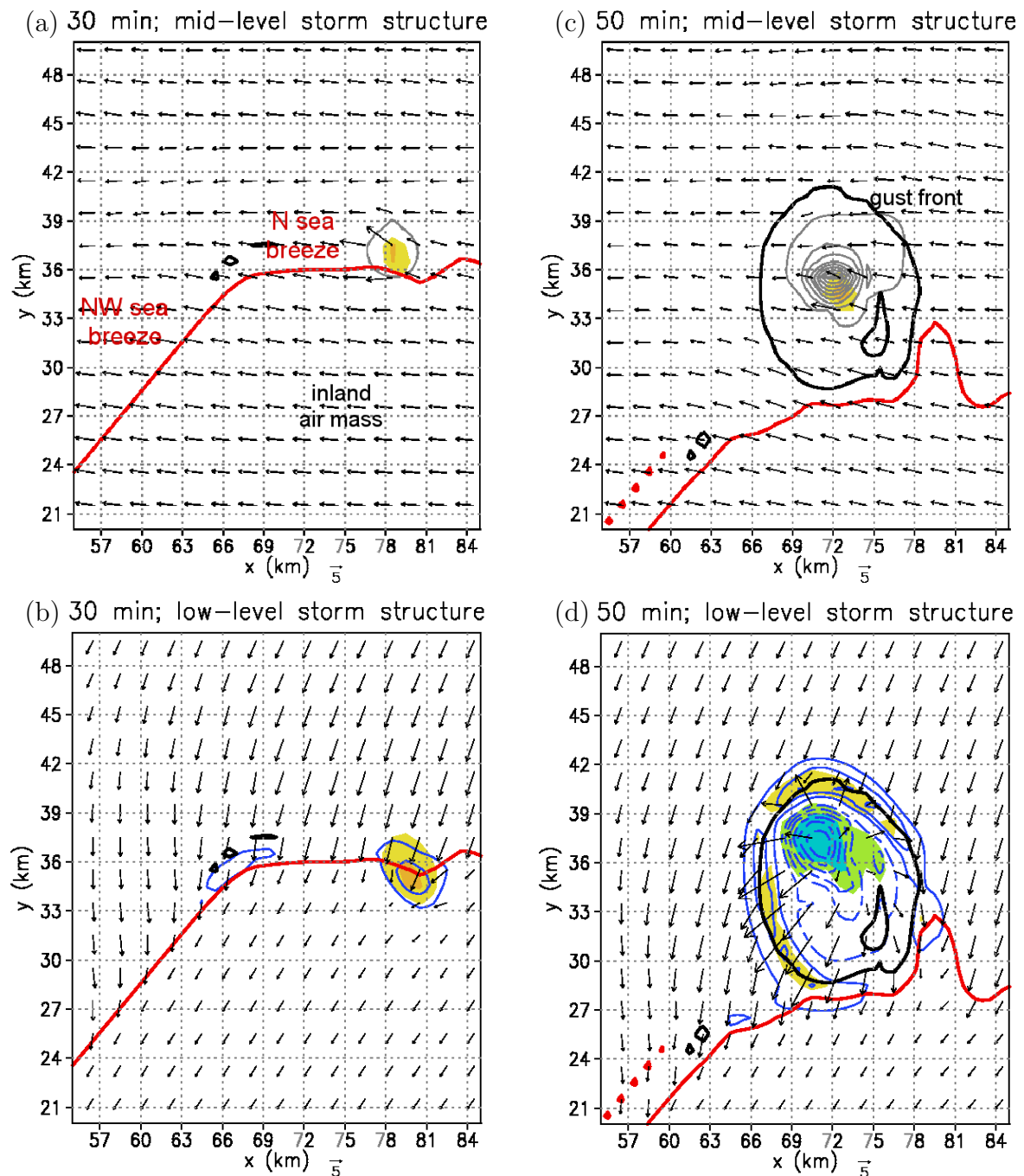
Figure 5.4: Mid-level and low-level storm structure depicted at $t = 30$ and 50 min. The sea breeze fronts and the gust front are denoted by the thick red and black lines, respectively, and represent the $-0.5$ K temperature perturbation contour. Upper panels: Vectors represent horizontal flow at $z = 4.6$ km, and the total precipitation mixing ratio $q_n = q_r + q_s + q_g$ is contoured in grey at 2 g kg$^{-1}$ intervals, with the zero contour omitted. Regions of updraught velocities at $z = 4.6$ km larger than 5 m s$^{-1}$ and 10 m s$^{-1}$ are shaded in yellow and orange, respectively. For the explanation of the lower panels, see Fig. 5.5.
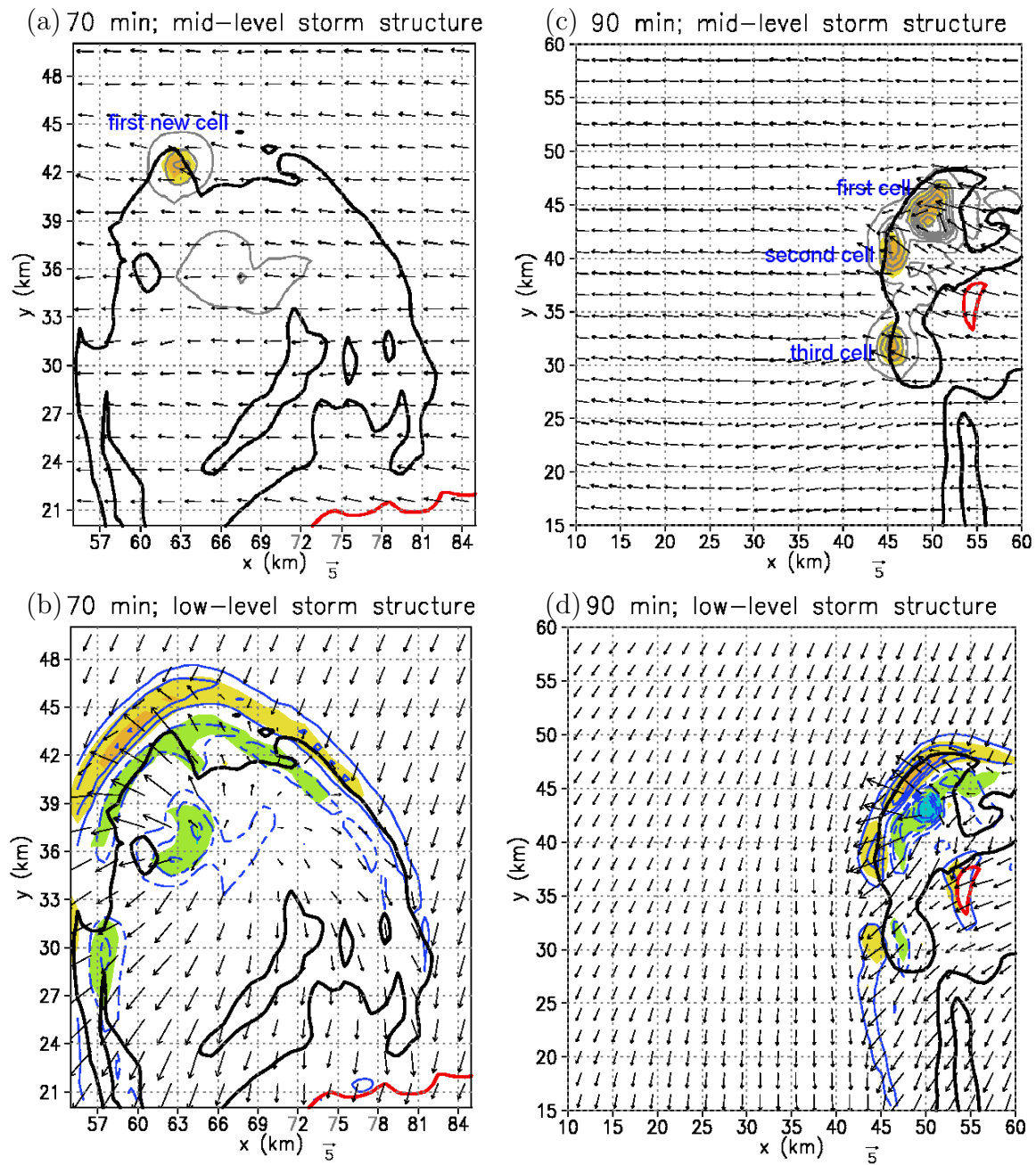
Figure 5.5:   Same as in Fig. 5.4, but for $t = 70$ and 90 min. Lower panels: Vectors represent the horizontal flow at the surface, and the surface divergence and convergence are contoured (dashed/solid) in blue at $2 \times 10^{-3}$ s$^{-1}$ intervals, with the zero contour omitted.   Regions of updraught velocities at $z = 1.1$ km larger than 2 m s$^{-1}$ and 5 m s$^{-1}$ are shaded in yellow and orange, while regions of downdraught $< -2$ m s$^{-1}$ and $< -5$ m s$^{-1}$ are shaded in green and light blue, respectively.   Note that a larger section of the domain is depicted for $t = 90$ min than for $t = 70$ min.
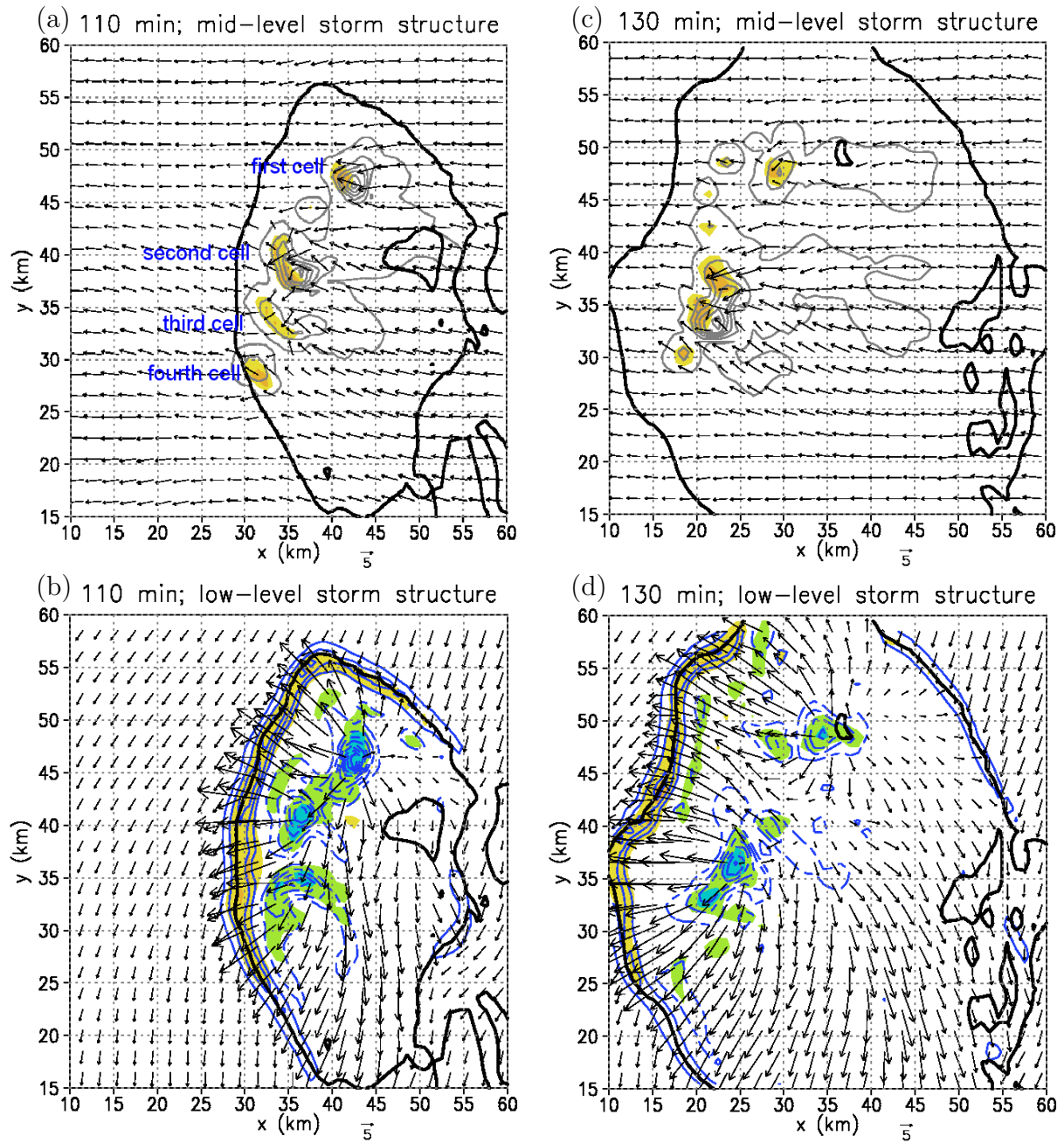
Figure 5.6:   Same as in Figs. 5.4 and 5.5, but for $t = 110$ and $130$ min.

was observed consistently with all types of convection (monsoonal system convection, sea breeze convection, squall lines).

The length of the line in the Severe Thunderstorm report is specified as $\approx 65$ km, but, the modelled multicell complex spans only about 25 to 30 km. However, the radar pictures of 051114 reveal, that at 0510 UTC, the "real" multicell complex, which grew at the gust front of the initial cell, spans $\approx 30$ km also. The "line" mentioned in the Severe Thunderstorm report contains the multicell complex and the system which developed along the Wsb near Channel Island (see Figs. 5.2c and d). The close proximity of these two systems results in one line having a total size of up to 65 km. However, the Channel Island thunderstorm complex is not included in the simulations.

The basic experiment shows that, with a single warm bubble and two sea breezes that are initialised at the right time and position, a multicell complex with similar characteristics to that of 14 November 2005, can be simulated. The model output compares well with reality in the following respects:

- The initial cell progresses to the west

- New cells develop on the gust front of the initial cell, forming a multicell complex

- New cells develop behind the sea breeze front

- New cell development along the southern flank of the multicell complex

- Propagation speed and direction of the multicell complex (40 km h$^{-1}$, WNW)

- Orientation of the multicell complex (NNE/SSW)

- Length of the line of convection (25 km to 30 km)

The single particular difference between the model output and the observed development is that the initial cell progresses slower to the west than the real cell. Such discrepancies may arise due to the different CAPE values (4129 J kg$^{-1}$ versus 5069 J kg$^{-1}$), or because the initial cell needs to be triggered by a warm bubble in the model.

In sections 5.4 and 5.5, the changes to the basic experiment will be conducted and the results discussed in order to examine the importance of the initial components (*e.g.*, sea breeze(s), warm bubble) in the model.

| EXP | basic | $b_{kess}$ | 1 | 2 | 3 | 4 | 5 | 6 | 7.1 | 7.2 | 7.3 |
|---|---|---|---|---|---|---|---|---|---|---|---|
| NWsb | × | × | | | × | | × | × | × | × | × |
| Nsb | × | × | | × | | × | × | × | × | × | × |
| Wsb | | | | | | × | | | | | |
| Wind | 00 UTC | 00 UTC | 00 UTC | 00 UTC | 00 UTC | 00 UTC | 00 UTC | 00 UTC | $u=0=v$ | $u=-5$ | $v=-5$ |
| Warm bubble $(x,y)$ | (85,38) | (85,38) | (85,38) | (85,38) | (85,38) | (85,38) | (85,**28**) | (85,**48**) | (75,42) | (85,43) | (75,41) |
| $t$ when $q_c > 0.1$ g kg$^{-1}$ | 30 | 30 | 30 | 30 | 30 | 30 | 30 | 24 | 26 | 26 | 26 |
| $w_{max}$ (m s$^{-1}$) | 28.0 | 25.6 | 24.0 | 27.8 | 23.4 | 28.5 | 24.4 | 26.5 | 45.5 | 46.8 | 49.9 |
| $t_{wmax}$ (min) | 48 | 36 | 38 | 38 | 38 | 48 | 38 | 30 | 34 | 32 | 34 |
| $w_{min}^{cb}$ (m s$^{-1}$) | -15.0 | -11.4 | -12.7 | -14.97 | -13.0 | -14.8 | -13.1 | -12.2 | -17.9 | -17.1 | -14.6 |
| $t_{wmin}^{cb}$ (min) | 44 | 42 | 46 | 44 | 44 | 44 | 44 | 38 | 44 | 42 | 46 |
| $\overline{w_{min}^{cb}}$ (m s$^{-1}$) | -10.2 | -9.2 | -8.4 | -10.2 | -9.2 | -10.0 | -9.8 | -7.7 | -10.6 | -10.9 | -11.4 |
| $max(q_n)$ (g kg$^{-1}$) | 17.5 | 14.1 | 11.6 | 16.5 | 11.5 | 18.2 | 12.0 | 13.0 | 22.8 | 20.7 | 21.1 |
| $t_{gf}$ (min) | 42 | 42 | 42 | 42 | 42 | 42 | 42 | 36 | 42 | 40 | 40 |
| $\overline{\partial u/\partial x + \partial v/\partial y}$ ($10^{-3}$ s$^{-1}$) | -7.17 | -6.93 | -5.54 | -6.93 | -7.05 | -7.13 | -7.76 | -5.44 | -5.04 | -5.23 | -4.62 |
| $t$ of decay ($q_c < 0.1$ g kg$^{-1}$) | 60 | 60 | 72 | 60 | 60 | 60 | 60 | 56 | 52 | 44 | 46 |
| $1^{st}$ new cell | 66 | 64 | - | 72 | 66 | 66 | 62 | - | - | - | - |
| $2^{nd}$ new cell | 72 | 68 | - | 76 | 76 | 68 | 72 | - | - | - | - |
| $3^{rd}$ new cell | 76 | 68 | - | 134 | - | 72 | 72 | - | - | - | - |
| $4^{th}$ new cell | 84 | 78 | - | - | - | 86 | 74 | - | - | - | - |
| $5^{th}$ new cell | 104 | 112 | - | - | - | 94 | 92 | - | - | - | - |
| $6^{th}$ new cell | 128 | 118 | - | - | - | 106 | - | - | - | - | - |
| Multicell complex | large | large | no | small | small | large | large | no | no | no | no |

Table 5.1: Settings and model output of the different experiments. The location where the warm bubble is initialised is given by $(x, y)$ in km. The time, $t$, at which the cloud water mixing ratio, $q_c$, of the initial updraught at $z = 4.7$ km becomes larger or smaller than 0.1 g kg$^{-1}$ ($\equiv$ time of decay) is given. $w_{max}$ refers to the maximum vertical velocity of the initial updraught, which is reached at the time $t_{wmax}$, while $w_{min}^{cb}$ is the peak minimum vertical velocity at cloud base ($z = 1.3$ km) reached at $t_{wmin}^{cb}$. $\overline{w_{min}^{cb}}$ is the average vertical velocity at cloud base between $t = t_{gf}$ and $t = t_{gf} + 20$ min. The maximum in the hydrometeors mixing ratio $q_n = q_c + q_r + q_i + q_s + q_g$ of the initial updraught is denoted by $max(q_n)$. $t_{gf}$ stands for the time of gust front occurrence of the initial updraught. The average convergence at low-levels, $\overline{\partial u/\partial x + \partial v/\partial y}$, is calculated between $t = t_{gf} + 12$ min and $t = t_{gf} + 20$ min. A new updraught is counted as a new cell if its updraught speed becomes larger than 5 m s$^{-1}$. The times (in min) at which the new cells occur are listed. Note that in all experiments a (8 km – 1 km – 2 K) warm bubble is used, except in EXP6 where a temperature excess of 6 K is necessary to trigger convection.

# 5.4    Sensitivity experiments

The role of the two sea breezes in the evolution of the multicell complex on 14 November 2005 is studied by modifying the basic experiment. A total of seven sensitivity experiments is considered here. Four experiments investigate the importance of the sea breezes: no sea breezes (EXP1); only a northerly sea breeze (EXP2), only a northwesterly sea breeze (EXP3); the northwesterly sea breeze replaced by a westerly sea breeze (EXP4). Two experiments use the basic experiment with the position of the initial convection changed: convection is triggered ahead of the northerly sea breeze (EXP5); and convection is triggered behind the northerly sea breeze (EXP6). The basic experiment, initialised with different idealised wind profiles, is used in EXP7 and examined for the most part in section 5.5.4. The experiments with the corresponding settings and outcome are listed in Table 5.1. In all experiments, the calculated CAPE ahead of the sea breeze(s) is 4129 J kg$^{-1}$, and 3517 J kg$^{-1}$ behind the sea breeze fronts. Thus, the environmental profile instability is the same in all cases.

It should be possible to answer the following questions by comparing EXPs 1 to 7 with the basic experiment:

- Does the orientation of the sea breeze(s) and the location of the initial cell relative to the sea breeze front have an influence on the characteristics of the initial updraught (strength $w_{max}$, evolution with time)?

- How are the downdraught and the gust front influenced in the different experiments?

- Is there new cell development on the gust front of the initial updraught, and

- Under which conditions does a large multicell complex with more than 3 or 4 new cells form?

In the following sections, the focus will be laid on describing the differences in the model settings and the major differences between the outcome of EXPs 1 to 7 and the basic experiment, while in section 5.5 the model results will be compared in more detail.

### No sea breeze – EXP1

In the first experiment, both sea breezes (NWsb, Nsb) are omitted. Then, the initial updraught develops in the absence of lifting supplied by a density current. The lack of lifting is demonstrated as the strength of the initial updraught in EXP1 is about 14% smaller than that in the basic experiment. As the downdraught develops, the vertical velocity at cloud base decreases significantly and a cold pool forms below the cloud after 42 min. In contrast to the basic experiment, where the gust front occurs behind the sea breeze fronts, the cold pool in EXP1 spreads out in an undisturbed environment. In the basic model run, more than 6 cells form at the gust front, while no new cell development occurs in EXP1. The main reason for the latter is the lack of large horizontal convergence at the leading edge of the cold pool (see section 5.5). Thus, the environmental winds of 14 November 2005, alone, would not have been sufficient for a multicell complex to form on this day. This suggests that one or more sea breezes are necessary to create an environment suitable for new cell development on a pre-existing density current.

**Northerly sea breeze, only – EXP2**

While the basic experiment is initialised with a Nsb and a NWsb, the latter is omitted in EXP2. However, the strength and evolution of the initial cell is very similar to that in the basic model run (see Table 5.1). The initial updraught in EXP2 reaches its peak of intensity $w_{max} = 27.8$ m s$^{-1}$ after 38 minutes. Shortly before, the downdraught occurs, an event that is apparent in a rapid decrease of the vertical velocity minimum at cloud base. This minimum in $w$ correlates with local maxima in the surface wind speed and surface divergence underneath the cell. The spreading cold outflow is associated with maxima of the horizontal vorticity components at the surface. After about 54 min, the strongest divergence is found behind the NW edge of the gust front, and the largest convergence is found just "opposite", *i.e.*, ahead of the gust front. With the weakening initial updraught and downdraught, the surface divergence, as well as the low-level horizontal vorticity weaken. After about 72 minutes, the first new cell develops at the NW edge of the cold pool of the initial updraught. Four minutes later, a second new cell grows close to the first one – even though the gust front is weak at this stage. The new cells in EXP2 intensify, but never reach the maximum vertical velocity of the initial updraught due to the weak gust front.

Altogether, only three new cells develop on the gust front in EXP2. Such a system will be called a "small multicell complex" below, due to the small amount of new cells which formed. However, in the basic experiment more than 6 new cells developed, and this system is classified as "large". The comparison of both experiments reveals that a) the initial updraught in the basic experiment is not significantly influenced by the NWsb, because the latter is too far away from the initial cell at the time it develops; b) under the given conditions (CAPE, wind profile) the influence of a Nsb alone can lead to the development of new cells at the pre-existing gust front; c) a NWsb (together with a Nsb) seems to be necessary for a large multicell complex to form.

**Northwesterly sea breeze, only – EXP3**

In the third experiment, the Nsb is omitted so that the effect of a NWsb on the overall evolution of the system can be studied. As in EXP1, the absence of the Nsb in EXP3 leads to a weaker initial cell than in the basic experiment. However, the gust front occurs at the same time in all model runs and convergence is largest ahead of the NW edge of the gust front at 66 min, leading to new cell development. Six minutes after the formation of the first new cell, a weaker second cell grows SW of it. Both cells decay after about 144 minutes. EXP3 shows that a) due to the lack of the Nsb, no lifting is provided to the thermal and the resulting updraught is weaker, and b) the NWsb alone does not provide the conditions for a large and long-lived multicell complex to form.

**Northerly and westerly sea breeze – EXP4**

EXP4 is very similar to the basic experiment, with the only difference being that the NWsb is replaced by a Wsb, so that the sea breeze fronts are oriented perpendicular to each other. With a Wsb front located at $x_{Wsb} = 60$ km, the distance between the warm bubble centre and the front is about 25 km at the beginning of the experiment. The evolution of the initial updraught is similar to that in the basic model run. However, the first new cell develops on the western edge of the gust front and subsequently a second cell forms at the

NW edge. A large multicell complex with more than 6 cells develops and survives for the duration of the model time of 180 min.

Model runs with different positions of the Wsb front ($x_{Wsb}$) were computed. For example, if $x_{Wsb} = 10$ km, giving a distance to the thermal of about 75 km, only a small multicell complex develops. Thereby, the characteristics of the initial updraught and the subsequent new cell development are comparable to that in EXP2, where only a Nsb is included. Thus, in the presence of a Nsb, a Wsb has the effect of generating an appropriate environment for the development of a large multicell complex, but only if the Wsb front is not located too far away from the initial updraught and its gust front.

**Warm bubble placed ahead of the Nsb front – EXP5**

In EXP5, both sea breezes are included, but the warm bubble is placed 10 km further south than in the basic experiment. Thus, the convection develops ahead of the Nsb and NWsb. The evolution and characteristics of the initial updraught and its cold pool are very similar to that in EXP3. The gust front occurs at 42 min, and at the beginning it spreads out ahead of the sea breeze fronts. As the Nsb front propagates with a larger speed towards the south than the southern edge of the gust front, the cold pool is located entirely behind the sea breeze fronts after about 70 min. The new cell development at the gust front is comparable to that in the basic experiment. Up to 5 new cells are generated at the NW and northern edge of the cold pool, forming a large and long-lived multicell complex. Thus, whether or not the convection forms at the Nsb front or is triggered up to 10 km ahead of it, has an influence on the initial updraught strength, but does not make a significant difference in the evolution of the multicell complex.

**Warm bubble placed behind the Nsb front – EXP6**

The influence of a displacement of the initial cell behind the Nsb front on the overall system structure is examined in EXP6. In this case the warm bubble is initialised 10 km further north then in the basic experiment and lies within the cold sea breeze air at the initial time. However, the cool sea breeze environment does not allow convection to be triggered by a (8 km – 1 km – 2 K) thermal, and thus, the temperature excess $\Delta\theta$ is increased to either 4 K or 6 K. With $\Delta\theta = 6$ K, the strength of the resulting updraught is comparable to those in the other experiments, allowing a better comparison of the characteristics of the generated cold pool and the subsequent development. Note that the characteristics of the initial updraught ($w_{max}$, $q_n$, timing) in EXP6 should not be compared directly with those of the other experiments as they are sensitive to the warm bubble parameters chosen (see section 3.4.2). In EXP6, there is no new cell development on the gust front of the initial updraught, the reason for which will be discussed in section 5.5.

**Different wind profiles – EXP 7**

Experiment 7 (Nsb and NWsb) consists of different model runs, where the environmental wind velocity is either kept constant with height (EXPs 7.1 to 7.3), or where an idealised wind profile is used (see section 5.5.4) instead of the 0000 UTC wind profile, as shown in Fig. 5.3. In EXP7.1, no environmental wind is included in the model ($u = 0 = v$), while in EXP7.2 the wind is easterly with $u = -5$ m s$^{-1}$, and in EXP7.3 the wind is northerly with $v = -5$ m s$^{-1}$. Due the smaller environmental wind speeds and the lack of wind shear, the

strength of the initial updraught and downdraught is much larger in EXPs 7.1 – 7.3 than in all the other experiments (see Table 5.1). However, no multicell complex is generated in any of these three calculations. Nevertheless, new cell development occurs in EXPs 7.4 – 7.6, where the wind profile is given by Eq. (5.2).

**Microphysics scheme**

The Northeaster experiments are generally computed with Bryan's model using ice microphysics. The sensitivity of the model results to the microphysics scheme used is studied by repeating the basic experiment, but using the Kessler scheme ($b_{kess}$) instead of the LFO-scheme. The output of the basic experiment, run with and without ice is listed in Table 5.1 (first two columns). In general, the maximum updraught speed, $w_{max}$, in "$b_{kess}$" is smaller and the downdraught is weaker than that in the experiment with ice. This confirms the findings of section 3.3, where the stronger updraught in the experiment with ice is explained by the additional latent heat release during fusion and where colder low-level downdraughts resulted from the production of more precipitation and from the melting of hail/graupel. The time of gust front occurrence, $t_{gf}$, and the lifetime of the initial cell are the same in both experiments. In "$b_{kess}$", the evolution of the multicell complex, along with the new cell generation in the south of it, is similar to that in the basic experiment, although the times and locations at which the new cells occur are slightly different.

# 5.5 Comparison of the experiments and discussion

In the following sections, the experiments with the wind profile from the 0000 UTC sounding will be compared (basic experiment, EXP1 – EXP6). Experiments 7.1 to 7.6 will be discussed in detail in section 5.5.4.

## 5.5.1 Initial updraught

The comparison of the model outputs of EXPs 1 to 6 and the basic experiment reveals that the strength of the initial cell, $w_{max}$, depends on whether a sea breeze provides lifting to the updraught or not. Due to the reasons discussed above EXP6 is ignored first. Then, predominantly two types of curves of $w_{max}(t)$ are apparent in Fig. 5.7a ($t = 0 \dots 60$ min). Experiments 2, 4, and the basic experiment have a similar maximum updraught speed with $w_{max} \approx 28$ m s$^{-1}$, while the $w_{max}$ in EXP1, EXP3, and EXP5 are smaller (see Table 5.1). The latter "group" has in common that there is either no Nsb (EXP1, EXP3), or that the Nsb is located far away from the warm bubble (EXP5), while in the other experiments the Nsb lies in close proximity to the warm bubble. As the Nsb can provide additional lifting to the thermal, the updraughts in EXPs 2, 4 and the basic experiment are stronger than in EXPs 1, 3, and 5.

   This "grouping" is apparent also in the time-series of low-level horizontal convergence (see Fig. 5.7c), which is given by Eq. (4.3). Between $t = 18$ and 40 min, the low-level convergence is strongest at the location of the thermal, due to the vertical motion associated with it. Figure 5.7c shows that during this period, the amount of convergence is largest for the basic experiment and EXPs 2 and 4, and is smaller for EXPs 1, 3 and 5, where the Nsb does not exist, or is located far away from the thermal. Thus, the Nsb front increases the convergence at low-levels, resulting in an enhanced upward motion.
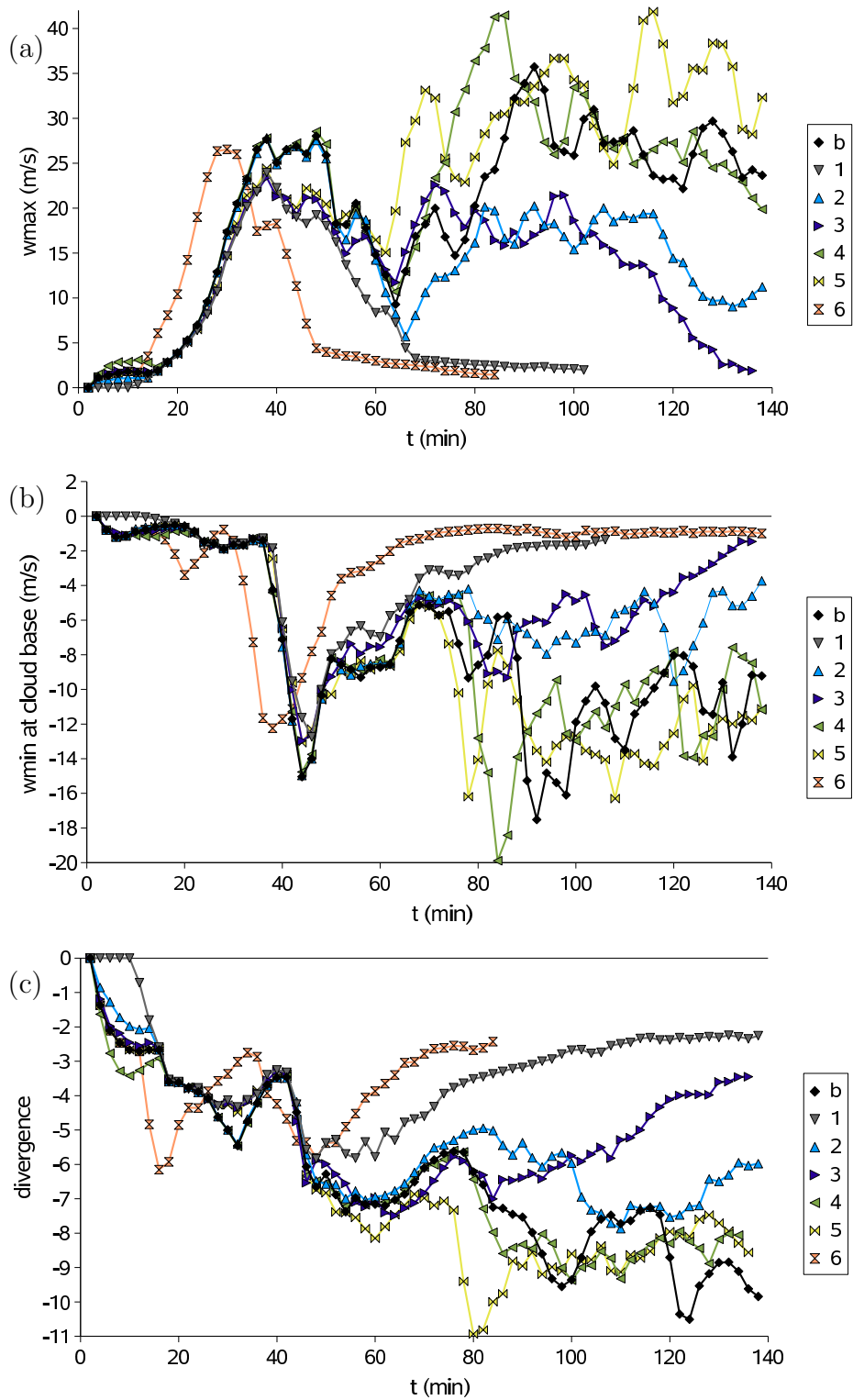
Figure 5.7: Time-series of the (a) maximum vertical velocity $w_{max}$, (b) the minimum vertical velocity at cloud base $w_{min}$ ($z = 1.3$ km), and (c) the minimum in horizontal divergence at $z = 190$ m (in $10^{-3}$ s$^{-1}$), measured over the whole horizontal extend of the domain. "b" stands for the basic experiment, while the numbers 1 to 6 stand for EXP1 to EXP6.

As apparent from Table 5.1, updraughts with large peak vertical velocities, $w_{max}$, show large maxima of hydrometeor mixing ratios, $max(q_n)$, also. It is found that the peak in $q_n = q_c + q_r + q_i + q_s + q_g$ occurs between $z = 4$ km and 5 km, whereby $q_g$ and $q_r$ provide the largest contributions to $max(q_n)$. Since updraughts counteract the fallout of hydrometeors, strong updraughts can hold more hydrometeors aloft in the cloud and give them more time to grow via collision and coalescence than weaker updraughts, a factor that explains the correlation between $w_{max}$ and $max(q_n)$.

### 5.5.2  Downdraught and gust front

Since the mid-tropospheric relative humidity and the wind profile are the same in EXPs 1 to 6 and the basic experiment, the effect of the entrainment of environmental air on the initial cells should be similar. Thus, differences in the downdraught strength are caused mainly by the different amounts of ice and water loading, $max(q_n)$, within the thunderstorms. The strength of the downdraught is represented by the minimum vertical velocity at cloud base ($z = 1.3$ km). Figure 5.7b shows how $w_{min}^{cb}$ changes within the domain with time. While the peak vertical velocities $w_{max}$ of the initial cells are reached at $t \approx 38$ min, the peak in $w_{min}^{cb}$ occurs about 6 min later. Since $w_{max}$ and the amount of ice and water loading, $max(q_n)$, are larger in the basic experiment and in EXPs 2 and 4, the corresponding downdraughts are stronger than in the other experiments. These strong downdraughts result in large gust front speeds shortly after the cold pool formed (not shown). Thus, the presence or absence of a Nsb front controls indirectly [via $w_{max}$, $max(q_n)$, $w_{min}^{cb}$] how strong the cold surface outflow of the initial cell will be immediately after the downdraught occurs. However, the updraught and downdraught strength of the initial cell are not directly an indicator for whether a large multicell complex will develop. For example, in EXP5 a large multicell complex forms, while in EXP2 (Nsb, only) just three new cells develop on the gust front – even though the downdraught and subsequent cold pool is stronger at the beginning than in EXP5.

### 5.5.3  Convergence and new cell development

The reason why the thunderstorm systems evolve differently in the experiments can be traced back to the problem of what triggers convection. The initiation of convection by density currents, *i.e.*, by gust fronts and sea breezes, is primarily a function of horizontal convergence.

In the experiments, the maximum low-level convergence[4] is found at different positions at the gust front edge shortly after the gust front occurs. However, twelve minutes after the gust front forms, the convergence is largest at the NW edge of the cold pool in all experiments, except in EXP6 where large convergence in the NW is apparent already after $t_{gf} + 8$ min (see Fig. 5.7c). This difference results from the faster overall evolution of the initial updraught and gust front in EXP6 compared to those in the other cases, which is caused by the larger temperature excess of the warm bubble that triggered convection. As the first new cells form about 20 min to 24 min after the gust front occurs, the mean convergence $\partial u / \partial x + \partial v / \partial y$ is calculated between $t = t_{gf} + 12$ min and $t = t_{gf} + 20$ min (see Table 5.1). This quantity should give information about how strong the low-level convergence

---

[4]If the word "convergence" is used in the following, low-level convergence ($z = 0.19$ km) is meant – if not stated otherwise.

needs to be so that new convection can be triggered at the pre-existing cold pool edge. The convergence is largest in the cases where a large multicell complex develops (EXP5, basic experiment, EXP4), followed by the experiments where small multicell complexes form (EXP3, EXP2), while the experiments in which no new cell development occurs show the smallest surface convergence (EXP1, EXP6). Thus, the amount of convergence at the gust front needs to be larger than about $6 \times 10^{-3}$ s$^{-1}$, on average, so that a new cell can be triggered. Thereby it is of great importance that strong convergence is present long enough time. If the convergence is large after the gust front appears, but decreases significantly some minutes later (see EXP1 and EXP6 in Fig. 5.7c), the upward motion declines – even before new cell development commenced.

The finding that strong convergence needs to be present over a sufficient time span is confirmed by observations. By studying the interaction of a SE-moving Darwin sea breeze front and a NW-moving gust front from a pre-existing thunderstorm, Keenan and Carbone (1992) noticed that a major storm did not develop until 25 minutes after the collision of the fronts. Then the new updraught formed 10 km downstream of the point of collision. The time lag between the collision of the fronts and the detection of the new cell was found also by Wilson and Schreiber (1986) who investigated mid-latitude convection at boundary-layer convergence lines. In their study, storms were initiated, on average, 18 min after a single front passed.

The reason for the different amounts of convergence at the cold pool edge in the experiments is, of course, related to the differences in the model settings. In three of the model runs with two sea breezes (basic experiment, EXP4, EXP5), the low-level wind in the cooler sea breeze environment creates a region of enhanced convergence when opposing the spreading gust front. Similar conditions are created by only one sea breeze (EXP2, EXP3), although, at later stages, the environment is less favourable for convection to form and the new cell development stops. In EXP1 (no sea breeze), the environmental winds of 14 November 2005 are not sufficient to provide an opposing flow to the spreading cold pool, which results in the demise of the initial cell and its gust front without triggering new updraughts. The question is why we do not see strong convergence and thus, new cell development in EXP6, even though there are two sea breezes creating the same environmental conditions as in the basic experiment. The answer lies in the characteristics of the gust front, which opposes the environmental flow. The strength of the cold pool is determined by the strength of the downdraught. A measure for the latter is calculated by averaging $w_{min}^{cb}$ between the time of gust front occurrence, $t_{gf}$, and $t_{gf} + 20$ min. For the basic experiment, the minimum vertical velocity $\overline{w_{min}^{cb}}$ is $-10.19$ m s$^{-1}$, while the downdraught in EXP6 is, with $\overline{w_{min}^{cb}} = -7.74$ m s$^{-1}$, about 24% weaker. This difference in the downdraught strength is due to the larger temperature excess of the warm bubble in EXP6, which leads to a faster growth and decay of the cell, resulting in a weaker downdraught and gust front than in the basic experiment.

I examine now in more detail all the new cells listed in Table 5.1. In all but one experiment, the first new cell develops at, slightly behind, or ahead of the NW edge of the cold pool, at the location where the surface convergence is largest. However, in EXP4 (Wsb-experiment) the first new updraught forms at the western edge of the gust front, where the convergence is smaller than in the NW. This apparent inconsistency will be discussed in section 5.5.5, where the buoyancy and pressure gradient forces are studied.

Of the 17 subsequent cells studied, 76% of them form southwest of the previous updraught. An example for this development is shown in Figs. 5.5 and 5.6. In Fig. 5.5a, only

the first cell which formed at the NW edge of the cold pool is apparent. Figures 5.5c and 5.6a show the second to fourth new cell which appear in the SW or south of the previous cell. The reason for this organisation is that the sea breezes, together with the low-and mid-levels winds, form an environment where the convergence is large to the SW of the previous cell. Thus, the line becomes oriented perpendicular to the low-level shear (see section 5.3.1). In two of the 17 cases, the convergence is not strongest at the location where the cells form. On the other hand, there are cases where, even though there is significant convergence, for example, at the northern edge of the cold pool in Fig. 5.5b, the new cell development is suppressed. The comparison of the distances between neighboring cells shows that a new updraught forms only at a distance larger than 5 km to the pre-existing ones. This organisation is because subsidence from previous cells suppresses convection in their surrounding (see section 5.5.5).

In summary, the regions where new cell development is possible can be predicted well by examining the low-level horizontal convergence in the model. However, in three cases (EXP4, first cell; basic experiment, third cell; EXP2, third cell), deep convection does not occur at locations where the convergence is at a maximum. Further, there are regions of weak ascent, such as at the northern and NNW edge of the gust front, but where convection is suppressed. Thus, even though the initiation of convection by density currents is primarily a function of horizontal convergence, there are several other factors that play a role. These factors were studied theoretically and numerically in the past decades, but often only in two dimensions. The theories and factors are discussed in the following sections, on the basis of all experiments (EXP1 to 7, basic experiment). It should be noted that the modelled multicell complexes and density currents show significant three-dimensional features, which could potentially limit the applicability of two-dimensional theories to interpreting overall system characteristics. Furthermore, the environmental shear profile of the 14 November 2005 case is neither idealised, nor restricted to low-levels. This makes it difficult to apply the results of existing studies to the observations of the Northeaster, and to the model results obtained here.

## 5.5.4   Vertical wind shear

As shown in chapters 3 and 4, the overall evolution of a thunderstorm depends strongly on the vertical wind shear. In order to study the effect of the wind profile on the evolution of the Northeaster, the basic experiment is modified in that idealised wind profiles are used, instead of that from 14 November 2005. Later on, the interaction between the environmental and cold pool shear will be studied, in the light of the Rotunno-Weisman-Klemp-theory.

### Tilting of the updraught

In EXPs 7.1 to 7.3, the wind velocity is chosen to be constant with height (see Table 5.1). This lack of wind shear results in 79% larger updraught velocities than in the other experiments. The strong updraughts and the large amounts of ice and water loading cause powerful downdraughts in EXPs 7.1 to 7.3, although, the surface convergence at the leading edge of the cold pool is significantly smaller than in the experiments where multicell complexes develop. While the gust front is strong over more than 20 min in the cases where a complex develops, in EXPs 7.1 to 7.3, it starts to decay about 10 min after
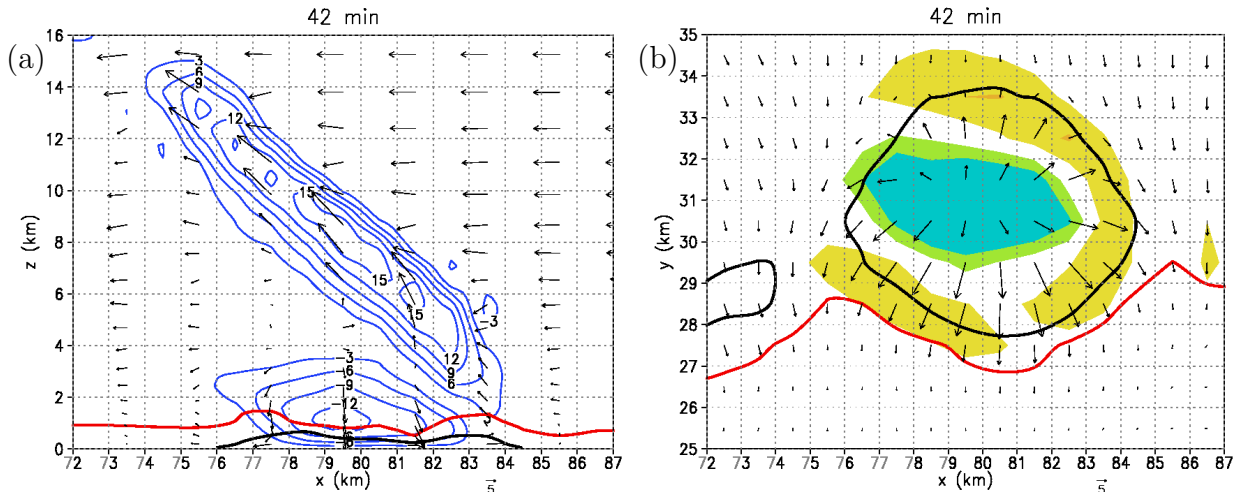
Figure 5.8: (a) Vertical cross-section at $y = 30.5$ km, and (b) horizontal cross-section at low-levels through the initial updraught in the NWsb-Nsb-EXP 7.5, where the wind profile is given by Eq. (5.2), with $u_{max} = -14$ m s$^{-1}$, $v_{max} = 0$, and $z_1 = 7.5$ km. The sea breeze front and the gust front are denoted by the thick red and black lines, respectively. (a) Vectors represent the $(u, w)$-flow, and $w$ is denoted by the blue contours. (b) Vectors represent the $(u, v)$-flow at $z = 0.06$ km, and regions of updraught velocities at cloud base larger than 2 m s$^{-1}$ and 5 m s$^{-1}$ are shaded in yellow and orange, while regions of downdraught $< -2$ m s$^{-1}$ and $< -5$ m s$^{-1}$ are shaded in green and light blue, respectively.

the cold pool formed and no new cell develops. The reason for the weak gust front and thus, for the small amount of low-level convergence at its leading edge, is the lack of strong tilting of the updraughts in EXPs 7.1 to 7.3.

The slope of the updraught is affected significantly by mid-tropospheric wind shear (Keenan and Carbone 1991), as well as by the low-level shear which is generated by density currents or the environment (see below). In the basic experiment, the Nsb and the environmental wind advect and tilt the initial updraught towards the NW, which results in a downdraught located NW of the updraught centre (compare Fig. 5.4c and 5.4d), allowing the downdraught to supply the NW region of the gust front continuously with cold air. In EXPs 7.1 – 7.3, on the other side, the initial updraughts are tilted only slightly towards the north due to the vorticity generated by the Nsb. The weak tilting causes the downdraught to fall into the updraught and its inflow what results in a rapidly weakening of the updraught. Moreover, the lack of tilting leads to a cold pool which is coldest in the centre, underneath the initial cell, but too warm at the edges to oppose the sea breeze flow in which it spreads out. Thus, the convergence is much smaller along the less developed gust front of EXPs 7.1 – 7.3 than in the other experiments, and no new cell development commences due to the lack of tilting.

As the horizontal vorticity generated by the Nsb is not large enough to tilt the updraught sufficiently so that the downdraught, and thus the gust front, are generated away from the base of the updraught, an environmental wind shear over a depth larger than that of the sea breeze is necessary to cause significant updraught tilting. In the basic experiment and in EXPs 1 to 6, the environmental south-easterly winds below 500 hPa,

together with the vorticity generated by the density current (Nsb), play the most important roles in determining the tilting direction and strength. This finding is confirmed by several model runs with a NWsb and a Nsb using different idealised wind profiles. For example, in EXP7.4, where the wind components $u_i = (u, v)$ increase linearly with height and are constant above $z = z_1$:

$$u_i(z) = \begin{cases} u_{i,max}(z\,z_1^{-1}) & \text{for } z \leq z_1, \\ u_{i,max} & \text{for } z > z_1, \end{cases} \qquad (5.2)$$

with $u_{max} = -14$ m s$^{-1}$, $v_{max} = 5$ m s$^{-1}$, and $z_1 = 7.5$ km, the initial updraught is tilted strongly towards the NW. New cell development is then found at the NW edge of the cold pool as the latter is supplied continously by cold air from the downdraught. Strong westward tilting of the initial updraught in EXP 7.5, with $u_{max} = -14$ m s$^{-1}$, $v_{max} = 0$, and $z_1 = 7.5$ km, is apparent in Fig. 5.8a. Because the wind profile has the shear vector pointing towards the west, the updraught, and especially the upper portion of it, is advected towards the west. This advection results in a downdraught that forms west of the mid-level ($z = 4.6$ km) portion of the updraught, instead of falling into it. As a result, the downdraught supplies the western portion of the cold pool with cool air (Fig. 5.8b), while the inflow from the east is able to supply the updraught with warm and moist environmental air (Fig. 5.8a).

The importance of updraught tilt and of a continuous supply of cool air to the gust front is apparent from a simple experiment. Instead of initialising the basic experiment with a warm bubble which triggers convection, a cold bubble with $\Delta\theta = -30$ K is initialised behind the Nsb front to represent a pool of cold air, *i.e.*, the gust front. Horizontal convergence at the edges of the cold pool in the toy model is large at the beginning, but decreases rapidly due to the lack of a downdraught which feeds the pool. Instead, the gust front is advected south by the Nsb and weakens significantly, thus, not allowing enough time for the formation of new cells.

**RKW-theory**

In previous studies, Rotunno *et al.* (1988; hereafter RKW88), Weisman *et al.* (1988), and Weisman and Rotunno (2004) examined the role of the cold pool and low-level shear on the development of convection and its characteristics. They point out that the cold-pool-shear relationships are "the most fundamental internal control on squall-line structure and evolution". A schematic diagram depicting the influence of a density current and of low-level environmental wind shear on an existing updraught is shown in Fig. 5.9. From Fig. 5.9b it is apparent that, in a environment without shear, a density current leads to an updraught which is tilted towards the rear due to the influence of the negative horizontal vorticity at the edge of the cold pool. However, the cold pool's negative vorticity might be balanced by a circulation associated with positive vorticity of the low-level environmental wind shear (Fig. 5.9d). This results in deep lifting at the nose of the outflow, and thus in an upright updraught as if there were neither a cold pool, nor environmental shear (Fig. 5.9a). RKW88 found, that a criterion for the ability of a cold pool to generate a vertically erect circulation is

$$c_{pool} = \Delta c_{env} \qquad \textbf{RKW-criterion (for deepest vertical lifting)} \qquad (5.3)$$
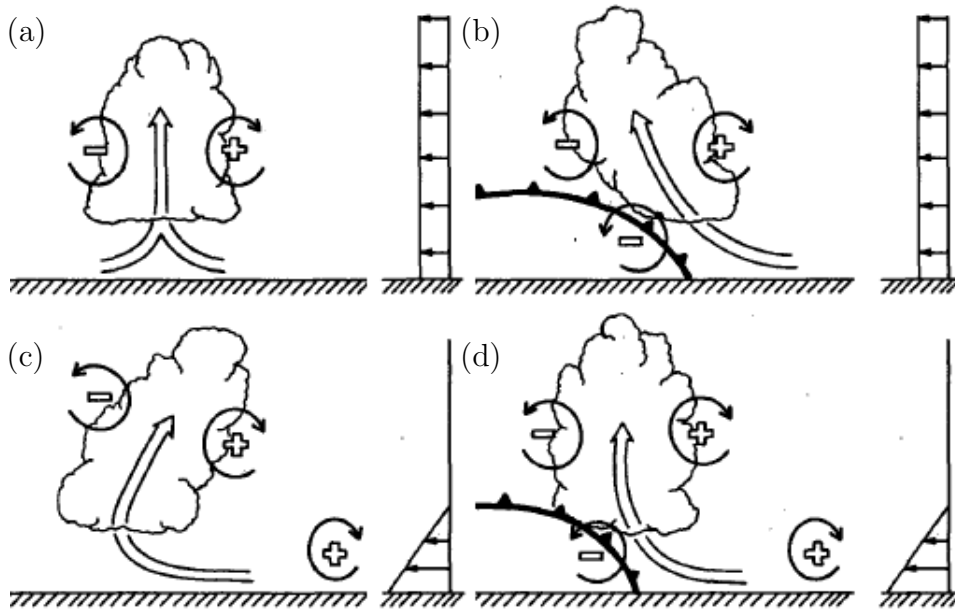
Figure 5.9: Schematic diagram showing how an updraught is influenced by environmental wind shear and/or a density current (barbed line). The signs "+/−" stand for positive and negative horizontal vorticity, respectively. (a) In an environment without environmental shear, and without a density current, the axis of the updraught is vertical due to a symmetric vorticity distribution. (b) In a shearless environment, the distribution is biased if a density current surges underneath the thermal, causing the updraught to lean towards the rear of the current. (c) With low-level environmental shear, but without a cold pool, the distribution is biased towards positive vorticity. (d) With low-level environmental shear and a density current, the circulation associated with the cold pool's negative vorticity may balance the circulation of the low-level shear (adapted from RKW88).

where $\Delta c_{env} = c_{z_2} - c_{z_1}$ is the difference between the environmental wind velocity at $z = z_2$ and $z = z_1$, and $c_{pool}$ is the theoretical speed of propagation of the (two-dimensional) density current given by:

$$c_{pool}^2 = 2 \int_0^H (-B)dz, \tag{5.4}$$

with $H$ representing the depth of the cold pool, and $B$ being the buoyancy. The RKW-criterion expresses the fact that a cell triggered by a cold pool can only realize its full potential when the cold pool circulation is countered by that of the shear (see Fig. 5.9d). When $c_{pool}/\Delta c_{env} \gg 1$, lifting at the head of the density current is decreased significantly, and cell generation is restricted. If $c_{pool}/\Delta c_{env} \ll 1$, the cell generation is limited also, as the new updraughts loose energy due to the strong environmental wind shear.

While the calculation of $\Delta c_{env}$ for idealised wind profiles[5] is straight forward, the com-

---

[5] For the curved hodograph used in chapter 4 [Eqs. (4.1), (4.2)], the difference between the environmental wind velocity at a height $z = z_2$ and the surface is

$$\Delta c_{env} = \frac{\sqrt{2}U_s}{\pi}\sqrt{1 - \cos\frac{z_2\pi}{h}}. \tag{5.5}$$

putation becomes more complex when the change of the wind direction and magnitude with height can not be expressed analytically, as it is the case for the 051114-profile. Furthermore, because of the model settings in EXPs 1 to 7 and the basic experiment, $c_{pool}$ is more difficult do determine with Eq. (5.4) than in cases without sea breezes, with an idealised wind field, or in a two-dimensional model. Together with the idea of the RKW-theory that the vorticity due to the environment needs to be balanced by that of the cold pool, these factors lead to the formula

$$
\begin{aligned}
\frac{\Delta c_{pool}}{\Delta c_{env}} &= \frac{\|(u_2, v_2) - (u_1, v_1)\|_{behind}}{\|(u_2, v_2) - (u_1, v_1)\|_{ahead}} \\
&= \frac{\sqrt{(u_2 - u_1)^2 + (v_2 - v_1)^2}|_{behind}}{\sqrt{(u_2 - u_1)^2 + (v_2 - v_1)^2}|_{ahead}},
\end{aligned} \tag{5.6}
$$

where $(u_2, v_2)$ is the wind vector at the top of the shear layer, $z = z_2$, and $(u_1, v_1)$ is the wind vector at the base of it, $z = z_1$. To determine $\Delta c_{pool}$, $(u_i, v_i)$ $(i = 1, 2)$ are taken behind the leading edge of the cold pool, while the wind components ahead of the front are used to calculate $\Delta c_{env}$. Thus, by using Eq. (5.6), the vertical shear created by the cold pool and by the environmental wind above it is compared with the environmental shear ahead of the cold pool. The RKW-criterion is different to that here in that it suggests that the speed of the cold pool is compared with the difference of the environmental wind velocities between $z_2$ and $z_1$.

The studies in RKW88 and Weisman and Rotunno (2004) showed that the shear in a layer in close proximity to the density current is most influential on convective development. In the experiments of RKW88 and Weisman *et al.* (1988), strong vertical lifting occurred for moderate-to-strong environmental shears confined to the lowest 2.5 km, while deeper shear was less conductive to maintain long-lived squall lines. A shear layer displaced to the top of the cold pool had a negligible effect on the low-level lifting. In Weisman and Rotunno (2004), a better correspondence with the overall system structure was obtained when $\Delta c_{env}$ was calculated over the lowest 5 km, instead over the lowest 2.5 km. Due to the different results obtained in RKW88 and Weisman and Rotunno (2004), the environmental shear $\Delta c_{env}$ and the cold pool shear $\Delta c_{pool}$ in this study are calculated over three different height levels: $z_1$ to $z_2 = 0 - 1.1$ km, $0 - 2.5$ km, and $0 - 5$ km. For the basic experiment and EXPs 2 – 5, the shear ratios $\Delta c_{pool}/\Delta c_{env}$ are calculated in the region of every new cell as summarised in Table 5.2.

Figures 5.10a and b show horizontal cross-sections through the storm system of the basic experiment, with the $0 - 1.1$ km shear vectors plotted at every second grid point. New cells are denoted by yellow and orange shading. In general, the shear vectors behind the gust front (thick black line) point towards the centre of the cold pool, while the shear vectors in the environment point towards the north or NW, mainly due to the propagating Nsb and NWsb. The wind components for calculating the shear ratio given by Eq. (5.6) are determined at the location where every new cell develops, at the time when the cell updraught becomes stronger than 5 m s$^{-1}$. For the first cell in the basic experiment, a 0 – 1.1 km-shear-ratio of 1.83 is obtained, with an angle in between the two shear vectors of about 180°. This is apparent from Fig. 5.10a, where the arrow south of the cell is almost twice as large as that north of the cell, with the vectors pointing in opposite directions. In RKW88, the environmental shear is calculated at the beginning of the analysis, without
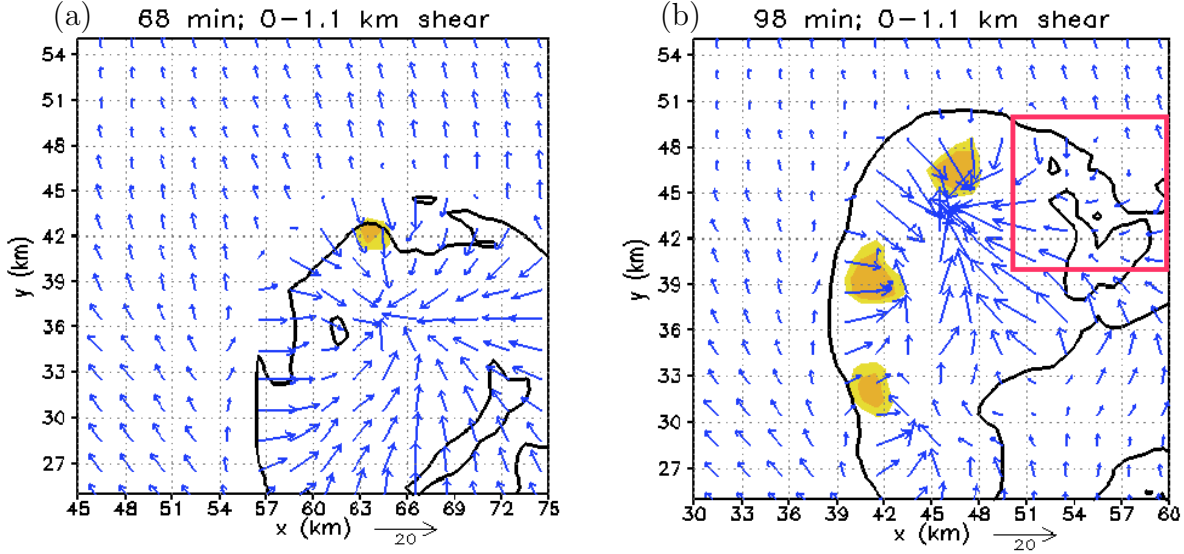
Figure 5.10:   Horizontal cross-section through the storm system in the basic experiment, at (a) 68 min, and (b) 98 min. Regions of updraught velocities at $z = 4.6$ km, larger than 5 m s$^{-1}$ and 10 m s$^{-1}$ are shaded in yellow and orange, respectively. The surface gust front is denoted by the thick black line and represents the $-0.5$ K temperature perturbation contour. Vectors represent the $0 - 1.1$ km shear vectors, described by $\sqrt{(u_2 - u_1)^2 + (v_2 - v_1)^2}$ (see Eq. 5.6). The region in the red square of panel (b) will be discussed in section 5.5.5.

taking into account the effects of the storm evolution. As the multicell complex can exert a significant influence on the environmental wind field, especially on the low-level shear (Lafore and Moncrieff 1990), the vertical wind shear behind and ahead the gust front is recalculated every time a new cell develops. As can be seen in Fig. 5.10b, the second and third new updraughts develop in environments where the angle between the shear vectors is smaller than 180°.

The calculation of the shear ratios and angles for all experiments with new cell genera-tion reveals that $\Delta c_{pool}/\Delta c_{env}$ is close to 1 in all experiments (see Table 5.2). This confirms the RKW-criterion in that the new cells develop in environments where the vorticity as-sociated with the cold pool is balanced by the vorticity generated by the environmental shear ahead of the gust front. One distinctive feature, apparent from Table 5.2, is that $\Delta c_{pool}/\Delta c_{env}$ calculated over the lowest 1.1 and 5.0 km are comparable and larger than 1, while $\Delta c_{pool}/\Delta c_{env}$ calculated over the lowest 2.5 km is, on average, smaller than 1. These differences are due to very strong environmental winds at $z = 2.5$ km with about 12 m s$^{-1}$, while the winds are only about 4 m s$^{-1}$ at $z = 1.1$ km and 5.0 km. Thus, even though the winds are easterly at low- and mid-levels (see Fig. 5.3), the different velocities at these height levels produce different strengths of wind shear. Another distinctive feature is that in the experiments where large multicell complexes develop (basic, 4, 5), the ratios are larger, on average, than in the cases where only few new cells form (EXP2, EXP3).

In summary, the values obtained for $\Delta c_{pool}/\Delta c_{env}$, calculated in close proximity to the locations where new cell development occurs, confirm that Eq. (5.6) is an indicator for new cell development. However, the question is to what extent the formulae and

| EXP | 0 − 1.1 km ratio | 0 − 1.1 km angle | 0 − 2.5 km ratio | 0 − 2.5 km angle | 0 − 5.0 km ratio | 0 − 5.0 km angle |
|---|---|---|---|---|---|---|
| all | 1.7 ± 1.1 | (118±47)° | 0.8 ± 0.5 | (114±58)° | 1.4 ± 0.8 | (97±50)° |
| basic | 1.8 ± 1.4 | (98±51)° | 0.9 ± 0.5 | (106±70)° | 1.3 ± 0.8 | (65±51)° |
| 2 | 1.1 ± 0.3 | (137±49)° | 0.6 ± 0.4 | (105±76)° | 1.0 ± 0.4 | (106±56)° |
| 3 | 1.3 ± 0.7 | (155±74)° | 0.6 ± 0.5 | (68±75)° | 1.2 ± 0.6 | (123±88)° |
| 4 | 2.5 ± 0.9 | (112±32)° | 1.2 ± 0.6 | (136±56)° | 2.2 ± 1.0 | (105±39)° |
| 5 | 1.3 ± 0.8 | (129±52)° | 0.6 ± 0.2 | (123±33)° | 1.1 ± 0.5 | (117±42)° |

Table 5.2: Shear ratios $\Delta c_{pool}/\Delta c_{env}$ according to Eq. (5.6), and angles between the environmental and cold pool shear vector, for all experiments with new cell formation.

the theory can be applied to three-dimensional cases with non-idealised wind profiles. The large standard deviations for the shear ratios and angles make it difficult to provide thresholds for which new cells can be expected. Furthermore, there are regions where the amount of shear ahead of and behind the leading edge of the cold pool seem to be comparable, but no new cell development occurs (see Fig. 5.10b, red box). In these cases, convection might be suppressed due to unfavourable mid-tropospheric environments (Wilson and Schreiber 1986, Rao and Fuelberg 2000). Lafore and Moncrieff (1989, 1990) studied the organisation and interaction of convective regions of tropical squall lines and found that the strength and form of the low-level shear is important for the longevity and intensity of these storm systems, a result that is consistent with the RKW-theory. However, when systems with extensive stratiform regions are considered, other factors can influence the evolution and characteristics of the storm system, such as the wind profile in the mid- to upper-levels, and the differential movement of convective cells. Thus, while the fulfilment of the RKW-criterion might be a necessary condition, it is not always sufficient for convective development.

### 5.5.5 Vertical perturbation pressure gradient and buoyancy

As we have seen in the previous sections, there is no generation of new cells at the northern and NNE edge of the gust front, even though the surface convergence is significantly large and the RKW-criterion is fulfilled. To determine why no thunderstorm develops, even though there is weak ascent at low-levels, I consider the vertical acceleration, given by Eq. (2.18):

$$\frac{\partial w}{\partial t} = \underbrace{- \left( u\frac{\partial w}{\partial x} + v\frac{\partial w}{\partial y} + w\frac{\partial w}{\partial z} \right)}_{\text{ADV}} \underbrace{- c_p\theta_\rho\frac{\partial \pi'}{\partial z}}_{\text{PGF}} + \underbrace{g\left( \frac{\theta_\rho}{\theta_{\rho 0}} - 1 \right)}_{\text{B}}. \qquad (5.7)$$

The terms on the right hand side of this equation represent the three-dimensional advection of vertical momentum (ADV), the vertical perturbation pressure gradient force (PGF), and the buoyancy force $B$. Note that the buoyancy force term appears different from that in other models (Rao and Fuelberg 2000, Heus and Jonker 2008), as the momentum equation in Bryan's model is derived without any approximations.

Figure 5.11a shows a horizontal cross-section at $z = 4.3$ km through the storm system of the basic experiment. The net vertical acceleration, $\partial w/\partial t$, at 74 min is shaded in the region where new cell development occurs. At the locations where the first and second
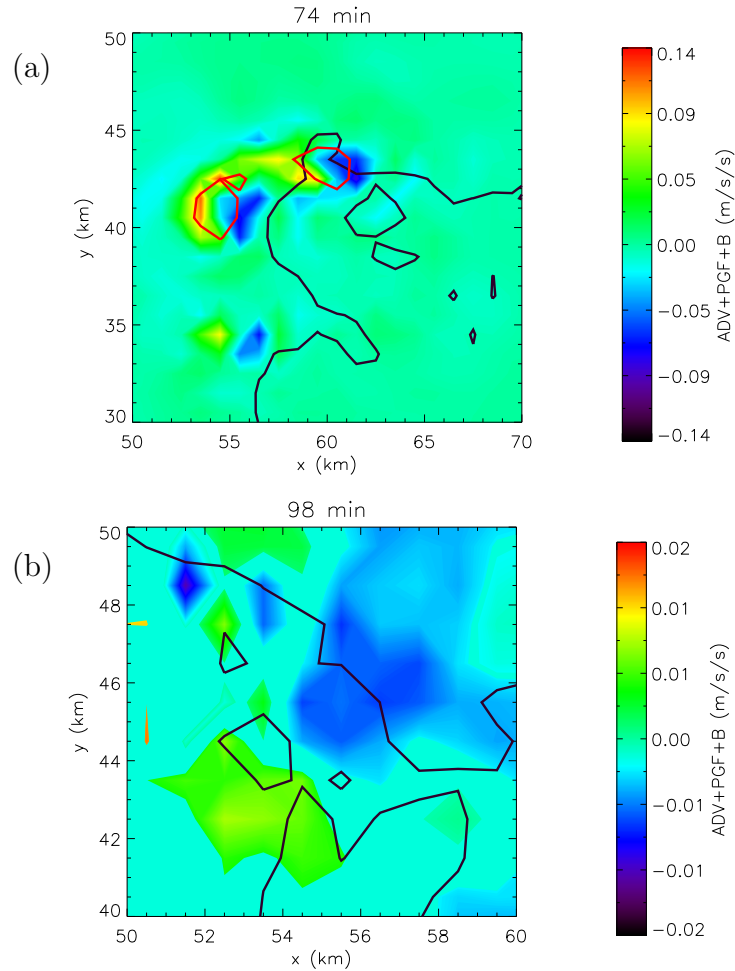
Figure 5.11:   Net vertical acceleration $\partial w/\partial t$ (shaded) at $z = 4.3$ km, (a) 74 min and (b) 98 min after initialisation of the basic experiment. The surface gust front is denoted by the thick black line and regions of updraught with $w > 5$ m s$^{-1}$ at 4.6 km are contoured in red. Note that different scalings for the shading of the $\partial w/\partial t$ values are used in the panels. Panel (b) is a zoom into the area depicted in Fig. 5.10b (red box).

updraught developed and where the third cell is about to form, $\partial w/\partial t$ is positive due to the positive buoyancy associated with the rising air. Because of the environmental wind and due to the shear generated by the cold pool, the updraughts are tilted towards the east, resulting in downdraughts east of the updraught centres. This explains the regions with $\partial w/\partial t < 0$ (shaded in dark blue), which results from the large negative buoyancy $B$ within the downdraught.

In most parts of the domain, a positive buoyancy force is cancelled by a negative pressure gradient force, because rising motion at $z = z^*$ due to $B > 0$ results in low perturbation pressure below $z^*$ and in high perturbation pressure above $z^*$. In contrast, negative buoyancy is cancelled in many regions by a positive pressure gradient force, leading also to a zero net acceleration. However, in regions of strong downdraughts (Fig. 5.11a) or subsidence, the positive pressure gradients are not large enough to overcome the negative buoyancy. Figure 5.11b is a zoom into the region east of the first new cell of the basic experiment, which occurred at the NNW edge of the gust front (red box in Fig. 5.10b).
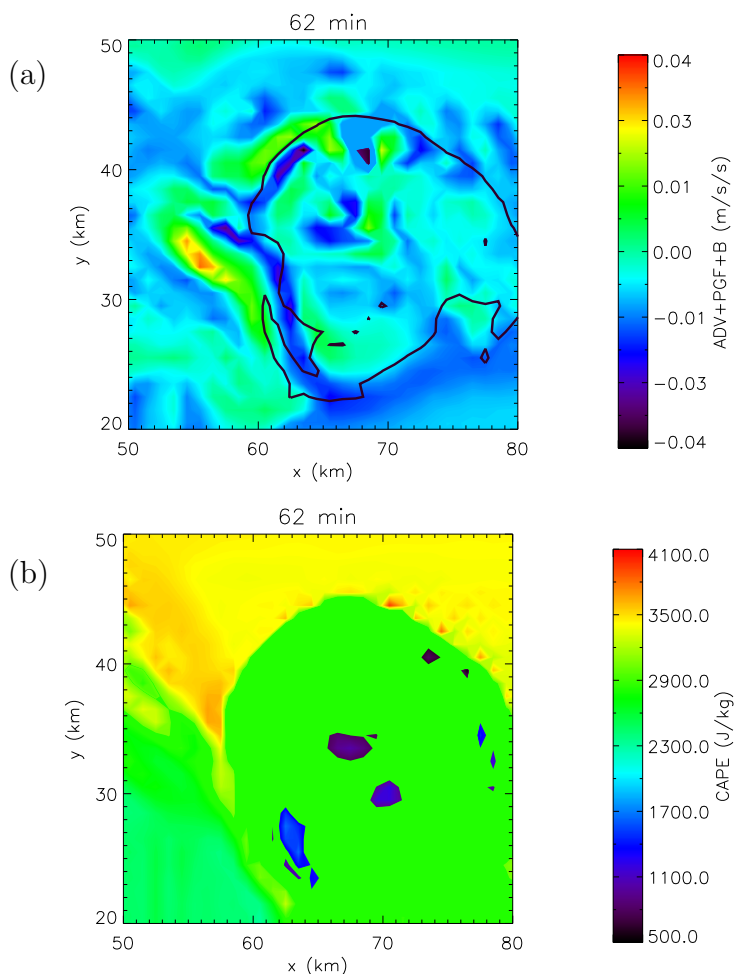
Figure 5.12:   Plotted are (a) the net vertical acceleration $\partial w/\partial t$ (shaded) at $z = 2.2$ km, and (b) CAPE, 62 min after the initialisation of EXP4. The surface gust front is denoted by the thick black line in (a).

In this area, the vertical acceleration is negative (light and dark blue shading) due to subsidence from the first new updraught. The sinking motion prevents new cell formation at the NNE edge of the gust front, even though there is weak ascent at low-levels (see Figs. 5.5d, 5.6b) and even though the RKW-criterion is fullfilled (Fig. 5.10b).

With the aid of the vertical momentum acceleration equation, Eq. (5.7), not only the suppression of convective development can be explained, but also why, in some cases, convection forms even though the surface convergence is not maximised in a specific area. The latter is the case in EXP4, where the first new cell is generated at the western edge of the cold pool, even though the surface convergence would have been larger at the NW edge. Figure 5.12a shows the region behind the westerly and northerly sea breeze fronts. The surface cold pool is denoted by the thick black line, and $\partial w/\partial t$ at $z = 2.2$ km is shaded. At 62 min, the vertical acceleration is largest in the west, ahead of the gust front, because of a positive buoyancy force that is not compensated by the pressure gradient force. This force imbalance leads to the formation of the first new cell after 66 min, at $(x,y)=(54$ km, 34 km). Thus, in EXP4, the Wsb creates larger low-level instability at the western edge of the cold pool than at the NW edge. Figure 5.12b shows the CAPE of a parcel lifted

from the surface for the same time and region as in Fig. 5.12a. The comparison of both panels shows that, in this case, the development of a new cell at the western edge of the gust front could not have been predicted by the CAPE value itself. The CAPE values are significantly smaller in the west than in the NW, suggesting that convection is more likely in the NW.

The development or suppression of convection that could not be explained by considering the low-level convergence (section 5.5.3), or by applying the RKW-criterion (section 5.5.4), is clear when the vertical momentum acceleration is considered. Negative buoyancy at mid-levels that is larger in magnitude than PGF+ADV can suppress convection, while positive buoyancy at low-levels indicates large instability and may favour convective development.

## 5.5.6   Other factors enhancing or suppressing convective motion

Other factors in addition to the surface convergence, the ratio of cold pool strength to the environmental shear, the low-level instability, and subsidence can be important when new cell generation is considered. Some of these factors are discussed briefly below, but are not investigated here.

### Kelvin-Helmholtz instability

Kelvin-Helmholtz instability (KHI) occurs in regions of strong vertical wind shear and/or where there is a local minimum of static stability in the mean flow, and can interact with density currents, such as sea breezes and gust fronts (Houze 1993). Rao and Fuelberg (2000) examined the role of KHI in creating preferred areas for convection behind the Cape Canaveral sea breeze front. They found that in a region where storm development was suppressed, Kelvin-Helmholtz billows affected the distribution of upward motion and the buoyancy force overcame the suppression. Thus, a favourable environment for convective development was created. The results of Rao and Fuelberg (2000) suggest that KHI helps in developing a preferred region for the development of storms. In contrast to their findings, Kingsmill's (1995) study showed that the KHI-induced updraught pattern on the gust front was not critical to convective development.

### Shape of the density current

Kingsmill (1995) examined the initiation of convection associated with the collision of a sea breeze front and a gust front using observational data collected in summer months in Florida. Kingsmill found that inflections, or kinks, in the boundary layer convergence zone can be preferred areas of convection initiation. At the intersection points of arc-shaped sea breeze segments, convergence and thus, ascent is enhanced.

### Rear inflow

A rear inflow jet is a circulation feature in which air enters and flows through the stratiform precipitation region of convective systems from the rear. These jets form in response to the upshear-tilting of the convective circulation, and supply cold and dry midlevel air that aids in the production of downdraughts. Rear-inflow jets become a significant component of the system-scale circulation during the mature phase of many simulated squall lines

(Weisman and Rotunno 2004). Their occurrence might complicate the relationship of the environmental wind shear and cold pool strength worked out by RKW88 (Lafore and Moncrieff 1989, 1990). However, Weisman and Rotunno (2004) point out that system-generated features, such as the rear-inflow jet, develop as a consequence of the cold-pool-shear relationships discussed above.

### 5.5.7 Multicell complex at later stages

**Tilting and propagation**

In the previous sections, the development of the initial cell leading subsequently to the formation of the multicell complex was studied in detail. At the time that the multicell complex develops, cell tilting is weak because of the compensation of the cold pool shear by the environmental shear $\Delta c_{pool} \simeq \Delta c_{env}$ (see Table 5.2). However, this relation changes significantly as the cold pool and the multicell complex propagate towards the west. The comparison of Figs. 5.6a and c shows that the cells of the multicell complex move backwards relative to the gust front with a speed of about 5.6 m s$^{-1}$. This rearward movement of the updraughts is associated with cell tilting towards the east, which becomes stronger with time (not shown). Because of the slope of the cells, the downdraughts and the regions of subsidence are located east of the updraught centres.

A similar behaviour of the overall system was found also by Lafore and Moncrieff (1989). They studied the organisation and interaction of convective regions of tropical squall lines and noted a differential propagation of cells and cold pool of about 10 m s$^{-1}$. In one of their models, the slope of the system changed when the distance between the gust front and the cells exceeded about 30 km. As a result the "rotor circulation" in the density current which is driven by water loading and evaporation associated with the cells, became stronger (see Lafore and Moncrieff 1989, Fig. 9).

**Dynamic structure**

If a multicell complex forms in an environment with large thermodynamic instability and strong vertical wind shear, the individual cells often show characteristics similar to those of isolated supercells (Weisman *et al.* 1988). One distinctive feature between ordinary cells and supercells is that the updraughts of the latter are rotational, while ordinary cells show no correlation of the updraught with vertical vorticity (see chapters 3, 4, and WK84).

In the basic experiment and in EXPs 1 to 6 where the 051114-wind profile is used, none of the new cells forming the multicell complex show a clear correlation between $\zeta$ and $w$. On the other hand, in EXP7.6 three new cells develop. In this experiment, the wind profile is given by Eq. (5.2) with $u_{max} = -14$ m s$^{-1}$, $v_{max} = 0$, and $z_1 = 3.3$ km, giving a shear of $4.24 \times 10^{-3}$ s$^{-1}$. While the first and second cell decay 10 to 20 min after their formation, the third cell is long-lived, and its updraught centre is correlated well with negative vorticity at mid-levels (see Fig. 5.13). Thus, even though the magnitude of shear in EXP7.6 is comparable to that in the experiments with the 051114-wind profile ($\approx 15.4$ m s$^{-1}$/3.7 km $= 4.16 \times 10^{-3}$ s$^{-1}$), the dynamics of one of the cells in EXP7.6 is different. This finding confirms that in environments with comparable CAPE, not only the magnitude of environmental shear (chapter 3), but also the curvature of the hodograph (chapter 4), the depth of the shear layer (section 3.4.3), and the vertical shear generated by density currents (section 5.5.4) have importance for the dynamics of a cell.
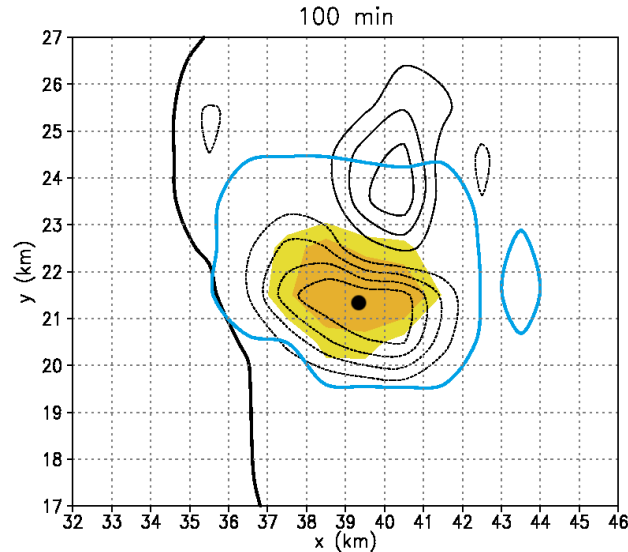
Figure 5.13: Mid-level ($z = 4.6$ km) storm structure of the third cell in EXP7.6, at 100 min. The surface gust front which is propagating towards the west is denoted by the thick black line and represents the $-0.5$ K temperature perturbation contour. Regions of updraught velocities at $z = 4.6$ km larger than 5 m s$^{-1}$ and 10 m s$^{-1}$ are shaded in yellow and orange, respectively, and the location of the updraught centre is denoted by a black dot. Vertical vorticity $\zeta$ is contoured every $2 \times 10^{-3}$ s$^{-1}$ with positive values depicted by solid black lines, negative values represented by dotted black lines, omitting the zero contour. The solid blue line encloses the region of rainfall ($q_r > 0.1$ g kg$^{-1}$).

## 5.6   Non-severe Northeaster on 7 February 2006

Multicellular thunderstorm complexes, like the Northeaster investigated here, are not necessarily severe. A non-severe Northeaster occurred on 7 February 2006 (YYMMDD = 060207), passing over the city of Darwin at about 0618 UTC (3.48 pm local time). Based on the findings described in the previous sections, this non-severe thunderstorm complex will be studied below. Even though the investigation is carried out in less detail than that for the 051114-Northeaster, it will help to summarise and underline important factors which play a role in the evolution of multicell complexes.

### 5.6.1   Model configuration

The model configuration for the 060207-Northeaster experiment is the same as for the 051114-Northeaster basic experiment, except that the 0000 UTC Darwin sounding from 7 February 2006 is used (see Fig. 5.14). Like for the 051114-experiments, the 060207-sounding is modified in the lowest 1 km to represent mid-afternoon conditions ($\theta_0 = 304.45$ K, and $q_{v0} = 18.30$ g kg$^{-1}$). The modification of the 060207-sounding towards a slightly smaller surface mixing ratio than that in the 0000 UTC-sounding is necessary in order to suppress unobserved convection in the model run. The resulting CAPE has a value of 2369 J kg$^{-1}$ , which is 43% smaller than in the 051114-experiment. At the beginning of the simulation of EXP060207, CAPE = 2369 J kg$^{-1}$ ahead of the sea breezes, and CAPE = 1854 J kg$^{-1}$ behind them.
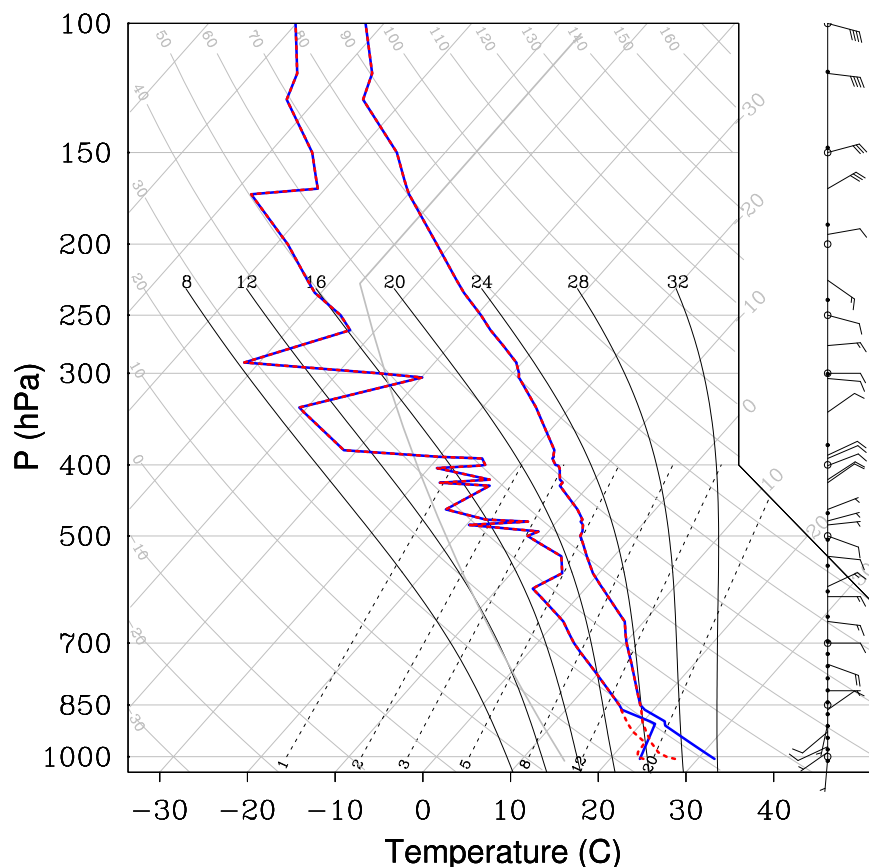
Figure 5.14: Skew$T$-log$p$ diagram showing the temperature and dew-point temperature of the 7 February 2006, 0000 UTC sounding as used in the simulations (blue, solid lines) and unmodified (red, dashed lines). Every second wind barb is plotted on the right.

While the upper-level wind vectors in the 060207-profile and 051114-profile point in opposite directions, the wind speeds and directions at low- and mid-levels are comparable. Significant wind shear is confined to the lowest $\approx 3$ km (compare Fig. 5.3 with Fig. 5.14), with the shear magnitude in the 060207-profile being smaller than that in the 051114-profile ($9.8$ m s$^{-1}$/2.6 km versus $15.4$ m s$^{-1}$/3.7 km).

## 5.6.2    Evolution of the multicell complex

The overall evolution of the 060207-Northeaster is similar to that on 14 November 2005. The first echo formed at about 0418 UTC, NE of Koolpinyah (see Berrimah radar image, Fig. 5.15a, red arrow). The initial cell progressed towards the west, and new cell development occurred, presumably at the gust front of the initial updraught. At 0618 UTC, the system had developed into a multicell complex which was located over the city of Darwin (Fig. 5.15c, blue arrow). The storm system which is oriented slightly NNW/SSE, propagates towards the WSW and survives yet another 2 hours.

The lack of a Severe Thunderstorm report and of a complete sequence of radar images makes it more difficult than in the 051114-case to compare the results of the numerical model in detail with the event of 7 February 2006. Figures 5.15b and d show horizon-
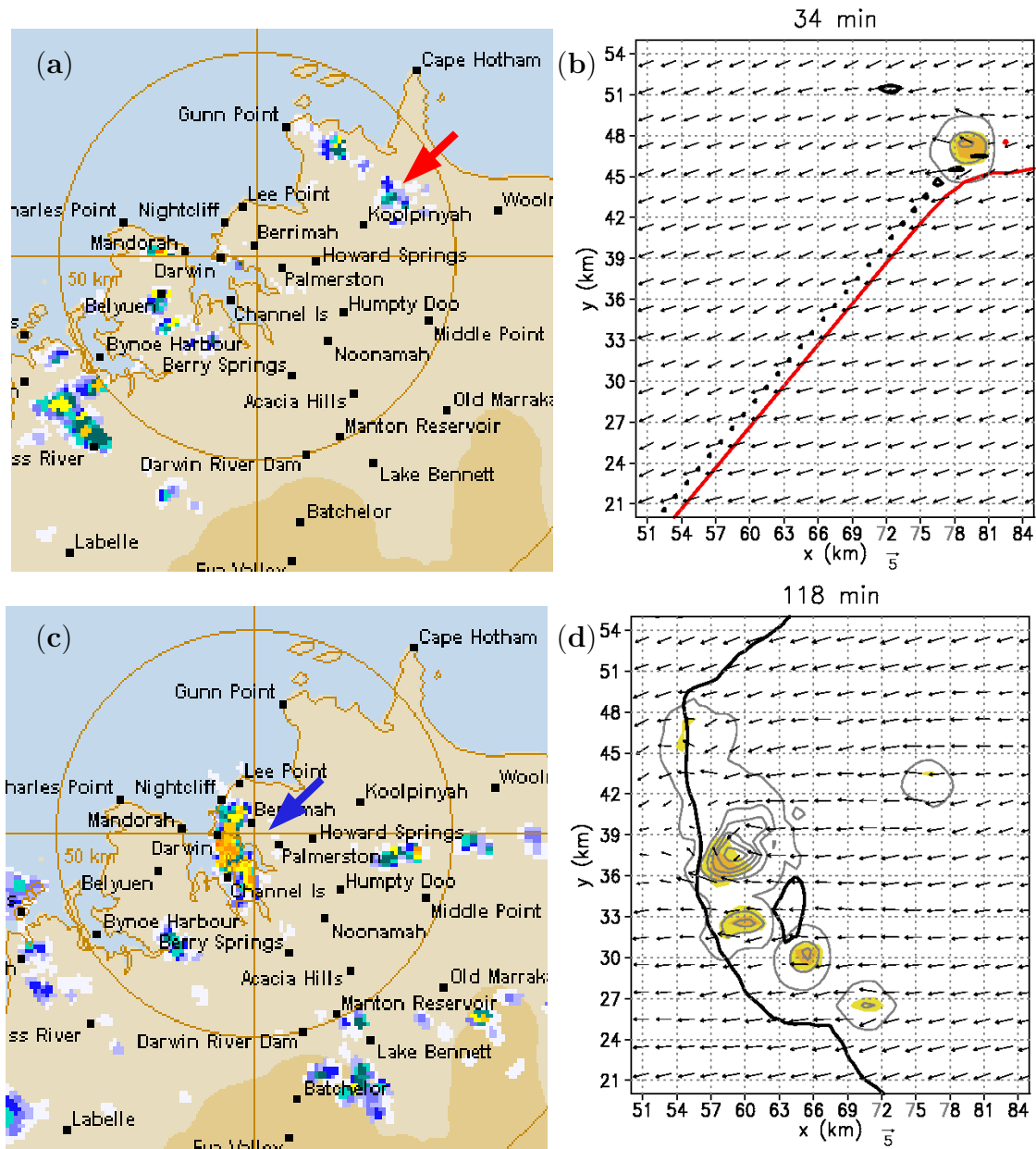
Figure 5.15:   Left panels: Berrimah radar images at (a) 0418 UTC, and (c) 0618 UTC on 7 February 2006.  Colours represent the rain rate, whereby white and blue stands for light, green and yellow for moderate, and red for heavy rain.  The circle has a radius of 50 km.  Courtesy of the Australian Bureau of Meteorology Regional Forecasting Centre in Darwin.  Right panels: Mid-level storm structure depicted at b) $t = 34$ and d) 118 min.  The sea breeze fronts and the gust front are denoted by the thick red and black lines, respectively.  Vectors represent horizontal flow at $z = 4.6$ km, and the total precipitation mixing ratio is contoured in grey at 2 g kg$^{-1}$ intervals, with the zero contour omitted.  Regions of updraught velocities at $z = 4.6$ km larger than 5 m s$^{-1}$ and 10 m s$^{-1}$ are shaded in yellow and orange, respectively.  Note that the scaling in the radar images is different to that in the model plots (factor $\approx 3$).
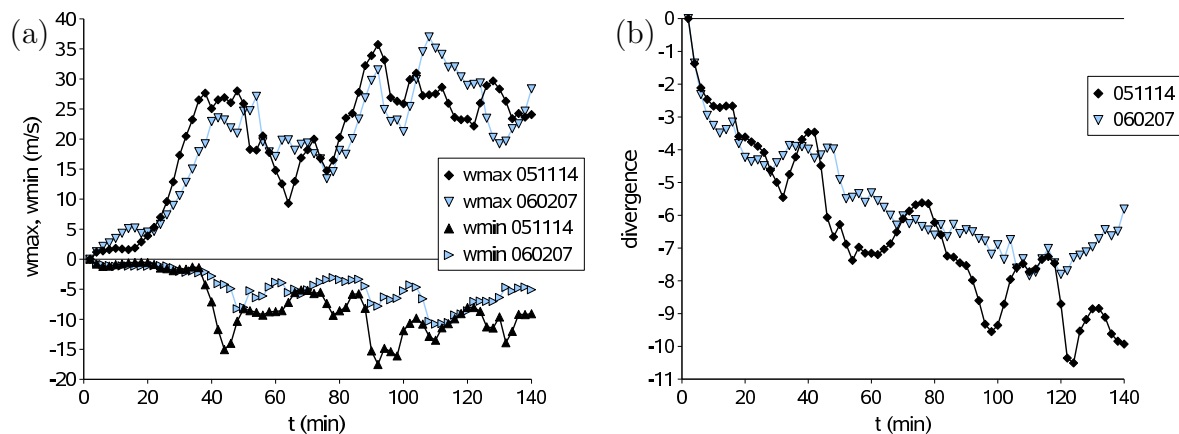
Figure 5.16: Time-series of (a) maximum vertical velocity $w_{max}$, and minimum vertical velocity at cloud base $w_{min}$ ($z = 1.3$ km), and (b) minimum in horizontal divergence at $z = 190$ m (in $10^{-3}$ s$^{-1}$), for the basic experiment carried out with the 051114-sounding, and the experiment run with the 060207-profile.

tal cross-sections through the initial model updraught and multicell complex, respectively. The initial cell, which is initialised so that it develops right above the Nsb front, progresses towards the west parallel to the front and reaches its maximum strength of $w_{max} = 27.1$ m s$^{-1}$ at about 54 min. The cold pool has formed at 34 min and spreads out, triggering the first new cell after 74 min at the western edge of the gust front. By 118 min, a total of five new cells has developed at the leading edge of the cold pool, forming a multicell complex (Fig. 5.15d). The multicell complex is oriented NNW/SSE, spans about 25 km in the horizontal, and progresses towards the WSW. Thus, the overall structure and development of the multicell complex compares well with the observations.

### 5.6.3   Comparison of the 051114- and the 060207-experiment

**Initial updraught and downdraught**

I compare now the results of the 051114-basic experiment and the 060207-experiment. Figures 5.16a and b show time-series of $w_{max}$, $w_{min}$ at cloud base, and the minimum in low-level horizontal divergence. Even though the amount of CAPE is significantly larger in the 051114-experiment than in the 060207-experiment, the peak updraught strength, $w_{max}$, is comparable in both cases. This reflects again the deficiencies of CAPE, in that it does not consider entrainment, precipitation loading, water vapour deficit, and vertical pressure gradient forcing (see section 3.2.2). On average, the updraught between $t = 20$ to 50 min is stronger in EXP051114, resulting in a 40% larger maximum of hydrometeor mixing ratio and thus, in a stronger downdraught than in the EXP060207.

**New cell development at the gust front**

The downdraught results in a cold pool that is shown in Figs. 5.17a and b for EXP051114 and EXP060207, respectively. While in EXP051114, the downdraught is strongest NW of the updraught centre, resulting in a gust front which is coldest in the NW, in EXP060207,
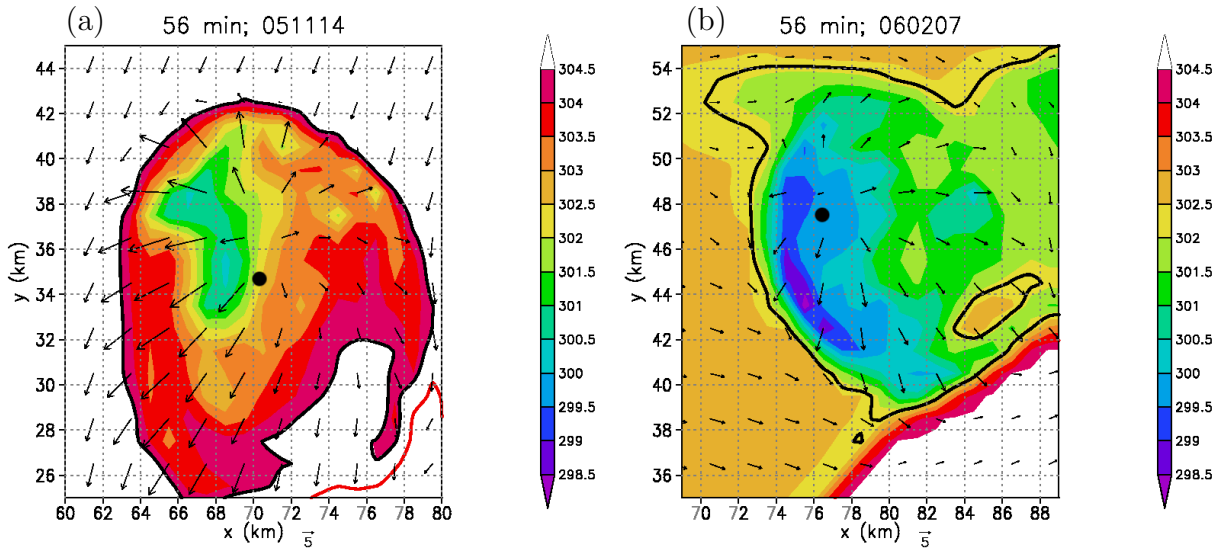
Figure 5.17: Horizontal cross-section, showing the potential temperature $\theta$ (in K) of the surface cold pool in (a) EXP051114, and (b) EXP060207, after 56 min. The sea breeze fronts and the gust front are denoted by the thick red and black lines, respectively, and vectors represent the horizontal flow at $z = 60$ m. The black dot marks the centre of the updraught at $z = 4.6$ km.

the gust front is coldest and strongest to the SW of the updraught centre (black dot in Fig. 5.17b). The latter relation is a result of the 060207-environmental winds, which are southwesterly at low-levels and easterly to northeasterly at mid- and upper-levels, resulting in advection and tilting of the updraught towards the SW. Thus, the western and southwestern portion of the gust front is supplied continously with cold air in EXP060207. This cold outflow, along with the sea breeze flow, results in strong surface convergence at the leading edge. The convergence is larger, on average, in EXP051114 than in EXP060207 (see Fig. 5.16b), but increases steadily with time in the latter case. In EXP060207, the new cell development commences at the western edge of the cold pool, where the horizontal convergence is strongest at 74 min. However, the first cell in EXP051114 forms already after 66 min due to the larger average surface convergence than in EXP060207.

As in section 5.5.4, the low-level shear ratios and angles are calculated for EXP060207 also, with the result that $\Delta c_{pool}/\Delta c_{env}$ is 1.55±0.35, 1.05±0.21, and 1.00±0.23 for the shear calculated over the lowest 1.1 km, 2.5 km, and 5.0 km, respectively. The corresponding angles between the environmental and cold pool shear vector are 78.27°±29.35°, 84.27°±31.31°, 70.94°±32.24°. The first two new cells develop at the western edge of the gust front, where the environmental shear vector points towards the west, and the shear vector behind the cold pool points towards the east. The third, fourth and fifth cells develop southwest or south to the previous one, at the SW edge of the gust front, where the angles between the shear vectors are even smaller than 90°. The close proximity of $\Delta c_{pool}/\Delta c_{env}$ to unity shows that the RKW-criterion, interpreted through Eq. (5.3), is a useful quantity for indicating where new cell development can occur. While subsidence can be found around the new updraughts at the time they develop, the sinking motion becomes stronger east of the new cells at later stages in EXP060207. Then, $\Delta c_{pool} > \Delta c_{env}$, indicating that the influence of the vorticity generated by the cold pool on the updraught

is larger than that caused by the environmental shear.

## 5.7  Summary

A numerical model with a highly idealised configuration[6] has been used to simulate multi-cellular thunderstorm complexes (Northeasters) that occur in the Darwin area of northern Australia. The overall evolution of the storm systems was reproduced well in that behind the sea breeze fronts new cells developed on the gust front of the initial updraught, forming a complex which showed characteristics similar to that in reality (propagation speed and direction, orientation, and length of the line of thunderstorms). Further experiments, where small changes to the initial model settings were made, revealed the following:

- A sea breeze can supply lifting to the initial cell what leads to a stronger updraught, to more precipitation loading within the thunderstorm, and to a stronger downdraught and gust front than if there had been no sea breeze or a sea breeze which is located far away from the initial cell.

- A strong updraught and downdraught are not indicators as to whether a (large) multicell system will develop. Large low-level horizontal convergence is the primary factor determining the regions where new cell development at the gust front of the initial updraught is most likely.

- The low-level convergence at the edge of the cold pool needs to be strong and persist for a sufficient time so that new cells can develop. This finding confirms observations of Keenan and Carbone (1992) and Wilson and Schreiber (1986) who noticed a time lag of about 18 to 25 min between the collision of the gust fronts and the detection of a new cell.

- Large horizontal convergence at the gust front is achieved if the strength of the cold pool is comparable to that of the opposing environmental flow. Whether the vertical shear generated by the environmental wind is approximately balanced by the gust front shear can be determined via Eq. (5.6). This equation was derived from the RKW-criterion and states that deep convective motion is most likely if $\Delta c_{pool}/\Delta c_{env} \approx 1$.

- The gust front is strong if the initial updraught is tilted significantly, so that the downdraught does not fall into the buoyant air, but supplies a specific region of the cold pool continuously with cool air.

- Updraught tilting is caused by strong environmental wind shear and by the vorticity generated by the sea breeze(s).

- Even though the convergence at the gust front is strong, convection can be suppressed by subsidence from pre-existing neighbouring cells.

---

[6]Here, topography was ignored and the model was initialised only with a warm bubble and one or two cold boxes, representing the sea breeze(s). In Rao and Fuelberg (2000), however, the ARPS was used, where surface characteristics, such as soil type, soil moisture, and water temperatures were implemented.

Figure 5.18:   Shown is the radar reflectivity of a thunderstorm with a strong updraught. The white/grey arrow points to the updraught region of weak reflectivity. Courtesy of the Australian Bureau of Meteorology Regional Forecasting Centre in Darwin.

The aim of this work has been to provide a deeper understanding of the overall evolution of the Northeasters and of the factors which lead to the development of thunderstorm complexes with squall-like characteristics. Even though the experiments were carried out specifically for the Darwin area, the basic principles and relations itemised above are likely to apply also to other regions in the tropics or mid-latitudes.

Together with the results in chapters 3 and 4, the work in this chapter can provide a basis for the future development or improvement of forecasting parameters and models. For example, one of the major findings here is that the updraught tilting is of utmost importance to the development of a storm system. The slope of an updraught can lead to large horizontal convergence at a location where cold air from the undisturbed downdraught is supplied to the gust front. Of course, not all parameters used in this study are available to the forecasters. However, the vertical tilt of a thunderstorm cell can be determined using radar reflectivity data, even though one must act with caution since storm movement and spatial resolution might affect the measurement (Todd Smith, personal communication). Figure 5.18 shows the radar reflectivity of a thunderstorm with a strong updraught, where the slope of the updraught is apparent. Thus, if the amount and direction of tilting of a thunderstorm cell can be estimated, the region with the largest horizontal convergence at the edge of the cold pool where new cell development is most likely can be determined. The availability of the parameters used in this thesis to forecasters will be discussed in the next chapter as well as the possibility of incorporating them into new forecasting tools.

# Chapter 6

# Important findings and their applicability for improving forecasts

In this section, the important findings and parameters used in this thesis are summarised. Suggestions are made how these parameters can be obtained from observations and how the findings can help to improve the forecasts of severe thunderstorms. A first step towards improving the forecast of split-cells was taken by suggesting a points system (see chapter 3). Of course, the points system along with the suggestions made here should not be used without thorough climatological verification. However, the following discussion is considered to be a good basis for the development of new diagnostic variables and can help the forecasters to implement the findings of this thesis in their daily routine.

### CAPE and updraught strength

One of the important diagnostic variables for forecasting thunderstorms is certainly CAPE. However, as shown in section 3.2.2, CAPE does not consider entrainment, precipitation loading, and water vapour deficit and thus, does not alone characterise the real updraught strength of the storm. Since it is difficult to measure the peak updraught speed, $w_{max}$, for any particular cell and to estimate $w_{max}$ via a proxy such as CAPE, the remaining source of information is the National Thunderstorm Forecast Guidance System (NTFGS). Model output from the NTFGS includes maximum upward motion between the surface and 850 hPa or the surface to 700 hPa, in hPa h$^{-1}$, and gives forecasts out to 48 hours at 3-hourly time steps.

### Downdraught strength and gust front strength

In chapters 3.2.3 and 5.5.2 it was shown that it is important to know the strength of the downdraught and the strength and speed of the subsequent gust front, since the latter controls whether the updraught has sufficient time to split or whether new updraughts can develop on the leading edge of the cold pool. In the Severe Thunderstorm report of 14 November 2005, for example, the reported low-level wind speeds were determined from Doppler radar images and were measured by anemometers on the ground. This "real-time" data feeds into the forecast process, but is not supplied to any real-time Numerical Weather Prediction model (currently, these NWP-models do not exist operationally). One possibility to obtain information about the gust front is to estimate its speed using Doppler radar. However, Doppler radar only measures the inbound component of the winds, thus

not allowing the gust front speed to be determined in all directions. Furthermore, some Doppler radar measurements are made at some height above the surface and these measured winds may not represent winds being experienced at the surface. Another possibility to obtain information about the gust front speed is the surface observation network. However, the network might be sparse and thus, does not allow one to estimate the gust front speed.

### Precipitation loading

The studies in chapter 3 and 4 showed that thunderstorms growing in environments with large surface humidity, as found in the tropics, exhibit a large amount of precipitation loading. The amount of precipitation loading along with the mid-tropospheric relative humidity control the strength of the downdraught and that of the subsequent gust front. Currently the radar software of the Australian Bureau of Meteorology is able to "measure" Vertically Integrated Liquid (VIL) within a storm cell. This parameter can serve as a real-time measurement of precipitation loading in a storm. Further, in terms of Numerical Weather Prediction, precipitable water is one of the outputs of NTFGS, which gives 3-hourly forecasts of precipitable water in millimetres.

### Wind profile

Together with the atmospheric instability, the vertical wind shear is an important parameter determining the severity of a thunderstorm and whether new cell development on the gust front of a pre-existing storm is possible. Thus, it is of utmost importance to know the wind profile. In addition to the environmental wind, sea breezes or a gust front can make large contributions to the low-level vertical wind shear. The Australian Bureau of Meteorology has a wind profiler situated near Darwin Airport, which measures winds from around 1 – 2 km up to 8 km with a vertical resolution of about 200 m, and a temporal resolution of one hour. In addition, there are hourly profiler data up to 20 km, however, the data quality and availability is dependant on the clarity of the atmosphere. Furthermore, wind shear is an output of NTFGS and there are options to display forecasts of maximum vertical wind shear between the surface and 850 hPa, the surface and 700 hPa, and the surface and 620 hPa, every 3 hours out to plus 48 hours.

### Vertical vorticity

In chapters 3 and 4, vertical vorticity was found to be an important parameter which determines the storm strength. Strong mid-level rotation on the updraught flank acts to lower the pressure and thereby induces updraught growth on these flanks. Vorticity is measured usually using the Doppler radar. The measurement is a method of adding the two maxima on either side of the mesocyclone (one inbound and one outbound) and averaging, to give an "average rotation strength".

### Cell tilt

In chapter 5 it was found that the tilt of the thunderstorm updraught is of utmost importance. When the updraught is tilted significantly, the downdraught does not fall into the buoyant air, but supplies a specific region of the cold pool continuously with cool air. Thus, the cold pool is strong and, if it is subjected to opposing flow, new cells are generated at the

leading edge of the cold pool. The vertical tilt of a thunderstorm can be measured using radar reflectivity data (see Fig. 5.18). However, storm movement and spatial resolution can affect the measurement.

**Subsidence**

Even though there is ascent at low-levels, subsidence from pre-existing cells can suppress new convection in their surrounding (see chapter 5). Subsidence can be observed sometimes by monitoring satellite imagery for "clear spots" between thunderstorms. Further, Doppler radar imagery can give occassionally the impression of descending air in the form of a rear-inflow jet at the back of a squall line. However, Doppler radar is only measuring the inbound/outbound component of the wind and not the vertical component.

**Sea breeze(s)**

One of the most important findings of this study is that sea breezes play a significant role in determining whether a severe multicell complex forms (see chapter 5). When the sea breeze flow opposes that of another density current, *e.g.*, a gust front, the low-level horizontal convergence is enhanced and new thunderstorms are triggered by the density current, behind the sea breeze front. Thus, it is of utmost importance to determine whether and when sea breezes occur. Mesoscale models, such as MesoLAPS or the Pennsylvania State University/National Center for Atmospheric Research mesoscale model (MM5), can help to forecast sea breezes and thus, can improve the forecast of multicell complexes, such as the Northeaster.

The information about the available equipment and the current methods used to forecast severe thunderstorms came from the Darwin Bureau of Meteorology. Even though concentrating here on Darwin in northern Australia, the basic findings and suggestions listed are likely to apply also to other regions in the tropics or mid-latitudes.

# Chapter 7

# Summary and conclusions

The initial focus of this study was to investigate the influence of vertical wind shear on thunderstorm development within a tropical environment. The simulations showed that a larger vertical wind shear is required in a tropical environment for a thunderstorm of given updraught velocity to split, compared with that in a mid-latitude environment (see chapters 3 and 4). This finding is supported by the experience of forecasters at the Australian Bureau of Meteorology Regional Forecasting Centre in Darwin that the operational storm forecasting tools developed for mid-latitude storms over-forecast supercells within the tropics.

The reason that tropical thunderstorms require higher vertical wind shears to split can be attributed either to the larger gust front speed or the earlier gust front occurrence, compared with that in the mid-latitudes. A fast gust front cuts off the storm from the warm moist inflow and the updraught has little or no time to split. In the cases where the mid-tropospheric relative humidity is larger in the tropics or comparable with that in the mid-latitudes, the total liquid water and ice content within the deeper tropical storms is larger than in the mid-latitude storms, causing a stronger downdraught. In other words, the main contribution to the negative buoyancy of the downdraught is the precipitation loading, rather than the evaporative cooling. When a tropical storm is simulated in an environment with typically smaller mid-tropospheric relative humidity than in the mid-latitudes, the amount of liquid water and ice within the storm is comparable to that within the mid-latitude storm. Intense evaporation within the tropical storm then leads to a stronger negative buoyancy than in the mid-latitude storm, causing a stronger downdraught and thus, an earlier or a faster spreading gust front. At higher shears in the tropics, entrainment reduces the storm depth and thus, the precipitation loading, resulting in a delayed gust front initiation and/or reduction of the gust front speed, which then allows storm splitting to occur.

The principal finding that a larger wind shear is required to split tropical thunderstorms than mid-latitude storms was found to be independent of the cloud model, the microphysics scheme, the horizontal resolution, the warm bubble characteristics used to initiate the storm, and the wind profile (uni-directional or directional wind shear) used.

The studies of the evolution of thunderstorms in environments with idealised wind profiles in chapters 3 and 4 are followed by two case studies of thunderstorm complexes with squall-like characteristics (chapter 5). A numerical model with a highly idealised configuration has been used to simulate these complexes (Northeasters) that occur in the Darwin area of northern Australia. The overall evolution of the storm systems was reproduced

well in that behind the sea breeze fronts new cells developed on the gust front of the initial updraught, forming a complex which showed characteristics similar to that in reality (propagation speed and direction, orientation, and length of the line of thunderstorms). It was found that sea breezes play an important role in the evolution of these thunderstorm complexes. In general, the low-level convergence at the edge of the cold pool of a pre-existing updraught needs to be strong and persist for a sufficient time so that new cells can develop at the edge. This large horizontal convergence at the gust front is achieved if the strength of the cold pool is comparable to that of the opposing environmental flow. In the case studies of 14 November 2006 and 7 February 2006, the sea breeze(s) together with the environmental wind of these days created a strong opposing flow to the gust front. On the other hand, the gust front was strong since the initial updraught was tilted significantly, so that the downdraught did not fall into the buoyant air, but supplied a specific region of the cold pool continuously with cool air. The balance between the vertical shear generated by the gust front and that generated by the sea breeze flow was quantified by a modified version of the RKW-criterion.

Forecasters in Darwin, as well as elsewhere in the tropics, have few conceptual tropical thunderstorm models at their disposal and there is a notable lack of useful theory about severe tropical thunderstorms that they can call upon. Motivated by the results of chapter 3, a points system was suggested for the forecast of supercell storms (section 3.5). This system is based on the findings that the likelihood of severe thunderstorms to occur increases if a) the wind shear increases, b) the mid-tropospheric relative humidity increases, and c) the surface moisture decreases. The points system applies well for the 63 mid-latitude and 192 tropical cases simulated with two cloud-models and using two different microphysics schemes and it can be a basis for the development of new diagnostic variables and forecasting parameters for the mid-latitudes and tropics. Furthermore, in chapter 6 suggestions were made how the parameters used in this thesis can be estimated from observations or how they can be obtained from model simulations. Moreover, it was discussed how the main findings of this work can help to improve the forecasts of severe thunderstorms. Even though concentrating on Darwin in northern Australia, the basic findings and suggestions are likely to apply also to other regions in the tropics or mid-latitudes.

# Appendix A

# List of acronyms

| | |
|---:|:---|
| **ARPS** | Advanced Regional Prediction System |
| **Bice** | Bryan's model run with the ice microphysics scheme |
| **Bkess** | Bryan's model run with the Kessler scheme |
| **CAPE** | Convective Available Potential Energy |
| **CIN** | Convective Inhibition |
| **CM1** | Cloud Model 1 (of George Bryan) |
| **DWD** | Deutscher Wetterdienst |
| **GSR04** | Gilmore *et al.* (2004) |
| **KHI** | Kelvin-Helmholtz Instability |
| **LAPS** | Limited Area Prediction System |
| **LFO** | Lin Farley Orville (microphysics scheme) |
| **MM5** | Pennsylvania State University/ National Center for Atmospheric Research mesoscale model |
| **NASA** | National Aeronautics and Space Administration |
| **NCAR** | National Center for Atmospheric Research |
| **NOAA** | National Oceanic and Atmospheric Administration |
| **Nsb** | Northerly sea breeze |
| **NSSL** | National Severe Storms Laboratory |
| **NTFGS** | National Thunderstorm Forecast Guidance System |
| **NWP** | Numerical Weather Prediction |
| **NWsb** | Northwesterly sea breeze |
| **PGF** | Pressure Gradient Force |
| **RAMS** | Regional Atmospheric Modeling System |
| **RKW** | Rotunno-Klemp-Weisman-theory, see Rotunno *et al.* (1988) |
| **RKW88** | Rotunno *et al.* (1988) |
| **TWP-ICE** | Tropical Warm Pool International Cloud Experiment |
| **UTC** | Coordinated Universal Time |
| **WK82** | Weisman and Klemp (1982) |
| **WK84** | Weisman and Klemp (1984) |
| **Wsb** | Westerly sea breeze |

# Appendix B

# List of symbols

Only the principal symbols are listed below. Symbols formed by adding primes, stars, or upper and lower indices are not generally listed separately, but are explained in the text where they appear.

$B$    Buoyancy

$c_p$    Specific heat of dry air at constant pressure (1004 J kg$^{-1}$ K$^{-1}$)

$c_{pm}$    Specific heat of moist air at constant pressure

$c_{pv}$    Specific heat of water vapour at constant pressure (1885 J kg$^{-1}$ K$^{-1}$)

$c_v$    Specific heat of dry air at constant volume (717 J kg$^{-1}$ K$^{-1}$)

$c_{vm}$    Specific heat of moist air at constant volume

$f$    Coriolis parameter $f \equiv 2\Omega \sin \phi$

$g$    Acceleration due to gravity (9.81 m s$^{-2}$)

$H$    Depth of shear layer

$L_f$    Latent heat of freezing

$L_s$    Latent heat of sublimation

$L_v$    Latent heat of vaporisation

$p$    Pressure

$p_{00}$    Reference pressure

$q_c$    Cloud water mixing ratio

$q_g$    Hail/graupel mixing ratio

$q_i$    Ice mixing ratio

$q_{iA}$    Mixing ratio of ice Type A

$q_{iB}$    Mixing ratio of ice Type B

$q_n$    Total precipitation mixing ratio $q_n \equiv q_c + q_r + q_s + q_i + q_g$

$q_r$    Rain water mixing ratio

$q_s$    Snow mixing ratio

$q_t$    Total mixing ratio $q_t \equiv q_v + q_c + q_r + q_s + q_i + q_g$

$q_v$    Water vapour mixing ratio

$q_{v0}$    Surface water vapour mixing ratio

$R_d$    Gas constant of dry air (287 J kg$^{-1}$ K$^{-1}$)
$R_m$    Gas constant of moist air $R_m \equiv R_d + R_v q_v$
$R_v$    Gas constant of water vapour (461 J kg$^{-1}$ K$^{-1}$)
$RH$    Relative Humidity
$t$    Time
$T$    Temperature
$u$    Eastward velocity
$u_i$    Velocity vector, with $i = 1, 2, 3$
$v$    Northward velocity
$w$    Upward velocity
$U_s$    Magnitude of velocity variation, determines the vertical wind shear magnitude
$x_i$    Direction vector, with $i = 1, 2, 3$
$x$    Horizontal coordinate, eastward distance
$y$    Horizontal coordinate, northward distance
$z$    Vertical coordinate, upward distance
$z^*$    Terrain-following vertical coordinate
$\alpha$    Overturning efficiency
$\delta_{ij}$    Kronecker delta
$\epsilon$    Ratio of $R_d$ to $R_v$
$\epsilon_c$    Constant, given by $R_v/R_d - 1$
$\zeta$    Component of vorticity in the $z$-direction
$\eta$    Component of vorticity in the $y$-direction
$\theta$    Potential temperature
$\theta_\rho$    Density potential temperature
$\xi$    Component of vorticity in the $x$-direction
$\pi$    Non-dimensional pressure
$\pi'$    Non-dimensional pressure perturbation
$\rho$    Density
$\rho_a$    Dry air density
$\phi$    Latitude
$\Omega$    Angular speed of rotation of the Earth

# Bibliography

[1] Bolton, D., 1980: The computation of equivalent potential temperature. *Mon. Wea. Rev.*, **180**, 1046–1053.

[2] Bryan, G. H., 2002: An investigation of the convective region of numerically simulated squall lines. *Ph.D. thesis, The Pennsylvania State University*, 181 pp.

[3] Bryan, G. H., and J. M. Fritsch, 2002: A benchmark simulation for moist nonhydrostatic numerical models. *Mon. Wea. Rev.*, **130**, 2917–2928.

[4] Byers, H. R., and R. R. Braham, 1949: "The thunderstorm." U.S. Weather Bur., Washington, D.C.

[5] Carbone, R. E., J. W. Wilson, T. D. Keenan, and J. M. Hacker, 2000: Tropical island convection in the absence of significant topography. Part I: Life cycle of diurnally forced convection. *Mon. Wea. Rev.*, **128**, 3459–3480.

[6] Chappel, L., 2001: Assessing severe thunderstorm potential days and storm types in the tropics. *Proc. Int. Workshop on the Dynamics and Forecasting of Tropical Weather Systems.* Darwin, Northern Territory, Australia, Australian Meteorological and Oceanographical Society, 1–11.

[7] Clark, T. L., 1977: A small scale numerical model using a terrain following coordinate transformation. *J. Comput. Phys.*, **24**, 186–215.

[8] Clark, T. L., 1979: Numerical simulations with a three-dimensional cloud model: later boundary condition experiments and multicellular severe storm simulations. *J. Atmos. Sci.*, **36**, 2191–2215.

[9] Clark, T. L., W. D. Hall, and J. L. Coen, 1996: Source code documentation for the Clark-Hall cloud-scale model, code version G3CH01. *National Center for Atmospheric Research.*

[10] Colon, J. A., 1953: The mean summer atmosphere of the rainy season over the western tropical Pacific Ocean. *Bull. Amer. Meteor. Soc.*, **34**, 333–334.

[11] Crook, N. A., 2001: Understanding Hector: The dynamics of island thunderstorms. *Mon. Wea. Rev.*, **129**, 1550–1563.

[12] Davies-Jones, R. P., 1986: Tornado dynamics. *Thunderstorm Morphology and Dynamics* (E. Kessler, Ed.), University of Oklahoma Press, Norman, 197–236.

[13] Doswell, C. A., and D. M. Schultz, 2006: On the use of indices and parameters in forecasting severe storms. *Electronic J. Severe Storms Meteor.*, **1(3)**, 1–22.

[14] Dotzek, N., 2002: Severe local storms and the insurance industry. *J. Meteorol.*, **26**, 3–12.

[15] Eastin, M. D., and M. C. Link, 2009: Miniature supercells in an offshore outer rainband of Hurricane Ivan (2004). *Mon. Wea. Rev.*, in press.

[16] Edwards, R., 2006: Supercells of the Serranias del Burro (Mexico). *Preprints*, 23rd Conf. Severe Local Storms, St. Louis MO, 1–6.

[17] Emanuel, K. A., 1994: Atmospheric convection. *Oxford*, 580 pp.

[18] Gilmore, M. S., and L. J. Wicker, 1998: The influence of midtropospheric dryness on supercell morphology and evolution. *Mon. Wea. Rev.*, **126**, 943–958.

[19] Gilmore, M. S., J. M. Straka, and E. N. Rasmussen, 2004: Precipitation and evolution sensitivity in simulated deep convective storms: comparisons between liquid-only and simple ice and liquid phase microphysics. *Mon. Wea. Rev.*, **132**, 1897–1916.

[20] Goler, R., M. J. Reeder, R. K. Smith, H. Richter, S. Arnup, T. Keenan, P. May, and J. Hacker, 2006: Low-Level Convergence Lines over Northeastern Australia. Part I: The North Australian Cloud Line. *Mon. Wea. Rev.*, **134**, 3092–3108.

[21] Heus, T., and H. J. J. Jonker, 2008: Subsiding shells around shallow cumulus clouds. *J. Atmos. Sci.* , **65**, 1003–1018.

[22] Houze, R. A., 1993: Cloud Dynamics. *Academic Press*, 574 pp.

[23] Jordan, C. L., 1958: Mean soundings for the west Indies area. *J. Meteor.*, **15**, 91–97.

[24] Keenan, T. D., and R. E. Carbone, 1992: A preliminary morphology of precipitation systems in tropical northern Australia. *Quart. J. Roy. Meteor. Soc.*, **118**, 283–326.

[25] Kingsmill, D. E., 1995: Convection initiation associated with a sea-breeze front, a gust front, and their collision. *Mon. Wea. Rev.*, **123**, 2913–2933.

[26] Klemp, J. B., 1987: Dynamics of tornadic thunderstorms. *Ann. Rev. Fluid Mech.*, **19**, 369–402.

[27] Klemp, J. B., and R. B. Wilhelmson, 1978: The simulation of three-dimensional convective storm dynamics. *J. Atmos. Sci.* , **35**, 1070–1096.

[28] Klemp, J. B., and R. B. Wilhelmson, 1978: Simulations of right- and left-moving storms produced through storm splitting. *J. Atmos. Sci.* , **35**, 1097–1110.

[29] Lafore, J.-P., and M. W. Moncrieff, 1989: A numerical investigation of the organization and interaction of the convective and stratiform regions of tropical squall lines. *J. Atmos. Sci.* , **46**, 521–544.

[30] Lafore, J.-P., and M. W. Moncrieff, 1990: Reply. *J. Atmos. Sci.* , **47**, 1034–1035.

[31] Lin, Y.-L., R. D. Farley, and H. D. Orville, 1983: Bulk parameterization of the snow field in a cloud model. *J. Climate Appl. Meteor.*, **22**, 1065–1092.

[32] Mapes, B., and R. A. Houze Jr., 1992: An integrated view of the 1987 Australian monsoon and its mesoscale convective systems. I: Horizontal structure. *Q. J. R. Meteorol. Soc.*, **118**, 927–963.

[33] May, P. T., and A. Ballinger, 2007: The statistical characteristics of convective cells in a monsoon regime (Darwin, Northern Australia). *Mon. Wea. Rev.*, **135**, 82–92.

[34] May, P. T., A. R. Jameson, T. D. Keenan, P. E. Johnston, and C. Lucas, 2002: Combined wind profiler/polarimetric radar studies of the vertical motion and microphysical characteristics of tropical sea-breeze thunderstorms. *Mon. Wea. Rev.*, **130**, 2228–2239.

[35] May, P. T., and D. K. Rajopadhyaya, 1999: Vertical velocity characteristics of deep convection over Darwin, Australia. *Mon. Wea. Rev.*, **127**, 1056–1071.

[36] McCaul, E. W., Jr. and M. L. Weisman, 1996: Simulations of shallow supercells in landfalling hurricane environments. *Mon. Wea. Rev.*, **124**, 408–429.

[37] McCaul, E. W., Jr. and M. L. Weisman, 2001: The sensitivity of simulated supercell structure and intensity to variations in the shapes of environmental buoyancy and shear profiles. *Mon. Wea. Rev.*, **129**, 664–687.

[38] McCaul, E. W., Jr., C. Cohen, and C. Kirkpatrick, 2005: The sensitivity of simulated storm structure, intensity, and precipitation efficiency to environmental temperature. *Mon. Wea. Rev.*, **133**, 3015–3037.

[39] National Academy of Science, 1998: The Atmospheric Sciences Entering the Twenty-First Century. *National Academy Press, Washington DC*, 364pp.

[40] Novlan, D. J., and W. M. Gray, 1974: Hurricane-spawned tornadoes. *Mon. Wea. Rev.*, **102**, 476–488.

[41] Rao, P. A., and H. E. Fuelberg, 2000: An investigation of convection behind the Cape Canaveral sea-breeze front. *Mon. Wea. Rev.*, **128**, 3437–3458.

[42] Rasmussen, E. N., and D. O. Blanchard, 1998: A baseline climatology of sounding-derived supercell and tornado forecast parameters. *Wea. Forecasting*, **13**, 1148–1164.

[43] Rotunno, R., 1981: On the evolution of thunderstorm rotation. *Mon. Wea. Rev.*, **109**, 171–180.

[44] Rotunno, R., and J. B. Klemp, 1982: The influence of the shear-induced pressure gradient on thunderstorm motion. *Mon. Wea. Rev.*, **110**, 136–151.

[45] Rotunno, R., J. B. Klemp, and M. L. Weisman, 1988: A theory for strong, long-lived squall lines. *J. Atmos. Sci.*, **45**, 463–481.

[46] Smith, R. K., G. Garden, J. Molinari, and B. R. Morton, 2001: Proceedings of an International Workshop on the Dynamics and Forecasting of Tropical Weather Systems. *Bull. Amer. Meteor. Soc.*, **81**, 2825–2829.

[47] Smith, R. K., M. T. Montgomery, and H. Zhu, 2005: Buoyancy in tropical cyclone and other rapidly rotating atmospheric vortices. *Dyn. Atmos. Oceans*, **40**, 189–208.

[48] Weisman, M. L., and J. B. Klemp, 1982: The dependence of numerically simulated convective storms on vertical wind shear and buoyancy. *Mon. Wea. Rev.*, **110**, 504–520.

[49] Weisman, M. L., and J. B. Klemp, 1984: The structure and classification of numerically simulated convective storms in directionally varying wind shears. *Mon. Wea. Rev.*, **112**, 2479–2498.

[50] Weisman, M. L., J. B. Klemp, and R. Rotunno, 1988: Structure and evolution of numerically simulated squall lines. *J. Atmos. Sci.*, **45**, 1990–2013.

[51] Weisman, M. L., and R. Rotunno, 2004: "A theory for strong long-lived squall lines" revisited. *J. Atmos. Sci.*, **61**, 361–382.

[52] Wilson, J. W., and W. E. Schreiber, 1986: Initiation of convective storms at radar-observed boundary-layer convergence lines. *Mon. Wea. Rev.*, **114**, 2516–2536.

[53] Wissmeier, U., and R. Goler, 2009: A comparison of tropical and mid-latitude thunderstorm evolution in response to wind shear. *J. Atmos. Sci.*, **66**, 2385–2401.

# Acknowledgements

I am grateful to the following people and institutions:

# Curriculum Vitae

**Ulrike Wißmeier**
Faculty of Physics, Ludwig–Maximilians–University
Theresienstr. 37, D-80333 Munich
E-Mail ulrike@meteo.physik.uni-muenchen.de

## Education

| | |
|---|---|
| 10/2006 – 10/2009 | **Ph.D. student at the University of Munich (LMU)**, Faculty of Physics, chair of Prof. Dr. Roger K. Smith. Thesis: "The Physics of Tropical Convection" |
| 10/2000 – 01/2006 | **M.Sc. in Physics**, University of Munich (LMU) Diploma-thesis: "k-Essence and Hybrid Inflation" at the chair of Prof. Dr. V. Mukhanov |
| 09/2002 – 03/2003 | Foreign semester at the University of Havana, Cuba |
| 10/1999 – 09/2000 | **Studies in Technical Physics** at the University of Applied Sciences, Munich |
| 09/2000 | Intermediate diploma |
| 09/1998 - 09/1999 | **Upper vocational school**, Nuremberg |
| 08/1994 - 09/1996 | **Apprenticeship** as an Electrical Assistant at Siemens, Erlangen |

## Work History

| | |
|---|---|
| 04/2006 – 09/2006 | Employment at Patent Lawyers Office Hoffman-Eitle, Munich |
| 10/2005 - 02/2006 | Tutor of quantum mechanics exercise group, University of Munich |
| 09/2003 - 02/2006 | ERASMUS-Tutor at the University of Munich |
| 03/2001 | Working student at Siemens, San Jose, Costa Rica |
| 09/2000 | Working student at Siemens, Paris, France |
| 10/1996 - 07/1998 | Employment at Siemens. Power Transmission and Distribution, Nuremberg |

**Publications**

- Wissmeier, U., and R. Goler, 2009: A comparison of tropical and mid-latitude thunderstorm evolution in response to wind shear. *J. Atmos. Sci.*, **66**, 2385–2401.

- Wissmeier, U., and R. Goler, 2008: The influence of vertical wind shear on deep convection in the tropics. *28th Conference on Hurricanes and Tropical Meteorology, Orlando, FL, Amer. Meteor. Soc.*, Extended abstract.

**Scientific Activities**

- Visiting scientist at the NOAA Hurricane Research Division, Miami, Florida (10/2008)

- Visiting scientist at the Bureau of Meteorology, Darwin, Australia (02/2007–03/2007)

**Conferences and Summer Schools**

- $28^{th}$ Conference on Hurricanes and Tropical Meteorology 2008 (Orlando, FL, USA); Oral presentation: The Influence of Vertical Wind Shear on Deep Convection in the Tropics.

- EGU General Assembly 2008 (Vienna, Austria); Poster: A Comparison of Tropical and Mid-latitude Storm Evolution in Response to Wind Shear.

- $4^{th}$ European Conference on Severe Storms ECSS 2007 (Trieste, Italy); Oral presentation: The Influence of Vertical Wind Shear on Deep Convection in the Tropics.

- Mitteldeutsche Physik-Combo 2005 (Jena, Germany).

- XXXV Latin American School of Physics *ELAF* 2004 (Mexico City, Mexico).